P-117

NASA CONTRACTOR REPORT 166582

Propfan Experimental Data Analysis

David F. Vernon
Gregory S. Page
H. Robert Welge

IN-05
DATE OVERRIDE
97696

CONTRACT NAS2-11672
August 1984

NASA

DATE OF GENERAL RELEASE JUNE 1987

NASA CONTRACTOR REPORT 166582

Propfan Experimental Data Analysis

David F. Vernon
Gregory S. Page
H. Robert Welge

McDonnell Douglas Corporation
Douglas Aircraft Company
Long Beach, California 90846

Prepared for
Ames Research Center
Under Contract NAS2-11672

NASA
National Aeronautics and
Space Administration

Ames Research Center
Moffett Field, California 94035

Date for general release June 1987

TABLE OF CONTENTS

NOMENCLATURE

A_E	cross sectional exhaust nozzle area
AR	aspect ratio
$C_{D_{BAL}}$	balance drag coefficient
$C_{D_{EFF}}$	thrust removed drag coefficient
C_L	lift coefficient
$C_{L_{EFF}}$	thrust removed lift coefficient
C_{mac}	mean aerodynamic chord
C_P	power coefficient
c_p	pressure coefficient
$C_{T_{AP}}$	apparent thrust coefficient
$C_{T_{AVG}}$	jet thrust calibration factor
$C_{T_{JET}}$	exhaust nozzle thrust coefficient
$C_{T_{NET}}$	net propeller thrust coefficient
D	propeller diameter
DAC	Douglas Aircraft Company
DELCXN	nacelle buoyancy coefficient
EPR	exhaust pressure ratio (P_{TE}/P_{SE})
ETA	percent wing semispan
F	exhaust nozzle thrust
FRP	fuselage reference plane
J	propeller advance ratio (V/nD)
LEX	wing leading edge extension
M_L	local normal Mach number based on wing quarter chord sweep

NOMENCLATURE

(continued)

M_o, M	freestream Mach number
NASA	National Aeronautics and Space Administration
NPR	nozzle pressure ratio (P_{TE}/P_{AMB})
n	propeller speed (rev/sec)
P	turbine shaft power
P_{AMB}	ambient static pressure
P_{SE}	exhaust nozzle exit static pressure
P_{TE}	exhaust nozzle total pressure
PTR	propeller test rig
q_∞	freestream dynamic pressure ($1/2\ \rho V_\infty^2$)
R_{ec}	Reynold's number based on C_{mac}
RPM	revolutions per minute
S_{REF}	reference area
T	transition location
TIDEAL	ideal jet thrust
TJET1	actual jet thrust
V_∞	tunnel freestream velocity
V_{EFF}	effective velocity seen by propeller
x/c	fraction of local chord
α	angle of attack (deg)
β	propeller blade pitch angle
η	propeller efficiency
ρ_∞	freestream density
$\Lambda_{c/4}$	wing quarter chord sweep

1.0 SUMMARY

The National Aeronautics and Space Administration(NASA) and Douglas Aircraft Company(DAC) have been working for several years to develop the installation aerodynamics technology for wing mounted turboprop propulsion system installations to the level required to assess the full potential of the propfan propulsion concepts. To meet this need, tests of several different wing/nacelle/power configurations have been made by NASA Ames. This report summarizes several design and data analysis tasks for these tests conducted by Douglas Aircraft Company in support of the NASA Ames installation aerodynamic program.

A data reduction thrust/drag bookkeeping method which is consistent with the performance prediction methods used for analysis of new aircraft designs is defined. Although numerous thrust/drag bookkeeping methods can be used, this method is compatible with data available to the engine, propeller and airframe manufacturers. When compared to the method used by NASA for analysis of Ames 11-foot transonic wind tunnel test data an 18 count (.0018) difference in interference drag results. This difference represents roughly 4% of the total configuration drag.

Powered data from the Ames high speed test for the underwing nacelle installation is reduced using the new thrust/drag accounting system, and a summary of the experimental performance is made. Pressure and flow visualization data from the test for both the straight underwing nacelle, and unpowered contoured overwing nacelle installations is used to determine the flow phenomena present for a wing mounted propfan installation. The test data is compared to analytic methods, showing the analytic methods to be suitable for design and analysis of new configurations. This analysis indicates that designs with zero interference drag levels are achieveable with proper wing and nacelle tailoring.

The performance of an unpowered overwing countered nacelle with a solid body exhaust plume simulation is evaluated both with and without a wing leading edge extension (LEX). The effects of the LEX and of nacelle contouring are shown to be complimentary, but not strictly additive. Improvements in the wing flow obtained utilizing one modification, make additional large improvements by the complimenting modification more difficult to achieve. A new contoured overwing nacelle design as well as modifications to the existing contoured nacelle and wing leading edge extension wind tunnel model geometries are evaluated. Hardware constraints of the current model parts prevent obtaining any significant performance improvements due to the modified nacelle and LEX shapes.

A new, aspect ratio 11 wing design for an up outboard single rotation propfan installation is defined, and an advanced contoured nacelle is provided for this wing. The design shows a slight reduction in induced drag, when compared to the unpowered clean wing in lifting line analysis, and maintains good pressure characteristics for the power-on case.

2.0 INTRODUCTION

The reduction of aircraft fuel consumption has been a major goal of NASA and the Douglas Aircraft Company for many years. The Aircraft Energy Efficiency (ACEE) program has been a major part of this effort. One of the more recent areas of study for reduction of aircraft fuel consumption is the incorporation of advanced propeller (propfan) propulsion systems. The configurations under consideration consist of highly loaded eight to ten blade propellers, capable of high efficiency at cruise Mach numbers from 0.7 to 0.8.

The technology required to exploit the fuel savings offered by the propfan propulsion systems includes the developement of an efficient propeller and nacelle design that minimizes the interference drag penelty when installed on supercritical wings. This is a much more severe design constraint than the installation of current turbofan propulsion systems, as not only the wing/nacelle interactions must be considered, but the wing/slipstream interactions must also be evaluated.

Initial testing used a wing developed for a turbofan concept, with a simulated propeller slipstream (reference 1). This test identified many of the critical issues affecting the turboprop installation including an increase in local stream velocity causing a change in shock location and strength, and large changes in the local wing upwash (or downwash) causing large changes in the leading edge suction pressure levels. A later test employed the same wing geometry definition, and added a straight, underwing nacelle and propeller system (reference 2). This test helped emphasize the importance of the nacelle to the understanding of the complete propulsion system installation picture. A test using a different wing geometry and several alternate nacelle geometries helped identify the significance of contouring the nacelle to account for the wing flow field. The results of this test are contained in unpublished NASA data. Both wing and nacelle design modifications based on the reference 2 test results were defined, and later tested.

This report describes an analysis performed for this latest test data. The test contained a baseline wing geometry (Table 1, reference 2), a modified wing geometry (Table 2, reference 2), a straight underwing nacelle and propeller installation, and a unpowerd contoured overwing nacelle installation. The wind tunnel model installation for the straight underwing nacelle configuration is shown in figure 1.

Section 3.0(Task I) of this report details the development of a thrust/drag accounting method for turboprop installations. The thrust/drag accounting method is employed to assess the results of the wind tunnel tests utilizing isolated propeller performance to determine the installation or interference drag which is defined as the total configuration drag minus the clean wing and nacelle parasite drag. Isolated propeller performance can be obtained from the propeller manufacturer, allowing the analysis of many propeller designs on a given aircraft, without retesting each configuration.

Section 4.0(Task II) of the report uses the pressure and flow visualization data to describe the flow phenomenum producing the measured installation

interference drag. The experimental data is compared to suitable analysis methods for both the low (0.6 M_0) and high (0.8 M_0) Mach number data to verify the accuracy of the methods used to design the model geometry. The effects of the nacelle installation are considered both with and without the additional effects due to power. The wing leading edge extension (LEX) is analyzed to determine if it was successful in reducing the effects of power on the wing pressure distributions, and the resulting drag levels are presented.

Section 5.0(Task III) evaluates the effects of the nacelle contouring on reducing the installation interference drag. The contoured nacelle data does not contain any power effects, however, the model did include a solid body exhaust plume simulation to account for nacelle base drag effects. The combination of the contoured nacelle and the LEX is assessed to determine the extent to which the effects of the two modifications are additive. Using a more comprehensive nacelle contouring scheme, a new advanced contoured nacelle is designed. Enhancments to the existing contoured overwing nacelle and LEX geometries are explored. A new aspect ratio 11 wing is designed for an up outboard rotation turboprop propeller/nacelle installation. An advanced contoured nacelle is defined for integration with the up-outboard rotation wing design.

3.0 TASK I. THRUST/DRAG BOOKKEEPING

3.1 Thrust/Drag Bookkeeping Methods

In the design of a new aircraft configuration, the thrust required to overcome drag must be defined to allow for proper engine sizing, which in turn is needed to establish suitable aircraft takeoff, climb, and cruise performance. The purpose of performing thrust/drag bookkeeping analysis on wind tunnel test data is to quantify all of the measureable thrust and drag components acting on a model configuration and to ensure that these components are defined in a way that can be used by the engine, propeller, and aircraft manufacturers to predict aircraft performance. The primary point for this discussion is that the propeller and nozzle data must be based on isolated characteristics, as the isolated characteristics are all that the manufacturers of the components can supply. Any installed interferences, both on the aircraft and on the propulsion unit, are included in the polar for each specific configuration. For wind tunnel data analysis, these isolated characteristics are obtained by calibration of the wind tunnel propulsion hardware and the resulting forces are removed from the data. Then the thrust terms obtained from isolated propeller and engine tests can be combined with the resulting polars to predict aircraft performance.

In both the current NASA and DAC bookkeeping methods, propeller and engine exhaust nozzle thrust terms are removed from the drag balance measurements for a series of angles of attack at several different Mach numbers in the following manner:

$$C_{D_{EFF}} = C_{D_{BAL}} - C_{T_{NET}} - C_{T_{JET}} \qquad (1)$$

The resulting thrust removed drag polars are used to find drag levels at a pre-defined lift coefficient for each Mach number. Parasite drag terms, which account for skin friction and propwash scrubbing, are calculated using standard procedures at the specified lift coefficient and subtracted out of the thrust-removed drag terms in order to obtain interference drag. What distinguishes the two methods from one another is the manner in which the propeller and engine exhaust nozzle thrust terms are calculated.

In the following sections both the NASA and DAC methods for determining propeller and exhaust nozzle thrust will be described. A comparison is made of results obtained from both methods for selected test conditions from the Ames test. As shown in figure 2 the powered conditions chosen for analysis are representative of normal cruise flight power settings at each Mach Number. Results, in the form of interference drag levels and lift curves, are given for each method. Finally, conclusions are drawn concerning the ramifications of the new analysis method.

3.1.1 Current NASA Installed Performance Method

In the force data reduction method currently used by NASA, the net propeller thrust is obtained from a rotating balance on the propeller drive shaft using the following relation:

$$C_{T_{NET}} = C_{T_{AP}} - DELCXN \tag{2}$$

where $C_{T_{AP}}$ is the apparent thrust coefficient, which accounts for hub base drag forces, and DELCXN is the nacelle buoyancy correction term which accounts for the opposing force generated on the propeller disk due to the presence of the nacelle. A brief outline of the installed procedure is shown in figure 3. Since the propeller thrust obtained in this manner is acting in the presence of the wing and nacelle, the value measured is configuration-dependent and, therefore, is not compatible with performance prediction techniques available to engine, propeller and airframe manufacturers. The performance data generated by engine and propeller manufacturers represents isolated performance predictions and are independent of any specific aircraft configuration.

The exhaust nozzle thrust coefficient ($C_{T_{JET}}$) is derived from a semi-empirical analysis which is developed in reference 3. The actual jet thrust term (TJET1) is the product of the ideal thrust (TIDEAL) and a jet thrust calibration factor ($C_{T_{AVG}}$) as shown below:

$$TJET1 = (C_{T_{AVG}})(TIDEAL) \tag{3}$$

where:
$$TIDEAL = A_E\left(P_{SE}\left\{\left(\frac{2q}{q-1}\right)\left[\left(\frac{P_{TE}}{P_{SE}}\right)^{\frac{\gamma-1}{\gamma}} - 1\right] + 1\right\} - P_{AMB}\right) \tag{4}$$

and:
$$C_{T_{AVG}} = \text{ACTUAL THRUST/IDEAL THRUST} \tag{5}$$

Once TJET1 is known, the exhaust nozzle thrust coefficient is found using the following relation:

$$C_{T_{JET}} = TJET1/q_\infty S_{REF} \tag{6}$$

The results of an exhaust nozzle calibration study conducted by Tech Development were used to calculate $C_{T_{AVG}}$ over a range of exhaust nozzle pressure ratios from 1.08 through 1.91. The exhaust nozzle and associated instrumentation were removed from the air driven turbine motor and mounted in the Fluidyne static test stand which is located at the Fluid Dyne Engineering Corporation's Medicine Lake Laboratory.The resulting experimental datapoints, together with a fitted calibration curve, are shown in figure 4. As in the case of the propeller thrust, the exhaust nozzle thrust term obtained from this procedure is dependent on a specific configuration since the ideal thrust term is a function of the local exhaust nozzle static pressure, P_{SE}.

In order to account for nacelle pitch-down and toe-in as well as exhaust thrust orientation with respect to the FRP, the $C_{T_{NET}}$ and $C_{T_{JET}}$ terms obtained using the preceeding equations are reduced into components acting in the axial and normal directions. A complete set of the equations used

to account for nacelle and exhaust nozzle orientation in the NASA method appears in reference 4.

3.1.2 DAC Isolated Performance Method

In the DAC bookkeeping method, both the propeller thrust and engine exhaust nozzle thrust are determined on an isolated basis; that is, they are calculated from propeller and engine manufacturers' experimental data which, as mentioned earlier, is independent of the specific aircraft configuration. An outline showing the proposed data reduction technique is given in figure 5.

The isolated propeller thrust term is found using propeller performance charts similar to the one shown in figure 6. The propeller charts used in the analysis of the Ames test data were generated at the NASA Lewis PTR for the Hamilton Standard SR-2C propeller. A set of these propeller charts appears in Appendix A.

For each test point a power coefficient (C_P) is calculated using the following equation:

$$C_P = \frac{P}{\rho_\infty n^3 D^5} \tag{7}$$

where P is the shaft horsepower calculated from the rotating balance torque and RPM and ρ_∞ is the freestream density at each test condition.

For each C_P at a given blade angle (β), a propeller efficiency(η) is found from the chart. C_P and β are used because they are directly related to fuel flow for an aircraft application and do not require the knowledge or assumption of a "velocity" as the Advance Ratio(J) does. Also, for normal operating conditions, C_P and β uniquely determine J, since any two parameters are all that is required to determine propeller performance. Once the propeller efficiency is found, the following relation is then used to determine the propeller thrust coefficient:

$$C_{T_{NET}} = \frac{\eta P}{q_\infty V_\infty S_{REF}} \tag{8}$$

The isolated exhaust nozzle calibration is the same data as previously discussed for the Tech Developement motor, however, the data were analyzed in a different manor.

The equation used to calculate the actual exhaust nozzle thrust is developed from the ideal thrust relation. Assuming subsonic nozzle flow (NPR $\leq$ 1.893), the ideal thrust equation can be written as:

$$\frac{F}{P_{AMB} A_E} = \frac{2\gamma}{\gamma-1}\left[\left(\frac{P_{TE}}{P_{AMB}}\right)^{\frac{\gamma-1}{\gamma}} - 1\right] \tag{9}$$

This equation differs from Eq. 4, which is developed in reference 3, in that it does not contain a local static pressure term (P_{SE}).

For air, $\gamma = 1.4$, and Eq. 9 can be rewritten as:

$$\frac{F}{P_{AMB}\, A_E} = 7\left[\left(\frac{P_{TE}}{P_{AMB}}\right)^{.2857} - 1\right] \tag{10}$$

Equation 10, plotted together with the Fluidyne static test calibration data, is given in figure 7. The calibration data simply appears to "bend over" faster than the ideal thrust curve. If Eq. 10 is rearranged as follows:

$$\left(\frac{P_{TE}}{P_{AMB}}\right)^{N} = 1 + \frac{F}{(7)\, P_{AMB}\, A_E} \tag{11}$$

and plotted in log-log format, then the exponent N is readily determined as the slope of the curve. Using this procedure, a curve-fit of the exhaust thrust calibration is established:

$$\frac{F}{P_{AMB}\, A_E} = 7\left[\left(\frac{P_{TE}}{P_{AMB}}\right)^{.2682} - 1\right] \tag{12}$$

Figure 8 shows the experimental calibration points together with the curve fit from Eq. 12. Equation 12 represents an exhaust nozzle thrust term which is based on isolated test data and is a function only of the nozzle total and ambient static pressures.

For each wind tunnel test point (i.e., each NPR), an exhaust nozzle thrust term is calculated using Eq. 12. The exhaust nozzle thrust coefficient can then be found using:

$$C_{T_{JET}} = \frac{F}{q_\infty S_{REF}} \tag{13}$$

Unlike the current NASA method, the $C_{T_{NET}}$ and $C_{T_{JET}}$ terms calculated using the isolated data are assumed to act in the freestream direction and are therefore added directly to the balance measurement in order to obtain the thrust removed drag. The thrust removed lift($C_{L_{EFF}}$) is obtained by correcting the normal force balance reading for angle-of-attack. The thrust removed drag and lift terms are obtained in this manner because, although the geometric nacelle pitchdown and toe-in and exhaust nozzle toe-in angles are known relative to the FRP, the resultant directions in which these thrust forces actually act cannot be defined and are included in the lift and drag polars using this procedure.

Parasite drag terms have been calculated to account for skin friction, propeller scrubbing, and nacelle form drag using form factors and skin friction coefficients obtained at the appropriate Reynolds numbers. These

parasite drag terms were used in both bookkeeping methods. A summary of values obtained for the different parasite drag terms appears in Appendix B.

3.2 Thrust/Drag Bookkeeping Method Comparison

To illustrate the differences between the two force bookkeeping methods, a comparison of propeller and exhaust nozzle thrust terms, as well as the resulting thrust removed lift and drag values calculated using both methods, is presented in the Table below. The selected test point for this comparison is the wing/nacelle/power case at 0.8M. A force data summary of the interference drag levels for all of the test points analyzed will be presented in the following section.

METHOD COMPARISON

	$C_{T_{NET}}$		$C_{T_{JET}}$		$C_{D_{EFF}}$		$C_{L_{EFF}}$	
$\alpha°$	DAC	NASA	DAC	NASA	DAC	NASA	DAC	NASA
1.0	.02780	.03087	.01779	.01800	.04490	.04689	.37800	.37700
2.0	.02740	.03009	.01754	.01742	.05280	.05461	.49600	.49440
3.0	.02482	.02691	.01459	.01450	.06180	.06326	.60100	.59950

A comparison between the drag polars constructed using the above data is given in figure 9. A complete set of all drag polars used in the analysis appears in Appendix C. The tabulated data above shows that most of the differences in drag levels can be attributed to the difference in the net propeller thrust values ($C_{T_{NET}}$). At a C_L of .5, the drag level for the NASA method is 18 counts higher than that for the isolated thrust method. These 18 counts can be attributed mainly to the influence of the wing and nacelle installation on the propeller.

3.3 RESULTS

The results of the force data analysis are presented in figure 10, which shows interference drag levels as a function of Mach Number for both bookkeeping methods. For the wing nacelle combination without the LEX, the interference drag levels obtained from the isolated thrust data are less than the installed method by 10 counts at $.75M_0$ and 18 counts at $.8M_0$. For the wing nacelle combination including the LEX, there is no difference in interference levels at $.75M_0$ while at $.8M_0$ the isolated thrust data level is roughly 8 counts less than the installed thrust data level. Both of these configurations exhibit a similar trend in that as Mach Number is increased above .75 the difference between the interference drag levels increases. For the fillet configuration the trend seen in the first two configurations seems to be reversed. At $.78M_0$ the interference drag level for the fillet configuration is roughly 13 counts higher for the isolated thrust method while at .8M both methods show essentially no interference drag. This reversal may be due to the fact that the positioning of the fillet, which is only .25 blade diameters downstream of the prop-plane, may have a significant influence on the installed prop thrust.

Figure 11 shows a comparison between the thrust removed lift curves generated using both force data reduction methods. There is a slight

increase in the level of the lift curves for the isolated thrust method as compared to the installed thrust method. This shift can be considered negligible since, at the most, it results in a C_L increase of only .005.

One way of determining the inflow velocity to the propeller is from the isolated propeller charts. Each test point has a unique power coefficient which is calculated using Eq. 7. For a given blade angle, a value for J can be found for each power coefficient using the propeller charts at the freestream Mach number. The J obtained in this manner is based on isolated prop data, therefore, the associated velocity is the local propeller onset velocity. Figure 12 shows two propeller curves, one based on isolated propeller data and the other based on tunnel freestream velocity. These results are similar to the results obtained in Reference 4. This shift in the propeller curve for the 0.8 tunnel freestream Mach number condition has an effect on propeller performance since propeller efficiency levels are a function of J. This difference in propeller performance shows up in the interference drag levels shown in Figure 10.

4.0 TASK II. DATA ANALYSIS, UNDERWING NACELLE

Section 3.0 of this contract presented a discussion and suggested approach for assessing the propulsion system interference drag levels in such a way that they are compatable with data supplied by the propeller manufacturer. Having established these drag levels, an analysis of the surface pressure and oil flow photographs is necessary to gain an understanding of the aerodynamics features of the propulsion system installation. In addition, comparisons of the surface pressure data with theoretical methods is required to establish the accuracy of these methods for future design.

4.1 Analysis of Straight Underwing Nacelle Data

The test conditions chosen for the experimental wing pressure summary presented in this section correspond to the same test conditions used in determining the interference drag levels shown in figure 10. The DAC isolated interference drag buildup results for the wing-nacelle configuration shown in figure 13 and 14, with and without power, are shown in figure 15. The corresponding pressure data obtained for freestream Mach numbers of 0.6, 0.75, and 0.8 appears in figures 16, 17, and 18 respectively. (Force and pressure data for the wing-nacelle-power case at $0.6M_0$ was not obtained during the Ames test and, as a result, interference drag levels are not available at this condition; however, suitable powered wing pressure data was obtained during the previous Ames test in the 14-foot transonic wind tunnel and is included in figure 16.)

At 0.6 M_0, the 20 count interference drag level due to the nacelle presented in figure 15 can most likely be attributed to the increased wing suction peak levels inboard of the nacelle. At the ETA = .418 pressure row, the presence of the nacelle results in suction peak normal Mach numbers based on wing c/4 sweep(M_L) of just over 1.1. The significance of this result is that even at this relatively low Mach number, the wing is experiencing regions of transonic flow due to the presence of the straight underwing nacelle. Previous analysis of installation effects for varying nacelle shapes (reference 2) has shown that proper tailoring or contouring of the nacelle shape can help alleviate these localized regions of highly accelerated flow.

As Mach number is increased from 0.6 to 0.8 the nacelle interference drag increases roughly 15 counts. This rise in the interference drag level can be attributed to increased wing compressibility effects. These compressibility effects are most clearly illustrated in the pressure distributions immediately inboard of the nacelle at the ETA = .418 pressure row (figures 17 and 18). The local suction peak Mach numbers just inboard of the nacelle at 0.75 and $0.80M_0$ are roughly 1.4 and 1.6, respectively, as compared to 1.1 for the $0.6M_0$ condition. These higher local Mach numbers result in stronger wing shocks. The flow visualization pictures presented in figures 19 and 20 for the windmilling test condition indicate a stronger more unswept shock at the $0.8M_0$ condition as compared to the $0.75M_0$ condition.

Comparison of the flow visualization for the clean wing (figure 21) and the unpowered nacelle configuration presented in figure 20 indicates the change in upper surface spanwise flow due to the presence of the nacelle.

As shown in figure 15, the addition of power (up-inboard propeller rotation) leads to a further increase in the interference drag values at all Mach numbers analyzed. Figures 17 and 18 show that at the ETA = .365 pressure row, where the effects of power are most pronounced, the onset of power increases the suction peak local Mach numbers from 1.2 to 1.6 at $0.75M_0$ and from 1.3 to 1.5 at $0.8M_0$. These higher inboard peak levels are due to an increase in the local wing angle-of-attack resulting from propeller upwash. For the area of the wing just outboard of the nacelle the effect of the propeller onset flow is reversed with a propeller downwash component producing a lower local angle-of-attack and, as a result, more positive wing pressures. At the ETA = .418 pressure row the effect of power has no appreciable effect on the wing suction peaks but rather a "bubbling" effect on the wing upper surface pressure recovery which may be due to a laminer bubble or local separated flow. The flow visualization pictures presented in figures 22 and 23 both appear to show an area of local separated flow in the region where this "bubbling" effect occurs in the pressure distributions.

Interference drag results for the wing leading edge extension (LEX) configuration (shown in Figure 24 and 25) with and without the inboard nacelle/wing fillet, are shown in Figure 26. The corresponding wing pressure data appears in figures 27, 28, and 29. At $0.6M_0$ the presence of the LEX results in a 10 count drag benefit when compared with the same unpowered nacelle configuration without the LEX (figure 15). Comparison of the $0.6M_0$ pressure data presented in figure 27 with the unmodified baseline wing-nacelle data previously shown in figure 16 demonstrates the effectiveness of the LEX in reducing the wing leading-edge peak local Mach numbers. At the pressure row just inboard of the nacelle (ETA = .418) the LEX reduces the wing local Mach numbers from 1.1 to a subsonic value. The drag benefit due to the LEX increases at higher Mach numbers; at $0.8M_0$ a 20 count benefit, relative to the unmodified wing, is realized. Comparing the $0.8M_0$ LEX pressure data (figure 29) with the baseline wing-nacelle data (figure 18) indicates a similar trend in the local Mach number reduction seen for the $0.6M_0$ test condition.

The interference drag increment due to power for the LEX configuration is approximately 10 counts at $0.6M_0$; however, as Mach number is increased the interference drag increment due to power decreases to a point where at $0.8M_0$, a 10 drag count favorable interference, relative to the unpowered LEX configuration, is seen. Examination of the $0.6M_0$ chordwise pressure distributions (figure 27) indicates that even with the LEX installed noticeable adverse effects due to power still exist. However, at the flow condition for which the LEX was designed, $0.8M_0$, the LEX does a better job of suppressing the inboard pressure peak levels (figure 29). The advantage of the LEX can be clearly seen in figure 30 which shows the powered conditions with and without LEX compared with the clean wing at $0.8M_0$. At ETA = .365 the LEX returns the pressure distributions close to the original clean wing levels. At the ETA = .418 station the LEX did not improve the upper surface suction peak levels compared to those for the unmodified wing, although there is some improvement seen on the lower wing surface pressures at this station. The flow visualization picture given in figure 31 shows the wing with LEX and power at $0.8M_0$.

To help improve the upper surface pressures just inboard of the nacelle a leading-edge fillet section, which is shown in figures 32 and 33, was fabricated at the wing/nacelle intersection. The fillet shape was defined by NASA during the test based on preliminary analysis of selected wind tunnel data without the benefit of any theoretical analysis. As shown in figure 26, the addition of the fillet improved the interference drag at $0.8M_0$. Figure 34 shows the resulting pressure distribution just inboard of the nacelle due to the addition of the fillet. When compared with the wing-LEX configuration, the addition of the fillet lowers the upper surface local Mach number by roughly 0.2.

4.2 Comparison With Theory, Straight Underwing Nacelle

Presently, the three theoretical methods used at DAC to analyze and design wings operating in the presence of a wing mounted propfan are the DAC lifting-line program (Ref.5), the DAC-Neumann panel program (modification of Ref. 6), and the DAC-Jameson 3-D transonic program (modification of Ref. 7).

The lifting-line program has been utilized to evaluate the effects of non-uniform onset flows on the wing induced drag characteristics. This method has been very useful in developing the optimum wing span loading for a particular propeller flow field. The DAC-Neumann program with its capability to handle complex 3-D geometries, as well as simulate propeller onset flows, has been used extensively to develop the engine nacelle and wing geometry at subsonic conditions. The DAC-Jameson program coupled with propeller onset flow effects and empirical transonic nacelle installation effects has been employed to develop the wing transonic flow characteristics.

The usefulness of these design methods is dependent on how well they can actually predict the effects of the nacelle installation and propeller onset flow. The series of comparisons that follow have been assembled in such a manner as to allow a one-to-one comparison between the actual nacelle and power effects as measured in the Ames test and the predicted effects obtained from the theoretical methods described above. For the three configurations on which the majority of the testing was performed (i.e., clean wing, wing-nacelle, and wing-LEX-nacelle) $0.6M_0$ data is compared with results from the DAC-Neumann program and $0.8M_0$ test data is compared with the DAC-Jameson results.

Presently, because of mathematical formulation difficulties, the DAC-Neumann program must be run at zero Mach number when the propfan onset flow is being simulated. In addition, to facilitate the use of the method, particularly when the nacelle is incorporated with the wing geometry, the Neumann solutions have been obtained without considering any viscous corrections to the wing geometry. Based on the above operational constraints and the fact that at low subsonic Mach numbers changes to the flow characteristics over the upper surface and forward position of the wing, due to the addition of a nacelle and power are the most important to predict all DAC-Neumann to experimental correlations have been made at a constant angle-of-attack. Since Mach number and viscous effects are accounted for in the present transonic nacelle and power simulation procedures, the DAC-Jameson correlations with experimental data are shown at constant C_L.

The comparison of the experimental and DAC-Neumann theoretical wing chordwise pressure distributions at $0.6M_0$ for the clean wing configuration is presented in Figure 35. As can be seen, the correlation is very good on the wing upper surface which supports the approach of making comparison at a constant angle-of-attack. For comparison, figure 36, a DAC-Jameson solution is compared to the above $0.6M_0$ data at a constant C_L. The DAC-Jameson calculated pressures are in very close agreement with the experiment data over the entire wing surface. A similar clean wing comparison at $0.8M_0$ is presented in figure 37. In general the DAC-Jameson calculated pressure distribution is in reasonable agreement with the experimental data.

Figure 38 shows the DAC-Neumann and experimental nacelle installation effects on the wing's chordwise pressure distributions just inboard and outboard of the nacelle at $0.6M_0$. As can be seen, the changes to the wing's surface pressure distributions due to the nacelle installation are predicted well by the DAC-Neumann program. Figure 39 presents, at the same wing semispan stations, the comparison of DAC-Jameson and experimental wing chordwise pressure distribution for the wing/nacelle configuration at $0.8M_0$. In general the DAC-Jameson/empirical transonic nacelle simulation procedure correlates well with the experimental data.

The comparison of the DAC-Neumann and experimental propeller slipstream (power) effects on the wing chordwise pressure distributions at $0.6M_0$ is presented in figure 40. The propeller swirl and total pressure ratio characteristics used in the DAC-Neumann power simulation are given in figure 15 of reference 2. These results indicate that the propeller onset flow simulation incorporated in the DAC-Neumann program is properly predicting the experimental power effects. The comparison of the DAC-Jameson and experimental wing chordwise pressure distributions for the powered wing/nacelle configuration at $0.8M_0$ is shown in figure 41. Again, the correlation is quite good except at the 42 percent semispan station where the experimental data is indicating separated flow as shown in the oil flow visualization picture (figure 23). The quality of the above correlation supports the present scheme used in the DAC-Jameson program to simulate propeller power effects.

Figure 42 presents, for the LEX configuration, the nacelle installation effects at $0.6M_0$ measured experimentally and predicted by the DAC-Neumann program. Again, the wing chordwise pressure distribution changes due to installing the nacelle are accurately predicted by the DAC-Neumann program. The DAC-Jameson/experimental comparisons for the straight underwing nacelle and LEX configuration at $0.8M_0$ appear in figure 43. With the exception of the slight over prediction of the suction peak level at ETA = .365 the theory is generally in good agreement with the experimental results.

Figure 44 compares the DAC-Neumann and experimental propeller power effects on the wing chordwise pressure distributions for the LEX configuration at $0.6M_0$. Again, as seen on the baseline wing configuration, the DAC-Neumann power effects simulation technique predicts the experimental results quite accurately, except at the 42 percent wing semispan station where the experimental flow is indicating a separation bubble downstream of its suction peak. Comparison of the DAC-Jameson and experimental chordwise pressure distribution at $0.8M_0$ for the LEX configuration with power is shown in figure 45. Again, the above comparison generally supports the present power effect technique employed in the DAC-Jameson program. As was

the case for the baseline wing, the experimental pressures at the 42 percent semispan span station appear separated as indicated in the flow visualization photograph (figure 31).

Figures 46 through 49 present the changes to the wing span loading due to propeller power effects as measured experimentally and predicted by DAC's current analysis methods. In all cases (i.e., independent of Mach number and wing configuration) the theoretical programs underestimate the increase in the experimental wing span loading in the region inboard of the nacelle. Whereas, in general, the correlation is quite good in the wing region outboard of the nacelle. The poor correlation in the wing region inboard of the nacelle may possibly be attributed to the fact that the experimental flow appears to separate in this region of the wing when power is applied to the propeller and/or due to the chordwise summation of small pressure differences between the theory and experimental data.

5.0 TASK III DATA ANALYSIS AND DESIGN, OVERWING NACELLE

This section describes the inteference drag increments and wing chordwise pressure distribution changes due to the overwing contoured nacelle installation. Data is presented for the baseline wing, baseline wing plus leading edge extension (LEX), and the LEX wing configuration with an inboard nacelle/wing leading-edge fillet developed by NASA personnel during the wind tunnel test. The complete configuration with the LEX and fillet installed is shown in figures 50, 51, and 52. Only unpowered (i.e., propeller off) data was acquired for this configuration, however, a solid body exhaust plume simulation was included in the model geometry. These experimental results are presented in a format similar to that used in the straight underwing nacelle data analysis (Section 4.0). A new contoured overwing nacelle design and a modification to the LEX for the current wind tunnel model design are evaluated. A new AR = 11 wing design for an up-outboard rotation turboprop installation is defined, and an advanced contoured nacelle is provided

5.1 Analysis of Contoured Overwing Nacelle Data

The interference drag increments for the overwing contoured nacelle at $0.5C_L$ are shown in figure 53. Examination of the 0.6 and $0.8M_0$ wing pressure data, presented in figures 54 and 55 respectively, suggests this level of interference drag is due to the increase in wing suction pressure levels inboard of the nacelle, as was the situation for the underwing nacelle installation. The oil flow photograph for the contoured nacelle configuration at $0.8M_0$ (figure 56) shows that the high leading-edge suction peak seen in the pressure distrubutions is producing a local shock, accounting for the increase in drag.

The addition of the LEX wing modification produced essentially no change to the contoured overwing nacelle interference drag levels (except at $0.7M_0$). The inboard wing surface pressure distributions do not fully explain this drag increment since the pressure distribution increments due to the addition of the LEX are very similar for both the contoured nacelle and straight underwing nacelle configurations and, as seen in figures 15 and 26, the LEX reduced the underwing nacelle interference drag level by 10 counts at 0.8M. Figures 54, 55, 57, and 58 present the effect of the LEX on the wing chordwise pressure for both nacelle configurations at 0.6 and $0.8M_0$. The small improvment in drag with the addition of the LEX for the contoured nacelle may be attributed to the complimentary effect of the nacelle contouring and the LEX. Both modifications were designed to reduce the leading edge suction peaks. Since either component by itself will reduce the suction peak there is a less severe condition for the other component to improve. It is therefore appropiate that the effects are not strictly additive.

The addition of the inboard nacelle/wing fillet reduced the nacelle interference drag approximately 10 drag counts relative to the LEX only configuration. This reduction in interference drag occurs because the fillet affects the wing pressures and shock in the region just inboard of the nacelle, as seen in figure 59 for $0.6M_0$ and $0.8M_0$.

5.2 Comparison With Theory, Contoured Overwing Nacelle

The DAC-Neumann and DAC-Jameson analysis methods have been utilized at 0.6 and 0.8 Mach numbers, respectively, to obtain comparisons with the experimental data for the contoured overwing nacelle configurations in a manner similar to the comparisons made for the straight underwing nacelle installations.

Figure 60 presents the DAC-Neumann and $0.6M_Q$ experimental effects of the contoured overwing nacelle on the wing chordwise pressure distribution just inboard and outboard of the nacelle. The changes due to the nacelle installation on the wing surface pressure distributions are generally predicted well by the DAC-Neuman program. The increase in wing leading edge suction peaks just inboard of the nacelle are slightly underestimated by the DAC-Neumann program. Figure 61 presents, at the same wing semispan stations, the comparison of the DAC-Jameson and experimental wing chordwise pressure distributions for the wing/nacelle configuration at 0.8M. As was the case for the underwing nacelle configuration, the DAC-Jameson/emperical transonic nacelle simulation procedure correlates well with the experimental data.

Nacelle installation effects for the LEX wing configuration, as predicted by DAC-Neumann and measured experimentally, are shown in figure 62. Again, the changes to the wing chordwise pressure distribution are adequately predicted by the DAC-Neumann program. The comparison of DAC-Jameson and experimental chordwise pressure distribution at 0.8 Mach number for the LEX/contoured overwing nacelle configuration is presented in figure 63. The correlation for this wing configuration, compared to that for the baseline wing and nacelle (figure 61) is slightly worse in the region inboard of the nacelle; but is acceptable outboard of the nacelle.

5.3 Design Modifications for Overwing Contoured Nacelle

Since the overwing contoured nacelle was not designed for the wing with the LEX, a study was conducted to determine if a better nacelle contouring, including a refined contouring procedure, could be developed that would reduce the wing/lex/nacelle installation drag and would meet constraints imposed by the current model hardware.

Two modified nacelle shapes were defined and analyzed using the DAC Neumann code. These nacelle shapes together with the existing wind tunnel model (baseline) geometry appear in figure 64. The modified baseline nacelle shape was designed subject to constraints of the existing internal hardware and, as a result, appears the same in the side view as the baseline nacelle. The fully contoured nacelle shape was designed using current design technology without any hardware constraints and therefore represents a more optimum design. Figure 65 shows the Neumann pressure comparisons for all three nacelle shapes at the two pressure rows just inboard of the nacelle. While the modified baseline nacelle pressures do not show much improvement over the baseline case, the unconstrained, fully contoured nacelle resulted in a significant reduction in the upper surface suction peaks. The modifications allowable with the physical constraints imposed by the internal hardware did not yield any major improvement in the pressure distributions. Therefore, nacelle modifications for the Ames model are not recommended.

Based on the interference drag level results of the powered testing of the straight underwing nacelle geometry, a modification to the LEX in the area just inboard of the nacelle was investigated. The transonic design and analysis method of reference 5 was used to modify the LEX geometry with the objective of reducing the suction pressure peaks in this region by 0.2. This value is the same decrease obtained with the addition of the fillet to the contoured nacelle LEX geometry which resulted in a 10 count drag reduction. The resulting geometry and corresponding chordwise pressure distributions appear in figures 66 and 67. Wing rework would be required aft of .15x/c to match these shapes to the existing wing.

5.4 New Wing Design

The purpose of the wing design effort was to design a wing which is tailored to minimize the interference drag increments associated with wing mounted up-outboard rotation propfan configurations. This wing would then be complementary to up-inboard work already completed. An existing supercritical wing geometry (Douglas Aircraft Co. Wing W1) with an AR of 11.1, $\Lambda_{C/4}$ of 26 degrees, and taper ratio of .275 was used as a baseline (figure 68). An overwing full chord engine nacelle was specified which is compatible with current installation requirements for a typical low wing airplane application.

As discussed previously, the wing design method currently employed at DAC utilizes a lifting-line program to evaluate the wing induced drag characteristics in the presence of nonuniform onset flows; a 3-D inverse Henne/Jameson program to generate the wing geometry to meet specified chordwise pressure distributions; and a 3-D Neumann program to determine the subsonic nacelle installation effects.

Initially the lifting line program was used to determine the span loading for the wing W1 planform which results in the minimum induced drag with both up-inboard and up-outboard propfan rotation onset flows. As was the case for the data-theory comparisons the propeller characteristics used to determine the onset flow were taken from results of a NASA Lewis PTR test on an isolated Hamilton Standard SR 2 propfan (Appendix A). The resulting drag polars are presented in Figure 69. It was found that the minimum attainable induced drag polar for up-outboard propfan rotation was roughly equal to the baseline W1 wing unpowered value. The 10 count benefit seen for the up-inboard rotation configuration is consistent with results seen in reference 8. From an induced drag standpoint, an up-inboard rotation configuration would appear preferable to the up-outboard rotation design. However, if interference and viscous effects discussed previously in this report, and wing thickness and shape are taken into account, the up-outboard rotation configuration may result in an overall improvement in the installed drag values.

The Henne/Jameson inverse design routine was employed to obtain pressure distributions for the wing operating in the presence of the propeller onset flow which are similar to the unpowered clean wing pressures. The resulting geometry for two of the modified airfoil geometries which lie within the propfan slipstream are shown in figure 70 together with the corresonding camber and thickness distributions. Coordinates for the complete wing defining airfoil sections are given in Table 1. The two airfoil sections are located to be downstream of the 70% installed propfan blade radius

spanwise location. The outboard airfoil section has significantly more camber than the section inboard of the nacelle. This increase in camber helps alleviate the adverse flow effects due to the added propfan upwash outboard of the nacelle. These airfoil modifications outboard of the nacelle are similar to the wing geometry resulting from the addition of the LEX to the wing W4 geometry for the Ames 11-foot test.

Wing thickness distributions for both the modified and baseline wing geometries appear in figure 71. The change in thickness made to the original W1 wing extends from roughly 20 to 70 percent semispan. Inboard and outboard of this section the W1 geometry is maintained.

A contoured nacelle shape was designed to eliminate adverse flow characteristics in the area of the wing-nacelle intersection while at the same time maintaining the internal lines necessary to contain a proposed flight propulsion system. Contouring of the nacelle was accomplished by first tracing several flow streamlines over the clean wing surface with the aid of the 3-D potential flow DAC Neumann code. A single streamline was selected to act as the centerline for the contoured nacelle. An in-house nacelle geometry generation routine was employed to modify a series of predefined nacelle cross sections to follow the selected streamline path. These cross sections are defined to clear the internal drive system and related equipment. Figures 72 and 73 show the resulting contoured nacelle shape compared with the initial straight overwing nacelle geometry. Coordinates for the nacelle defining cross sections are given in Table 2. A top view of the modified wing and contoured overwing nacelle geometry appears in figure 74.

Figures 75 and 76 show the resulting pressure distributions and span loadings for the modified wing geometry with power, compared to the baseline wing W1 with and without power at a configuration C_L of .55. For the wing W1 geometry, the addition of power increases the wing suction pressure peak levels outboard of the nacelle and offloads the leading edge area of the wing inboard of the nacelle. These changes are due to the effect of the up-outboard propfan rotation which increases local angle-of-attack outboard of the nacelle and decreases local angle-of-attack inboard of the nacelle. The resulting pressure distributions for the modified wing with power show that, with proper tailoring of airfoil shape and incidence, the adverse effects due to the propeller onset flow have been eliminated. In addition, the wing leading-edge pressures are off-loaded in the area of the nacelle to add a design margin.

Results of a lifting line induced drag analysis conducted on the modified wing geometry appear in figure 77. The new wing design shows a slight improvement, in induced drag, from both the unpowered and powered baseline wing.

6.0 CONCLUSIONS

- A thrust/drag bookkeeping method is described which is compatible with data available to the engine, propeller and airframe manufacturers, and is recommended for data reduction during future testing. The results of the thrust/drag bookkeeping method comparison show that the difference in the interference drag levels obtained using both methods is, at the most, 18 drag counts at the higher Mach numbers and represents roughly 4% of the total configuration drag.

- The propeller experiences a 13% shift in advance ratio when installed on the aircraft. This shift is due to the differences between the freestream and local(propfan diskplane) flowfield environments.

- Propfan propulsion system interference drag levels near zero are achievable by properly designing the wing to account for the nacelle and power. Modified designs to eliminate remaining flow problem areas can result in additional drag improvements.

- Theoretical methods agree very well with experimental pressure distributions at all Mach numbers and these methods are adequate for design purposes.

- Incremental span loads are adequately predicted outboard of the nacelle, however, discrepancies between data and theory were found inboard of the nacelle. The inboard separated flow regions which are apparent in the chordwise pressure distributions are probably causing this poor correlation. To confirm this assumption additional study is required.

- Analysis of the unpowered contoured overwing nacelle shows that contouring reduces the increase of nacelle interference drag as a function of Mach number.

- The benefits seen for the LEX with the contoured nacelle did not meet the level expected from analysis of the underwing nacelle. This can be explained by the complimentary nature of the two modifications.

- A modified nacelle contouring was evaluated, but hardware constraints prevent attaining any significant improvements.

- A new wing was designed with up-outboard prop rotation. This was selected based on considerations of viscous effects and wing thickness. An advanced, full chord, contoured nacelle was designed for use with the new wing.

7.0 TABLES

TABLE 1

UP-OUTBOARD PROPFAN ROTATION

WING AIRFOIL GEOMETRY

PRECEDING PAGE BLANK NOT FILMED

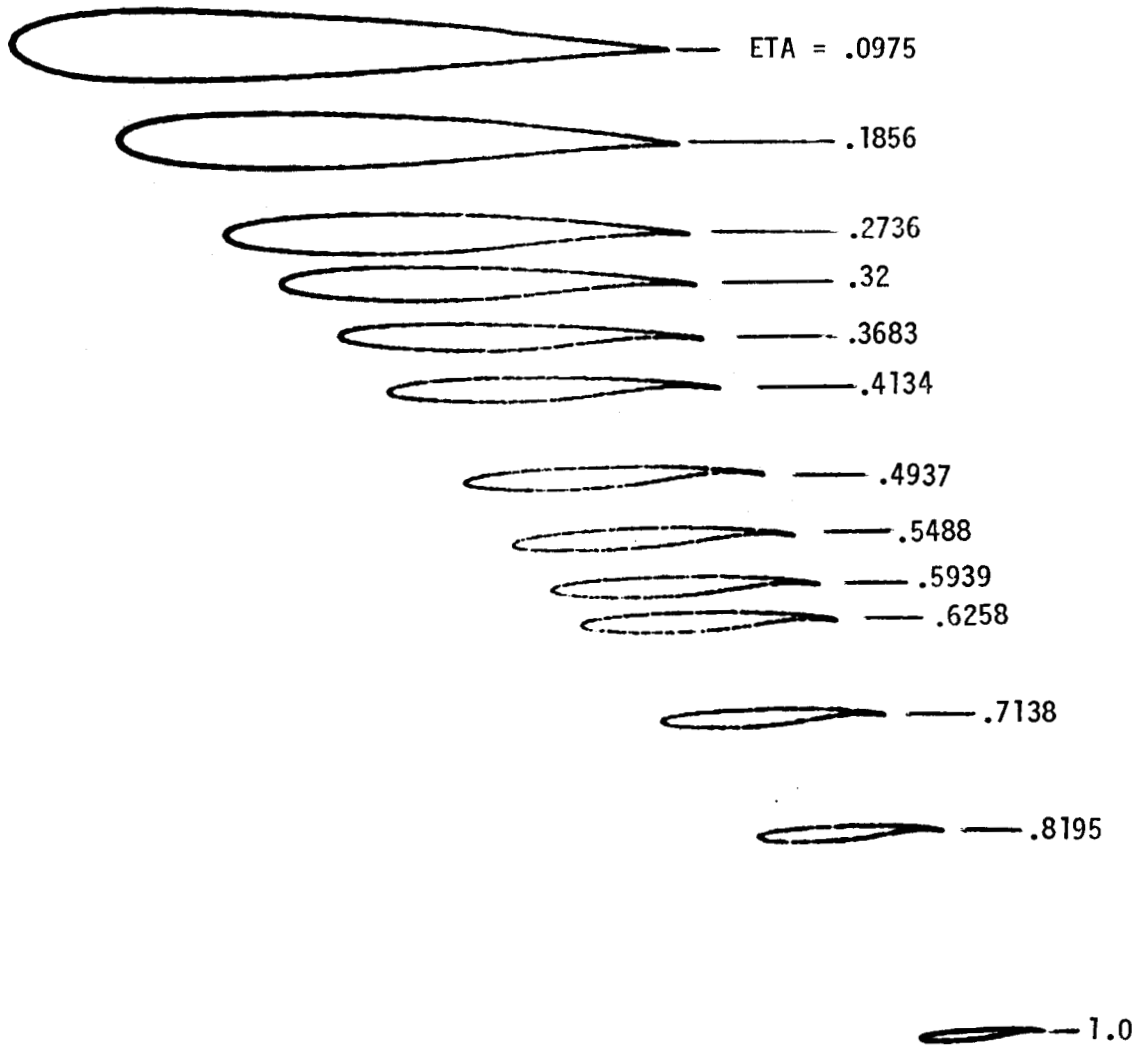

UP-OUTBOARD PROPFAN ROTATION WING AIRFOIL GEOMETRY

ETA = .0975			ETA = .1856		
X	Y	Z	X	Y	Z
290.1074	56.4494	-12.3343	292.8545	107.3989	-9.7807
288.6584	56.4494	-12.0928	291.6306	107.3989	-9.4372
284.3528	56.4494	-11.2776	287.9871	107.3989	-8.4580
277.3018	56.4494	-9.8036	282.0146	107.3989	-6.8477
267.6731	56.4494	-7.8234	273.8516	107.3989	-4.8291
255.7011	56.4494	-5.4408	263.6890	107.3989	-2.6424
241.6803	56.4494	-2.7159	251.7800	107.3989	-0.2897
225.9520	56.4494	0.2076	238.4165	107.3989	2.1481
208.8969	56.4494	3.1276	223.9207	107.3989	4.4697
190.9298	56.4494	5.8724	208.6448	107.3989	6.5254
172.4897	56.4494	8.3093	192.9653	107.3989	8.2702
154.0333	56.4494	10.4307	177.2711	107.3989	9.7187
136.0184	56.4494	12.2469	161.9488	107.3989	10.8390
118.8861	56.4494	13.6673	147.3722	107.3989	11.5331
103.0497	56.4494	14.4912	133.8963	107.3989	11.7030
88.8903	56.4494	14.5243	121.8498	107.3989	11.2854
76.7445	56.4494	13.5312	111.5267	107.3989	10.2351
66.9021	56.4494	11.3577	103.1798	107.3989	8.5473
59.6057	56.4494	8.0636	97.0116	107.3989	6.2068
55.0565	56.4494	4.1445	93.1743	107.3989	3.2772
53.3670	56.4494	-0.2916	91.7756	107.3989	0.0936
54.6011	56.4494	-4.7015	92.8300	107.3989	-3.6650
58.7137	56.4494	-9.2647	96.3598	107.3989	-6.9332
65.6170	56.4494	-13.6050	102.2656	107.3989	-9.8828
75.1635	56.4494	-17.1793	110.4064	107.3989	-12.3508
87.1331	56.4494	-19.6084	120.5818	107.3989	-14.2771
101.2252	56.4494	-20.9494	132.5382	107.3989	-15.6760
117.0732	56.4494	-21.5472	145.9773	107.3989	-16.5887
134.2759	56.4494	-21.5997	160.5659	107.3989	-17.0410
152.4050	56.4494	-21.1975	175.9438	107.3989	-17.0388
171.0078	56.4494	-20.4762	191.7323	107.3989	-16.5857
189.6231	56.4494	-19.5093	207.5430	107.3989	-15.6873
207.7918	56.4494	-18.3396	222.9810	107.3989	-14.4738
225.0616	56.4494	-17.0886	237.6571	107.3989	-13.1633
241.0034	56.4494	-15.8640	251.2017	107.3989	-11.9497
255.2234	56.4494	-14.7205	263.2756	107.3989	-10.9758
267.3665	56.4494	-13.7830	273.5791	107.3989	-10.3232
277.1309	56.4494	-13.1259	281.8601	107.3989	-9.9662
284.2773	56.4494	-12.7442	287.9182	107.3989	-9.8478
288.6311	56.4494	-12.6237	291.6072	107.3989	-9.9100
290.0925	56.4494	-12.6235	292.8447	107.3989	-9.9800

ETA = .2736

X	Y	Z
295.4822	158.3481	-5.4909
294.4729	158.3481	-5.2182
291.4670	158.3481	-4.4871
286.5371	158.3481	-3.3746
279.8040	158.3481	-1.9102
271.4297	158.3481	-0.2379
261.6187	158.3481	1.5457
250.6103	158.3481	3.3286
238.6716	158.3481	4.9616
226.0946	158.3481	6.3407
213.1875	158.3481	7.3961
200.2706	158.3481	8.1670
187.6646	158.3481	8.7136
175.6777	158.3481	8.9580
164.6023	158.3481	8.8197
154.7091	158.3481	8.2389
146.2419	158.3481	7.2336
139.4101	158.3481	5.8608
134.3850	158.3481	4.2411
131.2854	158.3481	2.2699
130.1899	158.3481	0.0609
131.1157	158.3481	-2.6088
134.0748	158.3481	-4.6772
138.9817	158.3481	-6.4528
145.7092	158.3481	-8.0784
154.0913	158.3481	-9.5206
163.9224	158.3481	-10.7256
174.9617	158.3481	-11.6236
186.9394	158.3481	-12.1340
199.5630	158.3481	-12.1752
212.5249	158.3481	-11.6517
225.5074	158.3481	-10.5376
238.1847	158.3481	-9.0364
250.2334	158.3481	-7.5060
261.3469	158.3481	-6.2642
271.2476	158.3481	-5.4759
279.6907	158.3481	-5.1662
286.4731	158.3481	-5.2075
291.4336	158.3481	-5.4489
294.4546	158.3481	-5.7394
295.4683	158.3481	-5.8868

ETA = .32

X	Y	Z
297.4685	185.1767	-4.7442
296.5674	185.1767	-4.5055
293.8838	185.1767	-3.8748
289.4805	185.1767	-2.9390
283.4678	185.1767	-1.6883
275.9893	185.1767	-0.2525
267.2271	185.1767	1.2656
257.3940	185.1767	2.7624
246.7293	185.1767	4.1170
235.4940	185.1767	5.2641
223.9639	185.1767	6.1517
212.4257	185.1767	6.8316
201.1666	185.1767	7.3646
190.4609	185.1767	7.6603
180.5694	185.1767	7.6411
171.7341	185.1767	7.2676
164.1726	185.1767	6.5489
158.0717	185.1767	5.5178
153.5839	185.1767	4.2591
150.8140	185.1767	2.6565
149.8286	185.1767	0.7062
150.6551	185.1767	-1.4594
153.2969	185.1767	-3.1737
157.6802	185.1767	-4.6222
163.6875	185.1767	-6.0159
171.1715	185.1767	-7.3030
179.9493	185.1767	-8.4176
189.8066	185.1767	-9.2863
200.5028	185.1767	-9.8286
211.7769	185.1767	-9.9707
223.3557	185.1767	-9.5991
234.9566	185.1767	-8.6527
246.2889	185.1767	-7.2905
257.0603	185.1767	-5.8850
266.9932	185.1767	-4.7905
275.8376	185.1767	-4.1795
283.3760	185.1767	-4.0665
289.4280	185.1767	-4.2994
293.8521	185.1767	-4.6937
296.5457	185.1767	-5.0710
297.4492	185.1767	-5.2442

ETA =.3683

X	Y	Z
299.5388	213.1270	-3.9665
298.7507	213.1270	-3.7632
296.4021	213.1270	-3.2370
292.5471	213.1270	-2.4852
287.2839	213.1270	-1.4571
280.7383	213.1270	-0.2673
273.0676	213.1270	0.9742
264.4583	213.1270	2.1731
255.1194	213.1270	3.2376
245.2808	213.1270	4.1430
235.1844	213.1270	4.8557
225.0824	213.1270	5.4406
215.2270	213.1270	5.9594
205.8567	213.1270	6.3089
197.1994	213.1270	6.4135
189.4676	213.1270	6.2556
182.8516	213.1270	5.8357
177.5141	213.1270	5.1612
173.5879	213.1270	4.2787
171.1633	213.1270	3.0661
170.2925	213.1270	1.3788
171.0172	213.1270	-0.2756
173.3306	213.1270	-1.6065
177.1696	213.1270	-2.7192
182.4274	213.1270	-3.8691
188.9758	213.1270	-4.9942
196.6561	213.1270	-6.0143
205.2814	213.1270	-6.8517
214.6417	213.1270	-7.4281
224.5091	213.1270	-7.6742
234.6460	213.1270	-7.4595
244.8073	213.1270	-6.6886
254.7387	213.1270	-5.4708
264.1799	213.1270	-4.1950
272.8828	213.1270	-3.2544
280.6262	213.1270	-2.8339
287.2202	213.1270	-2.9194
292.5093	213.1270	-3.3542
296.3728	213.1270	-3.9071
298.7239	213.1270	-4.3747
299.5125	213.1270	-4.5746

ETA = .4134

X	Y	Z
304.8037	239.2250	-2.7197
304.0823	239.2250	-2.5266
301.9338	239.2250	-2.0274
298.4099	239.2250	-1.3360
293.5979	239.2250	-0.4241
287.6147	239.2250	0.5873
280.6060	239.2250	1.5921
272.7432	239.2250	2.5099
264.2195	239.2250	3.2715
255.2447	239.2250	3.8699
246.0395	239.2250	4.2771
236.8319	239.2250	4.5454
227.8493	239.2250	4.7171
219.3116	239.2250	4.7136
211.4283	239.2250	4.4945
204.3933	239.2250	4.0493
198.3798	239.2250	3.3941
193.5361	239.2250	2.5531
189.9821	239.2250	1.5830
187.8039	239.2250	0.4283
187.0548	239.2250	-0.8970
187.7534	239.2250	-2.3553
189.8925	239.2250	-3.3595
193.4143	239.2250	-4.1657
198.2279	239.2250	-4.9819
204.2155	239.2250	-5.7558
211.2301	239.2250	-6.4368
219.0998	239.2250	-6.9657
227.6320	239.2250	-7.2671
236.6178	239.2250	-7.2603
245.8381	239.2250	-6.8309
255.0677	239.2250	-5.8914
264.0779	239.2250	-4.5376
272.6406	239.2250	-3.1444
280.5391	239.2250	-2.1020
287.5750	239.2250	-1.6003
293.5757	239.2250	-1.6537
298.3962	239.2250	-2.0913
301.9224	239.2250	-2.6646
304.0710	239.2250	-3.1427
304.7925	239.2250	-3.3440

ETA = .4937

X	Y	Z
319.6018	285.7209	-0.0330
318.9441	285.7209	0.1507
316.9878	285.7209	0.6158
313.7822	285.7209	1.2027
309.4062	285.7209	1.9398
303.9680	285.7209	2.7481
297.6021	285.7209	3.5266
290.4656	285.7209	4.2009
282.7344	285.7209	4.7141
274.5994	285.7209	5.0614
266.2603	285.7209	5.2351
257.9226	285.7209	5.2264
249.7919	285.7209	5.0531
242.0677	285.7209	4.7363
234.9405	285.7209	4.2811
228.5858	285.7209	3.6846
223.1604	285.7209	2.9236
218.7982	285.7209	1.9933
215.6061	285.7209	0.9609
213.6624	285.7209	-0.0978
213.0153	285.7209	-1.1971
213.6811	285.7209	-2.3687
215.6401	285.7209	-3.1803
218.8460	285.7209	-3.8292
223.2210	285.7209	-4.4513
228.6571	285.7209	-4.9933
235.0203	285.7209	-5.4288
242.1536	285.7209	-5.7158
249.8810	285.7209	-5.7840
258.0112	285.7209	-5.5590
266.3440	285.7209	-4.9500
274.6726	285.7209	-3.8493
282.7925	285.7209	-2.3327
290.5063	285.7209	-0.7720
297.6274	285.7209	0.4326
303.9817	285.7209	1.0771
309.4133	285.7209	1.0817
313.7869	285.7209	0.6533
316.9922	285.7209	0.0694
318.9487	285.7209	-0.4106
319.6067	285.7209	-0.6092

ETA = .5488

X	Y	Z
329.9924	317.5776	-0.2747
329.3752	317.5776	-0.0629
327.5398	317.5776	0.4694
324.5334	317.5776	1.1367
320.4299	317.5776	1.9359
315.3315	317.5776	2.7829
309.3643	317.5776	3.5706
302.6760	317.5776	4.2245
295.4316	317.5776	4.7074
287.8093	317.5776	5.0260
279.9971	317.5776	5.1558
272.1873	317.5776	5.0730
264.5720	317.5776	4.7966
257.3389	317.5776	4.3584
250.6656	317.5776	3.7599
244.7167	317.5776	3.0172
239.6387	317.5776	2.1494
235.5564	317.5776	1.1840
232.5705	317.5776	0.1420
230.7536	317.5776	-0.8707
230.1492	317.5776	-1.7362
230.7786	317.5776	-2.9724
232.6161	317.5776	-3.6820
235.6210	317.5776	-4.2292
239.7206	317.5776	-4.7211
244.8137	317.5776	-5.1151
250.7749	317.5776	-5.4009
257.4570	317.5776	-5.5499
264.6951	317.5776	-5.5105
272.3101	317.5776	-5.2173
280.1135	317.5776	-4.6066
287.9121	317.5776	-3.5856
295.5144	317.5776	-2.2211
302.7363	317.5776	-0.8315
309.4041	317.5776	0.2295
315.3555	317.5776	0.7783
320.4438	317.5776	0.7638
324.5425	317.5776	0.3604
327.5476	317.5776	-0.1855
329.3818	317.5776	-0.6327
329.9990	317.5776	-0.8159

ETA = .5939

X	Y	Z
338.6877	343.6768	0.0671
338.1067	343.6768	0.2660
336.3772	343.6768	0.7708
333.5413	343.6768	1.4113
329.6689	343.6768	2.1740
324.8550	343.6768	2.9894
319.2175	343.6768	3.7627
312.8953	343.6768	4.4299
306.0442	343.6768	4.9594
298.8325	343.6768	5.3496
291.4377	343.6768	5.5732
284.0422	343.6768	5.6197
276.8281	343.6768	5.5172
269.9731	343.6768	5.2904
263.6460	343.6768	4.9395
258.0024	343.6768	4.4637
253.1816	343.6768	3.8549
249.3017	343.6768	3.1103
246.4584	343.6768	2.2449
244.7218	343.6768	1.2857
244.1348	343.6768	0.2778
244.7114	343.6768	-0.8070
246.4390	343.6768	-1.6752
249.2745	343.6768	-2.3827
253.1474	343.6768	-3.0469
257.9624	343.6768	-3.6263
263.6013	343.6768	-4.1008
269.9250	343.6768	-4.4409
276.7781	343.6768	-4.5863
283.9924	343.6768	-4.4693
291.3904	343.6768	-4.0029
298.7905	343.6768	-3.1029
306.0105	343.6768	-1.8422
312.8708	343.6768	-0.5290
319.2012	343.6768	0.4883
324.8452	343.6768	1.0200
329.6631	343.6768	1.0152
333.5376	343.6768	0.6395
336.3740	343.6768	0.1293
338.1040	343.6768	-0.2831
338.6853	343.6768	-0.4483

ETA = .6258

X	Y	Z
344.6692	362.1445	-0.3359
344.1128	362.1445	-0.1341
342.4565	362.1445	0.3810
339.7402	362.1445	1.0470
336.0303	362.1445	1.8296
331.4180	362.1445	2.6579
326.0159	362.1445	3.4381
319.9570	362.1445	4.1091
313.3901	362.1445	4.6443
306.4775	362.1445	5.0435
299.3887	362.1445	5.2772
292.2986	362.1445	5.3351
285.3816	362.1445	5.2452
278.8088	362.1445	5.0379
272.7415	362.1445	4.7139
267.3293	362.1445	4.2644
262.7051	362.1445	3.6809
258.9829	362.1445	2.9724
256.2542	362.1445	2.1561
254.5859	362.1445	1.2024
254.0192	362.1445	0.1714
254.5679	362.1445	-0.9575
256.2207	362.1445	-1.8650
258.9363	362.1445	-2.5988
262.6472	362.1445	-3.2723
267.2615	362.1445	-3.8522
272.6663	362.1445	-4.3211
278.7280	362.1445	-4.6551
285.2979	362.1445	-4.8045
292.2148	362.1445	-4.6987
299.3093	362.1445	-4.2476
306.4072	362.1445	-3.3851
313.3333	362.1445	-2.1937
319.9148	362.1445	-0.9562
325.9873	362.1445	0.0020
331.3999	362.1445	0.5014
336.0193	362.1445	0.5055
339.7329	362.1445	0.1657
342.4509	362.1445	-0.3051
344.1082	362.1445	-0.6838
344.6650	362.1445	-0.8329

ETA = .7138

X	Y	Z
361.4495	413.0933	0.7638
360.9570	413.0933	0.9207
359.4924	413.0933	1.3350
357.0920	413.0933	1.8976
353.8157	413.0933	2.5535
349.7444	413.0933	3.2214
344.9785	413.0933	3.8210
339.6357	413.0933	4.3070
333.8479	413.0933	4.6644
327.7573	413.0933	4.8949
321.5137	413.0933	4.9842
315.2710	413.0933	4.9401
309.1831	413.0933	4.7743
303.3992	413.0933	4.5080
298.0620	413.0933	4.1538
293.3032	413.0933	3.7153
289.2397	413.0933	3.1863
285.9717	413.0933	2.5660
283.5801	413.0933	1.8579
282.1238	413.0933	0.9977
281.6392	413.0933	0.0034
282.1370	413.0933	-0.9837
283.6042	413.0933	-1.8095
286.0049	413.0933	-2.4480
289.2805	413.0933	-2.9881
293.3503	413.0933	-3.4244
298.1145	413.0933	-3.7485
303.4551	413.0933	-3.9390
309.2407	413.0933	-3.9639
315.3286	413.0933	-3.7559
321.5681	413.0933	-3.2390
327.8052	413.0933	-2.3645
333.8867	413.0933	-1.2096
339.6646	413.0933	-0.0247
344.9978	413.0933	0.8955
349.7563	413.0933	1.3888
353.8232	413.0933	1.4165
357.0972	413.0933	1.1360
359.4963	413.0933	0.7348
360.9604	413.0933	0.4174
361.4526	413.0933	0.2988

ETA = .8195

X	Y	Z
381.1624	474.2329	1.4374
380.7522	474.2329	1.5443
379.5327	474.2329	1.8440
377.5339	474.2329	2.3097
374.8066	474.2329	2.8473
371.4197	474.2329	3.3653
367.4570	474.2329	3.8048
363.0168	474.2329	4.1398
358.2083	474.2329	4.3652
353.1492	474.2329	4.4869
347.9646	474.2329	4.5062
342.7815	474.2329	4.4322
337.7278	474.2329	4.2687
332.9280	474.2329	4.0199
328.5000	474.2329	3.6908
324.5530	474.2329	3.2884
321.1843	474.2329	2.8189
318.4771	474.2329	2.2781
316.4985	474.2329	1.6498
315.2988	474.2329	0.8798
314.9072	474.2329	0.0002
315.3313	474.2329	-0.8690
316.5583	474.2329	-1.5839
318.5583	474.2329	-2.1127
321.2832	474.2329	-2.5238
324.6663	474.2329	-2.8309
328.6245	474.2329	-3.0329
333.0601	474.2329	-3.1123
337.8633	474.2329	-3.0506
342.9153	474.2329	-2.7977
348.0906	474.2329	-2.2978
353.2603	474.2329	-1.5119
358.2983	474.2329	-0.5013
363.0837	474.2329	0.5289
367.5029	474.2329	1.3319
371.4492	474.2329	1.7731
374.8257	474.2329	1.8253
377.5464	474.2329	1.6318
379.5420	474.2329	1.3337
380.7605	474.2329	1.0986
381.1702	474.2329	1.0162

ETA = 1.0

X	Y	Z
416.1240	578.6787	2.6707
415.8425	578.6787	2.7350
415.0063	578.6787	2.9097
413.6370	578.6787	3.1718
411.7708	578.6787	3.4643
409.4568	578.6787	3.7281
406.7539	578.6787	3.9254
403.7290	578.6787	4.0398
400.4568	578.6787	4.0712
397.0171	578.6787	4.0244
393.4949	578.6787	3.9036
389.9763	578.6787	3.7163
386.5479	578.6787	3.4715
383.2939	578.6787	3.1761
380.2947	578.6787	2.8369
377.6240	578.6787	2.4617
375.3477	578.6787	2.0563
373.5225	578.6787	1.6210
372.1943	578.6787	1.1481
371.3989	578.6787	0.5997
371.1550	578.6787	-0.0004
371.4648	578.6787	-0.5722
372.3164	578.6787	-1.0192
373.6882	578.6787	-1.3240
375.5496	578.6787	-1.5328
377.8557	578.6787	-1.6554
380.5496	578.6787	-1.6925
383.5647	578.6787	-1.6365
386.8262	578.6787	-1.4744
390.2517	578.6787	-1.1765
393.7542	578.6787	-0.7064
397.2458	578.6787	-0.0415
400.6423	578.6787	0.7734
403.8665	578.6787	1.5957
406.8479	578.6787	2.2556
409.5171	578.6787	2.6569
411.8093	578.6787	2.7799
413.6624	578.6787	2.7188
415.0256	578.6787	2.5659
415.8594	578.6787	2.4360
416.1399	578.6787	2.3895

TABLE 2

UP-OUTBOARD PROPFAN ROTATION OVERWING

CONTOURED NACELLE GEOMETRY

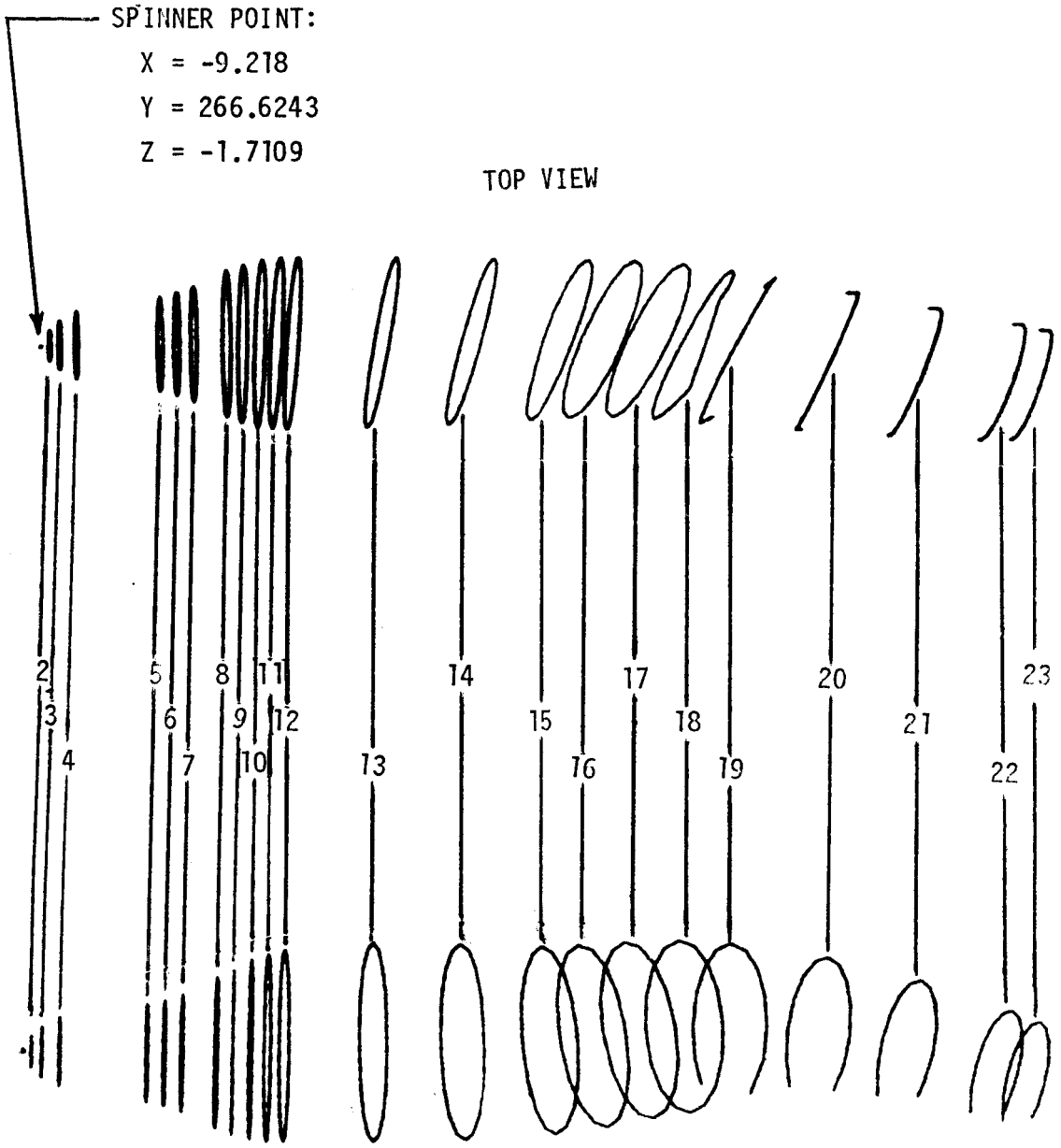

UP-OUTBOARD PROPFAN ROTATION OVERWING CONTOURED NACELLE GEOMETRY

2

X	Y	Z
-7.2039	266.6660	3.3132
-7.2212	268.5410	2.9408
-7.1929	270.1313	1.8804
-7.1234	271.1953	0.2934
-7.0233	271.5706	-1.5787
-6.9079	271.1997	-3.4507
-6.7945	270.1396	-5.0378
-6.7007	268.5518	-6.0982
-6.6406	266.6775	-6.4706
-6.6233	264.8022	-6.0982
-6.6516	263.2117	-5.0378
-6.7211	262.1477	-3.4507
-6.8212	261.7727	-1.5787
-6.9367	262.1433	0.2934
-7.0500	263.2036	1.8804
-7.1438	264.7915	2.9408
-7.2039	266.6660	3.3132

3

X	Y	Z
-4.1824	266.7283	6.4923
-4.2102	269.7515	5.8919
-4.1646	272.3157	4.1822
-4.0526	274.0310	1.6235
-3.8912	274.6357	-1.3947
-3.7050	274.0383	-4.4129
-3.5223	272.3289	-6.9716
-3.3710	269.7688	-8.6813
-3.2741	266.7471	-9.2816
-3.2463	263.7236	-8.6813
-3.2919	261.1592	-6.9716
-3.4039	259.4438	-4.4129
-3.5653	258.8391	-1.3947
-3.7515	259.4368	1.6235
-3.9341	261.1460	4.1822
-4.0354	263.7063	5.8919
-4.1824	266.7283	6.4923

4

X	Y	Z
1.1464	266.8381	9.6039
1.1088	270.9329	8.7907
1.1705	274.4062	6.4751
1.3222	276.7295	3.0095
1.5408	277.5486	-1.0784
1.7930	276.7390	-5.1664
2.0404	274.4241	-8.6320
2.2453	270.9563	-10.9476
2.3766	266.8635	-11.7607
2.4143	262.7688	-10.9476
2.3525	259.2954	-8.6320
2.2008	256.9724	-5.1664
1.9822	256.1531	-1.0784
1.7301	256.9626	3.0095
1.4827	259.2773	6.4751
1.2777	262.7454	8.7907
1.1464	266.8381	9.6039

5

X	Y	Z
28.0427	267.3931	15.5605
27.9895	273.1716	14.4130
28.0767	278.0732	11.1452
28.2908	281.3516	6.2545
28.5992	282.5076	0.4855
28.9551	281.3655	-5.2834
29.3043	278.0986	-10.1741
29.5935	273.2046	-13.4419
29.7788	267.4290	-14.5895
29.8319	261.6501	-13.4419
29.7448	256.7485	-10.1741
29.5307	253.4704	-5.2834
29.2222	252.3144	0.4855
28.8663	253.4567	6.2545
28.5172	256.7231	11.1452
28.2279	261.6172	14.4130
28.0427	267.3931	15.5605

6

X	Y	Z
33.3636	267.5029	17.0690
33.3063	273.7407	15.8303
33.4003	279.0317	12.3028
33.6314	282.5708	7.0235
33.9644	283.8186	0.7960
34.3486	282.5854	-5.4314
34.7254	279.0591	-10.7107
35.0376	273.7764	-14.2383
35.2377	267.5415	-15.4770
35.2950	261.3037	-14.2383
35.2010	256.0125	-10.7107
34.9699	252.4737	-5.4314
34.6369	251.2258	0.7960
34.2527	252.4589	7.0235
33.8758	255.9853	12.3028
33.5636	261.2678	15.8303
33.3636	267.5029	17.0690

7

X	Y	Z
38.8382	267.6160	19.3877
38.7741	274.5806	18.0046
38.8791	280.4885	14.0659
39.1372	284.4399	8.1712
39.5090	285.8335	1.2179
39.9437	284.4568	-5.8353
40.3645	280.5193	-11.7300
40.7131	274.6206	-15.6687
40.9364	267.6592	-17.0518
41.0004	260.6941	-15.6687
40.8954	254.7864	-11.7300
40.6374	250.8349	-5.8353
40.2656	249.4416	1.1180
39.8309	250.8183	8.1712
39.4100	254.7557	14.0659
39.0614	260.6541	18.0046
38.8382	267.6160	19.3877

8

X	Y	Z
49.3076	267.8318	25.3997
49.2266	276.6335	23.6519
49.3593	284.0999	18.6744
49.6854	289.0933	11.2250
50.1553	290.8542	2.4379
50.7376	289.1150	-7.0481
51.2694	284.1392	-14.4975
51.7100	276.6848	-19.4750
51.9922	267.8872	-21.2229
52.0731	259.0852	-19.4750
51.9404	251.6194	-14.4975
51.6143	246.6259	-7.0481
51.1444	244.8650	1.7390
50.5621	246.6042	11.2250
50.0303	251.5800	18.6744
49.5898	259.0342	23.6519
49.3076	267.8318	25.3997

9

X	Y	Z
54.3491	267.9687	27.7972
54.4464	277.4592	25.9118
54.7515	285.5046	20.5446
55.2179	290.8806	12.5124
55.7746	292.7683	3.0382
55.8335	292.7683	2.0400
56.3958	290.8806	-7.4339
56.8779	285.5046	-15.4651
57.2067	277.4592	-20.8310
57.3319	267.9687	-22.7147
57.2346	258.4783	-20.8294
56.9295	250.4326	-15.4621
56.4631	245.0567	-7.4299
55.9064	243.1690	2.0443
55.8475	243.1690	3.0425
55.2852	245.0567	12.5164
54.8031	250.4326	20.5476
54.4743	258.4783	25.9135
54.3491	267.9687	27.7972

10

X	Y	Z
59.6975	268.0894	31.5240
60.0101	278.1135	29.5450
60.5173	286.6121	23.8859
61.1417	292.2903	15.4083
61.7885	294.2844	5.4028
61.9706	294.2844	2.4084
62.5411	292.2903	-7.6018
62.9485	286.6121	-16.0926
63.1309	278.1135	-21.7714
63.0604	268.0894	-23.7737
62.7477	258.0649	-21.7947
62.2406	249.5666	-16.1356
61.6161	243.8882	-7.6580
60.9694	241.8942	2.3475
60.7873	241.8942	5.3420
60.2168	243.8882	15.3521
59.8093	249.5666	23.8428
59.6270	258.0649	29.5217
59.6975	268.0894	31.5240

11

X	Y	Z
64.8300	268.2068	33.6941
65.3507	278.4165	31.6903
66.0461	287.0723	25.9347
66.8104	292.8557	17.3035
67.5271	294.8867	7.1108
67.7989	294.8867	2.7692
68.3590	292.8557	-7.4334
68.6771	287.0723	-16.0925
68.7050	278.4165	-21.8899
68.4382	268.2068	-23.9430
67.9175	257.9968	-21.9392
67.2220	249.3412	-16.1835
66.4578	243.5577	-7.5524
65.7411	241.5267	2.6404
65.4693	241.5267	6.9819
64.9092	243.5577	17.1845
64.5910	249.3412	25.8436
64.5632	257.9968	31.6410
64.8300	268.2068	33.6941

12

X	Y	Z
69.8849	268.3254	35.3682
70.6062	278.5642	33.3704
71.4803	287.2441	27.6052
72.3741	293.0439	18.9503
73.1515	295.0806	8.7232
73.5119	295.0806	3.1348
74.0546	293.0439	-7.1074
74.2799	287.2441	-15.8054
74.1535	278.5642	-21.6351
73.6947	268.3254	-23.7090
72.9734	258.0864	-21.7112
72.0992	249.4065	-15.9461
71.2054	243.6069	-7.2911
70.4280	241.5702	2.9360
70.0676	241.5702	8.5244
69.5250	243.6069	18.7666
69.2997	249.4065	27.4646
69.4261	258.0864	33.2943
69.8849	268.3254	35.3682

13

X	Y	Z
97.1578	269.0217	39.6049
98.9257	279.1108	37.7048
100.7421	287.6643	32.0417
102.3306	293.3794	23.4776
103.4493	295.3865	13.3163
104.0746	295.3865	5.3407
104.5531	293.3794	-4.8707
104.3187	287.6643	-13.5778
103.4070	279.1108	-19.4548
101.9569	269.0217	-21.6072
100.1890	258.9324	-19.7071
98.3726	250.3791	-14.0439
96.7841	244.6639	-5.4798
95.6654	242.6570	4.6815
95.0401	242.6570	12.6570
94.5616	244.6639	22.8685
94.7960	250.3791	31.5755
95.7076	258.9324	37.4525
97.1578	269.0217	39.6049

14

X	Y	Z
124.2681	269.8396	41.1261
127.0502	279.7246	39.3725
129.8298	288.1047	33.8428
132.1839	293.7043	25.3791
133.7540	295.6707	15.2698
134.4896	295.6707	8.2080
135.0367	293.7043	-2.0080
134.4775	288.1047	-10.7752
132.8972	279.7246	-16.7589
130.5363	269.8396	-19.0483
127.7542	259.9543	-17.2946
124.9745	251.5743	-11.7651
122.6205	245.9749	-3.3013
121.0504	244.0085	6.8081
120.3148	244.0085	13.8699
119.7677	245.9749	24.0858
120.3268	251.5743	32.8530
121.9072	259.9543	38.8367
124.2681	269.8396	41.1261

15

X	Y	Z
150.3350	270.7959	42.2876
154.1013	280.4033	40.8594
157.9676	288.5483	35.6400
161.3453	293.9905	27.4239
163.7202	295.9016	17.4621
164.5319	295.9016	12.6298
165.5424	293.9905	2.4387
165.0347	288.5483	-6.4300
163.0860	280.4033	-12.6263
159.9932	270.7959	-15.2067
156.2269	261.1882	-13.7785
152.3606	253.0434	-8.5591
148.9829	247.6012	-0.3430
146.6080	245.6900	9.6188
145.7962	245.6900	14.4511
144.7857	247.6012	24.6422
145.2935	253.0434	33.5109
147.2421	261.1882	39.7072
150.3350	270.7959	42.2876

16

X	Y	Z
162.3763	271.1868	43.4952
166.6197	280.5981	42.4312
171.1621	288.5771	37.5914
175.3120	293.9084	29.7127
178.4374	295.7805	19.9943
179.3241	295.7805	16.2992
180.9494	293.9084	6.2209
180.8269	288.5771	-2.6832
178.9755	280.5981	-9.0573
175.6770	271.1868	-11.9312
171.4335	261.7751	-10.8672
166.8911	253.7964	-6.0274
162.7412	248.4649	1.8514
159.6158	246.5929	11.5698
158.7291	246.5929	15.2649
157.1038	248.4649	25.3432
157.2264	253.7964	34.2472
159.0778	261.7751	40.6214
162.3763	271.1868	43.4952

17

X	Y	Z
176.4236	270.9456	45.5252
181.0272	280.1130	44.5949
185.8961	287.8850	39.9049
190.2889	293.0781	32.1693
193.5369	294.9016	22.5656
194.1378	294.9016	20.1383
195.7465	293.0781	10.1292
195.4709	287.8850	1.2375
193.3531	280.1130	-5.1825
189.7155	270.9456	-8.1535
185.1118	261.7778	-7.2232
180.2430	254.0060	-2.5332
175.8501	248.8129	5.2025
172.6022	246.9893	14.8062
172.0013	246.9893	17.2329
170.3926	248.8129	27.2425
170.6682	254.0060	36.1342
172.7859	261.7778	42.5542
176.4236	270.9456	45.5252

18

X	Y	Z
193.2558	269.8447	47.2171
198.0875	278.7566	45.9019
202.7557	286.3123	40.8395
206.5494	291.3606	32.8005
208.8912	293.1333	23.0088
209.0489	293.1333	21.9201
209.5822	291.9526	11.8664
208.2259	288.5906	3.0813
205.1863	283.5581	-3.0978
200.9265	269.8447	-5.7301
196.0947	256.1309	-4.4149
191.4265	251.0988	0.6475
187.6328	247.7366	8.6865
185.2910	246.5560	18.4782
185.1333	246.5560	19.5669
184.6000	248.3287	29.6206
185.9564	253.3771	38.4057
188.9959	260.9326	44.5848
193.2558	269.8447	47.2171

19

X	Y	Z
203.7980	247.6231	3.3964
201.0166	246.0843	11.1786
199.5693	245.5047	20.9073
199.8554	247.2450	31.0380
201.8637	252.2007	39.4748
205.2708	259.6172	45.2329
209.5582	268.3660	47.4356
214.0730	277.1145	45.7476
218.1280	284.5312	40.4258
221.1058	289.4868	32.2805
222.5706	291.2271	22.2522
222.2670	290.6475	12.4211
218.9035	288.1243	1.5566

20

X	Y	Z
231.2213	243.7296	4.6902
229.5094	243.7258	13.0536
229.1831	243.7258	22.1098
230.3605	245.3600	31.3965
232.8371	250.0143	38.9462
236.2493	256.9795	43.9092
240.0778	265.1958	45.5300
243.7398	273.4119	43.5617
246.6778	280.3772	38.3040
248.4445	285.0315	30.5574
248.7569	286.6658	21.2016
247.5933	286.6658	12.2145
244.9967	286.6809	4.5332

21

X	Y	Z
258.7842	242.0561	3.8350
258.2595	242.0341	11.9376
258.7646	242.0341	20.2116
260.5046	243.5559	28.3264
263.2129	247.8893	35.0284
266.4778	254.3748	39.3071
269.8027	262.0249	40.5112
272.6809	269.6748	38.4573
274.6748	276.1604	33.4582
275.4807	280.4937	26.2748
274.9746	282.0156	17.9908
273.2356	282.0156	9.8859
271.4307	281.9805	4.6505

22			23		
X	Y	Z	X	Y	Z
287.9004	241.1779	0.6556	298.1560	241.4208	-1.1110
287.6294	241.1805	8.1048	297.7847	241.4403	6.5725
288.5056	241.1805	15.4556	298.4824	241.4403	13.5172
290.3704	242.5616	22.6504	300.0767	242.7492	20.3123
292.9314	246.4949	28.5394	302.3242	246.4763	25.9235
295.8035	252.3811	32.2555	304.8833	252.0542	29.4963
298.5493	259.3247	33.2331	307.3645	258.6338	30.4870
300.7510	266.2681	31.3232	309.3892	265.2131	28.7447
302.0735	272.1545	26.8166	310.6499	270.7910	24.5346
302.3152	276.0876	20.3995	310.9548	274.5183	18.4977
301.4341	277.4687	13.0193	310.2568	275.8271	11.5530
299.5742	277.4687	5.8539	308.6628	275.8271	4.7579
298.4993	277.3857	1.9943	306.9634	275.8218	0.4535

8.0 APPENDICES

PRECEDING PAGE BLANK NOT FILMED

PAGE 44 INTENTIONALLY BLANK

APPENDIX A

EXPERIMENTAL SR-2C

ISOLATED PROPELLER PERFORMANCE

OBTAINED AT NASA LEWIS

PRELIMINARY DATA

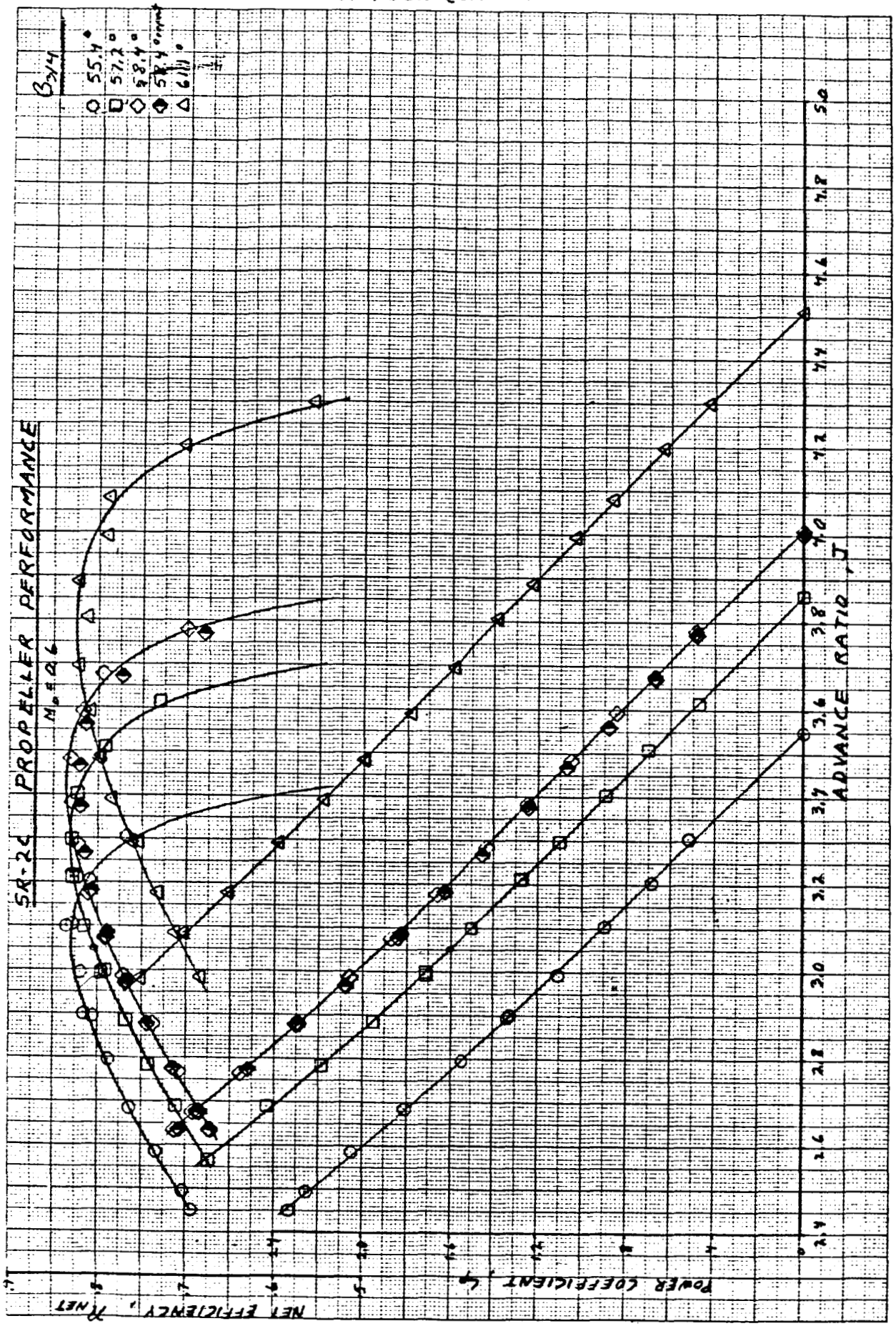

PAGE 46 INTENTIONALLY BLANK

PRELIMINARY DATA

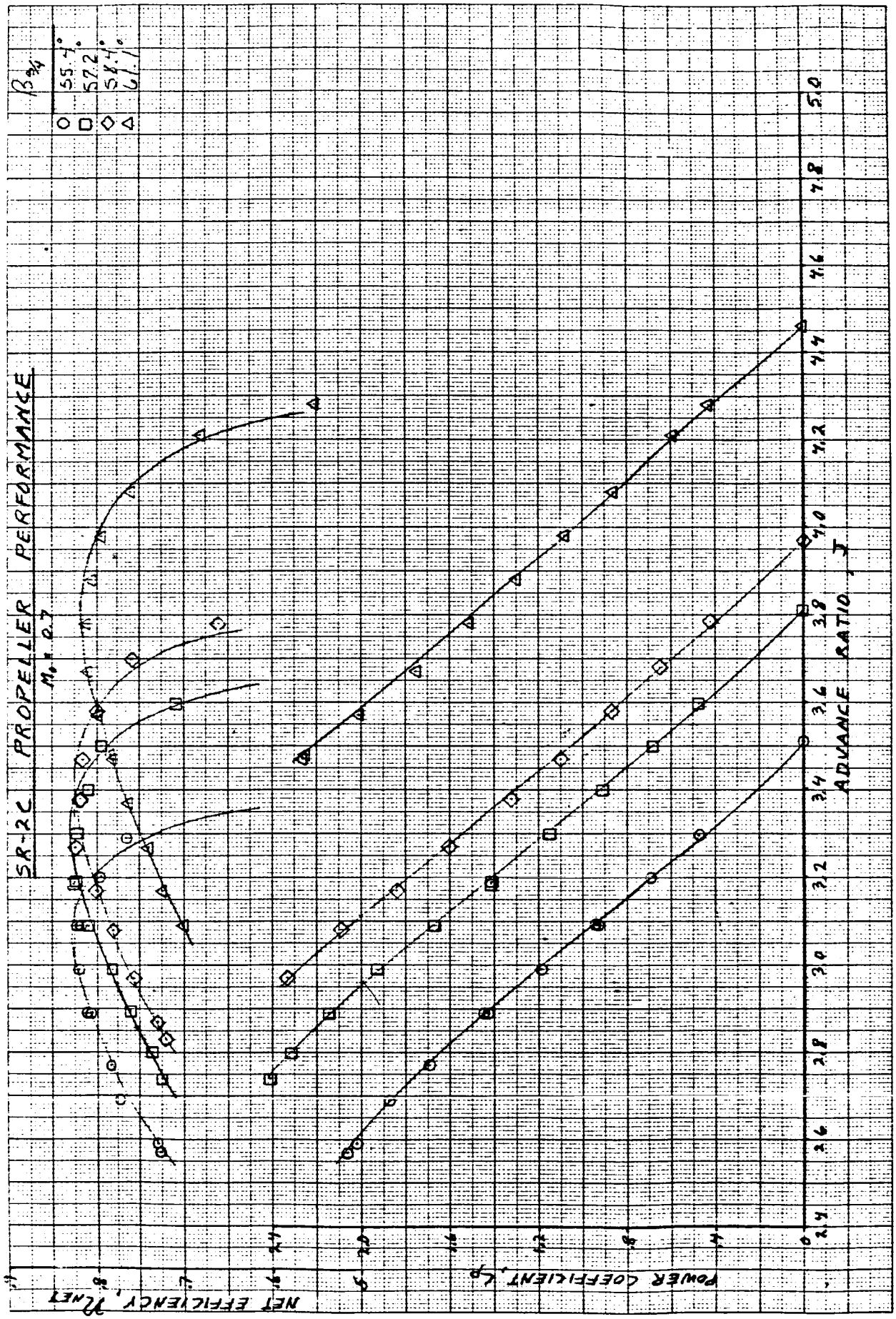

PRELIMINARY DATA

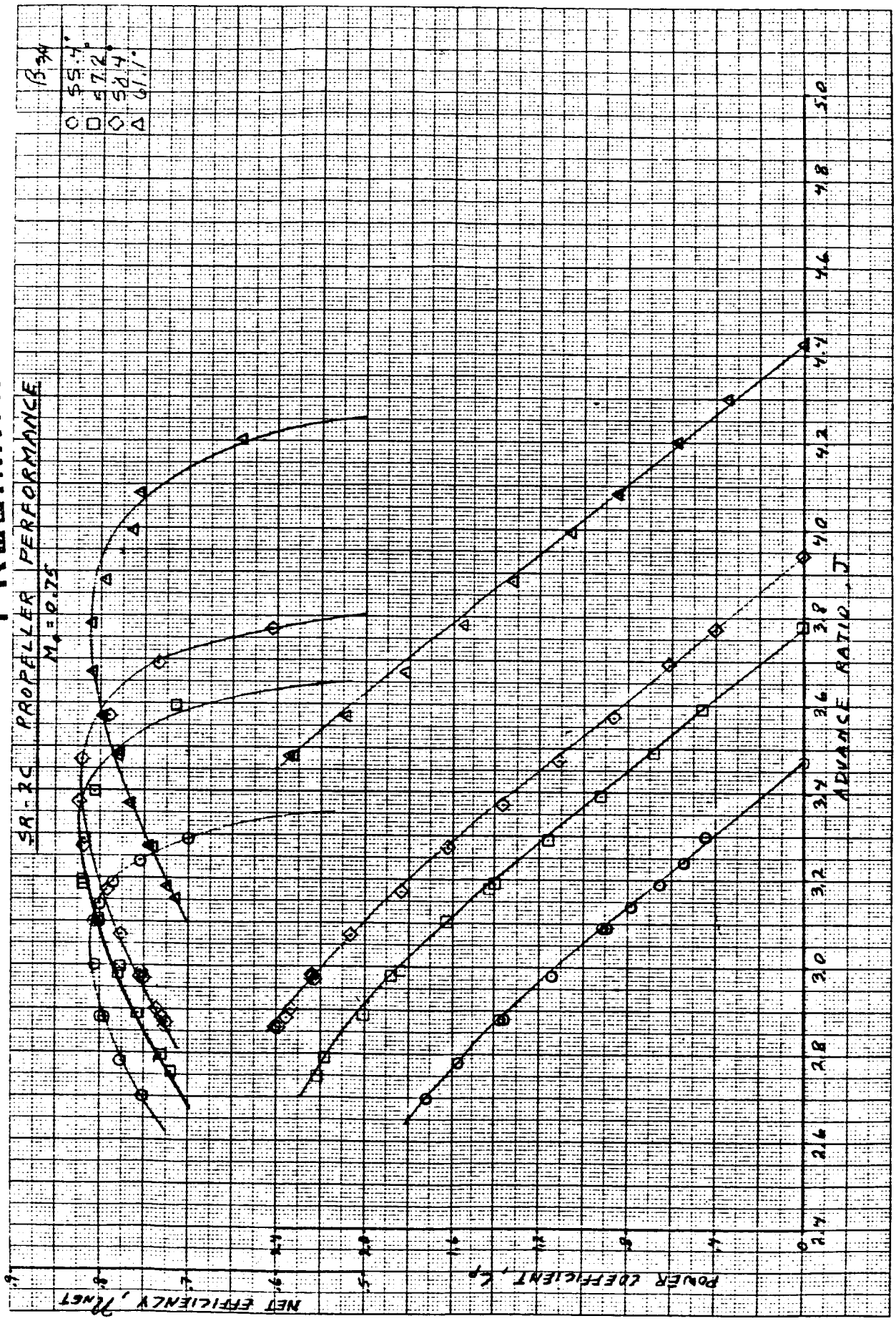

PRELIMINARY DATA

APPENDIX B

PARASITE DRAG SUMMARY

WING MOUNTED PROPFAN NACELLE

PARASITE DRAG SUMMARY:

		DRAG COUNTS
ΔC_{D_1}	due to LEX skin friction	6
ΔC_{D_2}	due to nacelle footprint on wing	-1
ΔC_{D_3}	due to scrubbing drag on wing*	3
ΔC_{D_4}	due to wing footprint on nacelle	-1.2
ΔC_{D_5}	due to scrubbing drag on nacelle	1.1
ΔC_{D_6}	due to nacelle skin friction	7.3

*Did not include scrub drag increment on LEX (rough Calc. showed it to be only 0.1 count)

NOTE: 1 Drag Count = .0001

APPENDIX C

DRAG POLARS

WING MOUNTED PROPFAN NACELLE

PRECEDING PAGE BLANK NOT FILMED

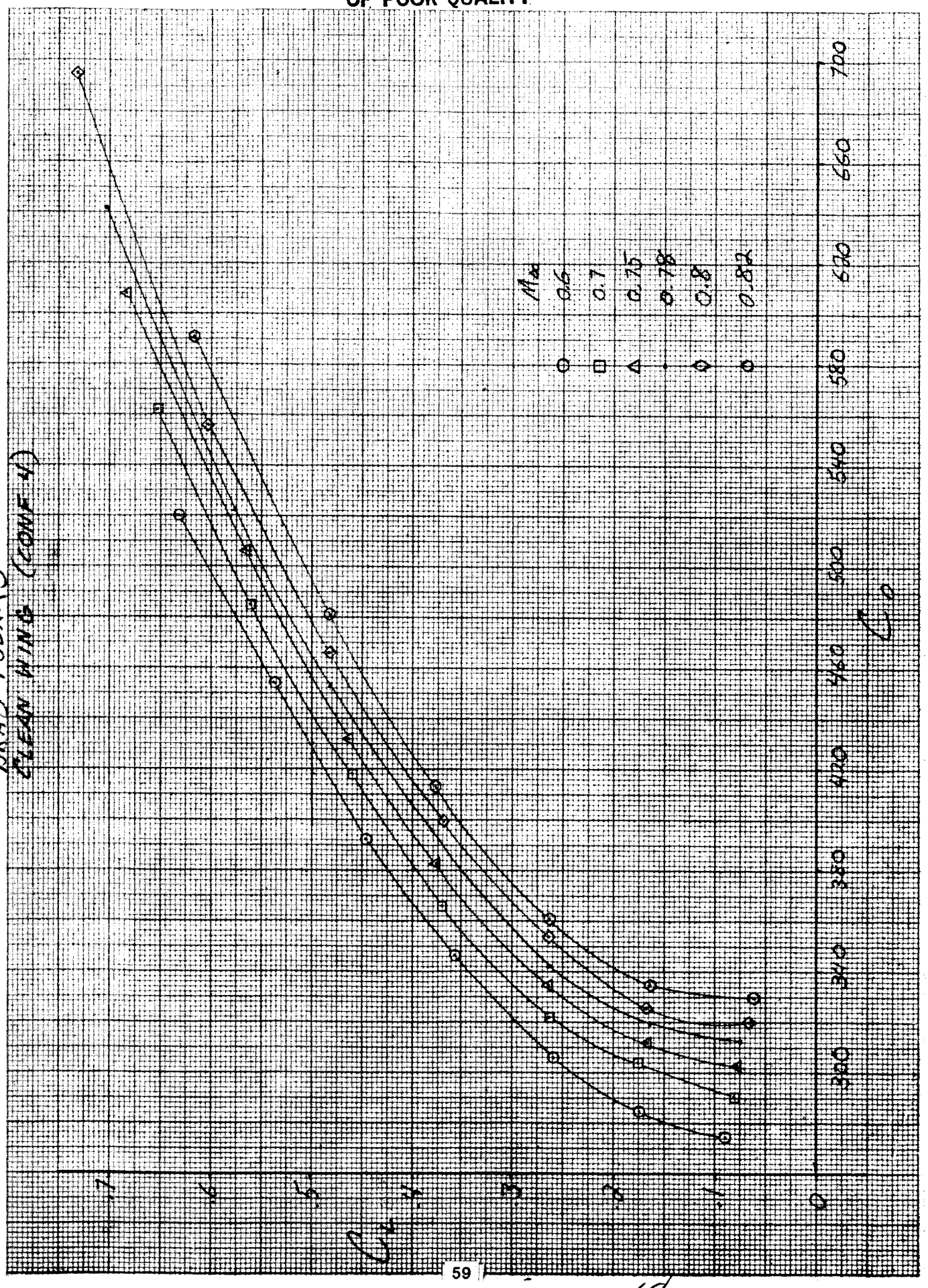

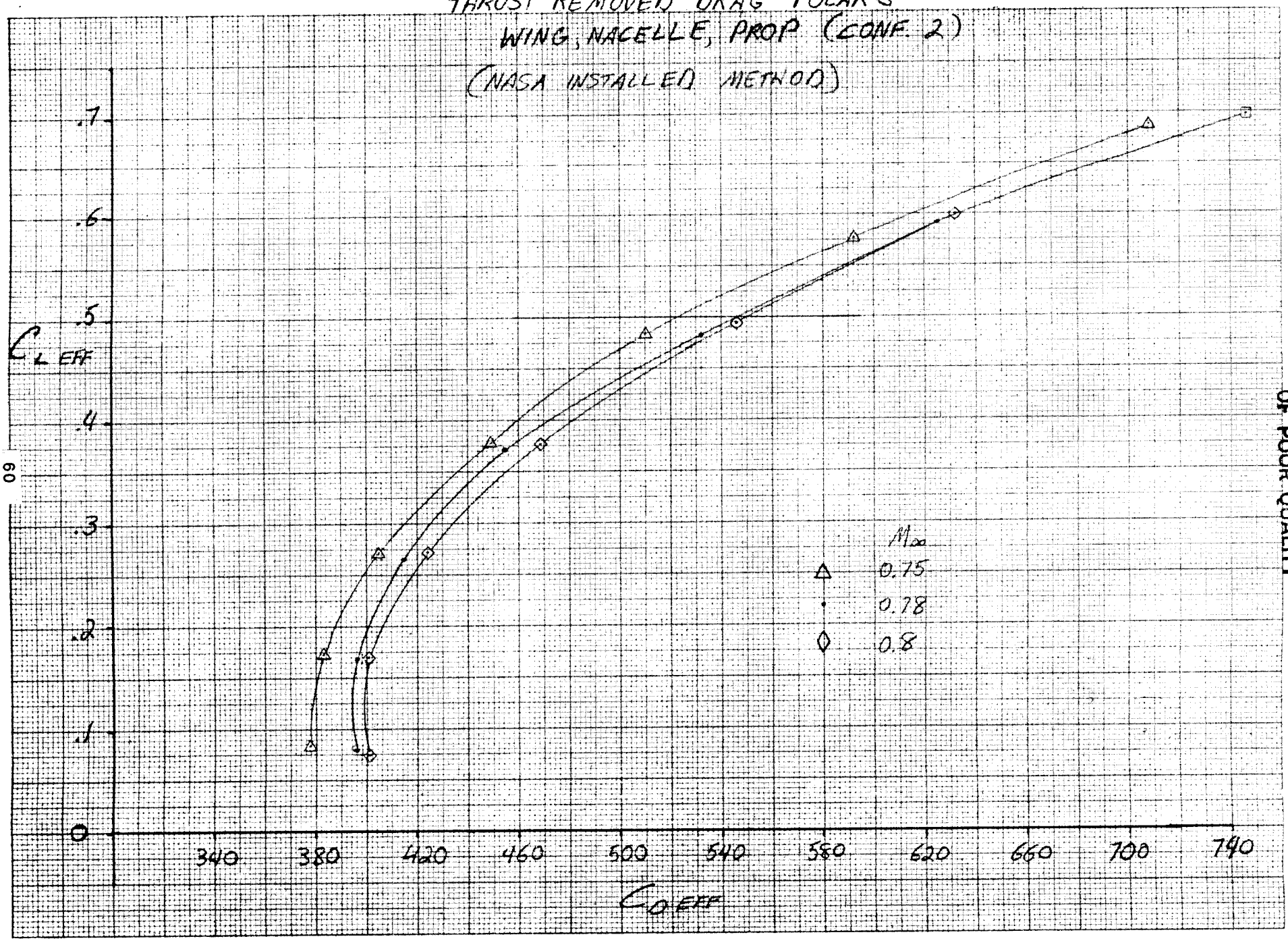

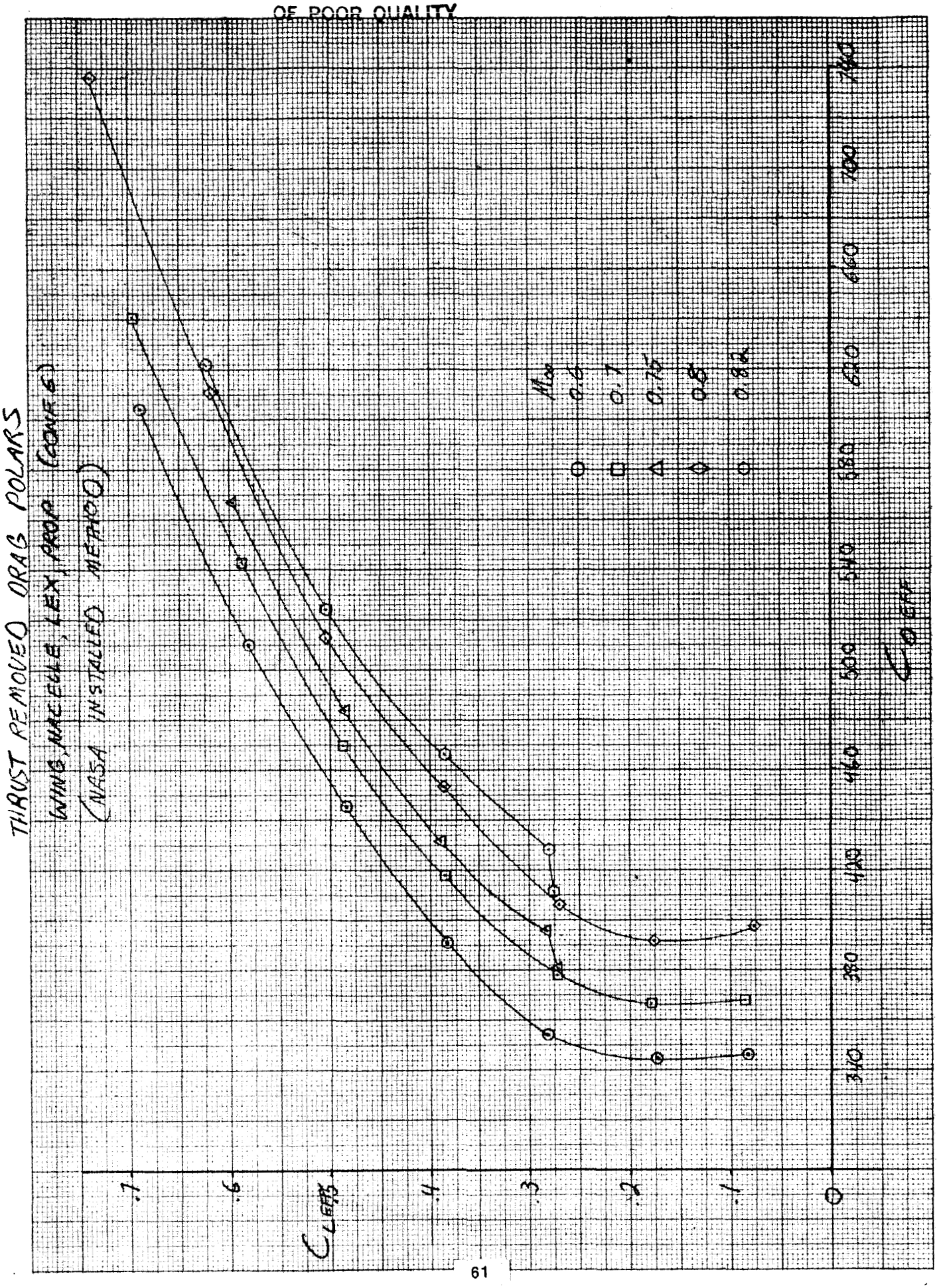

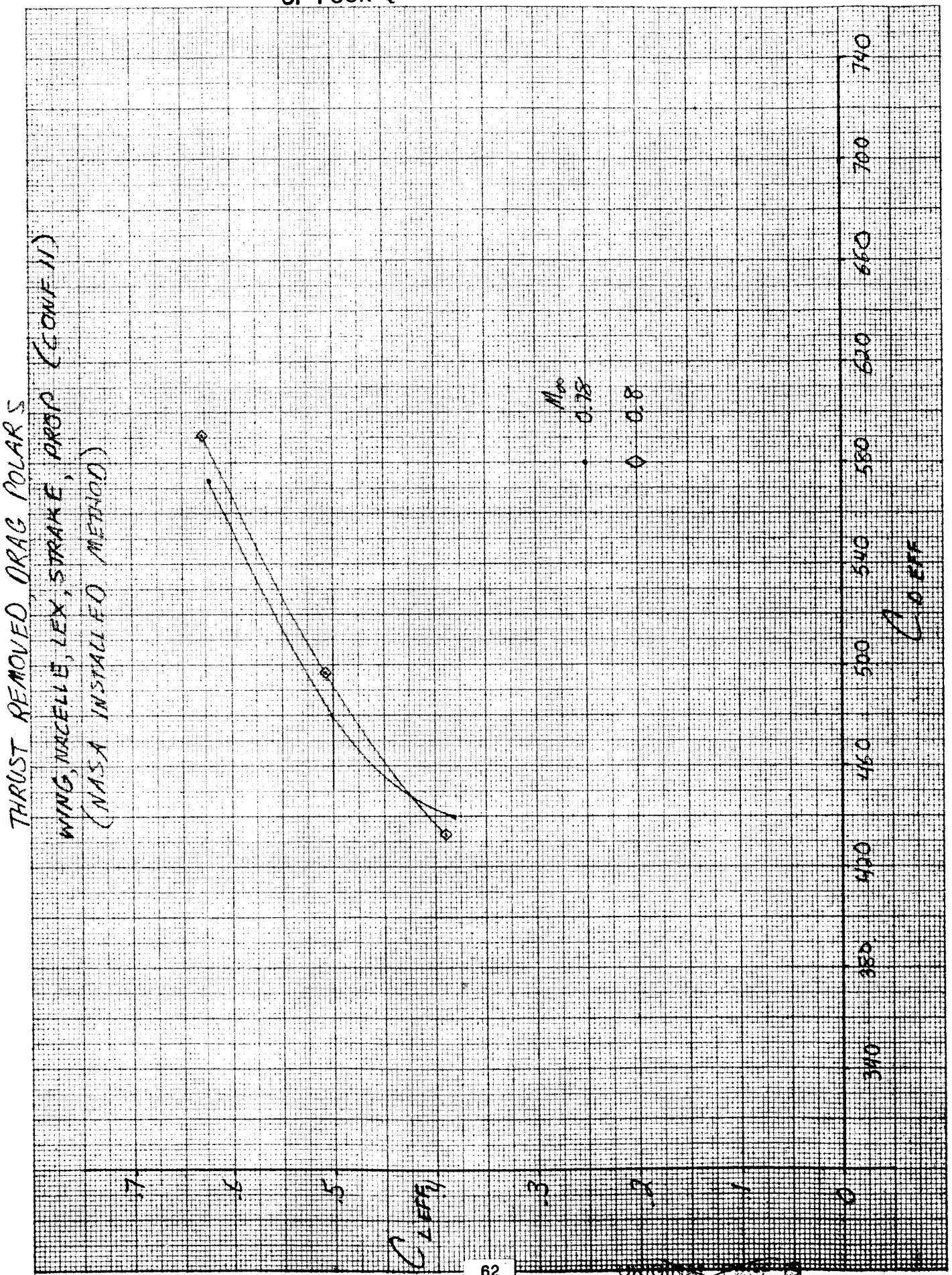

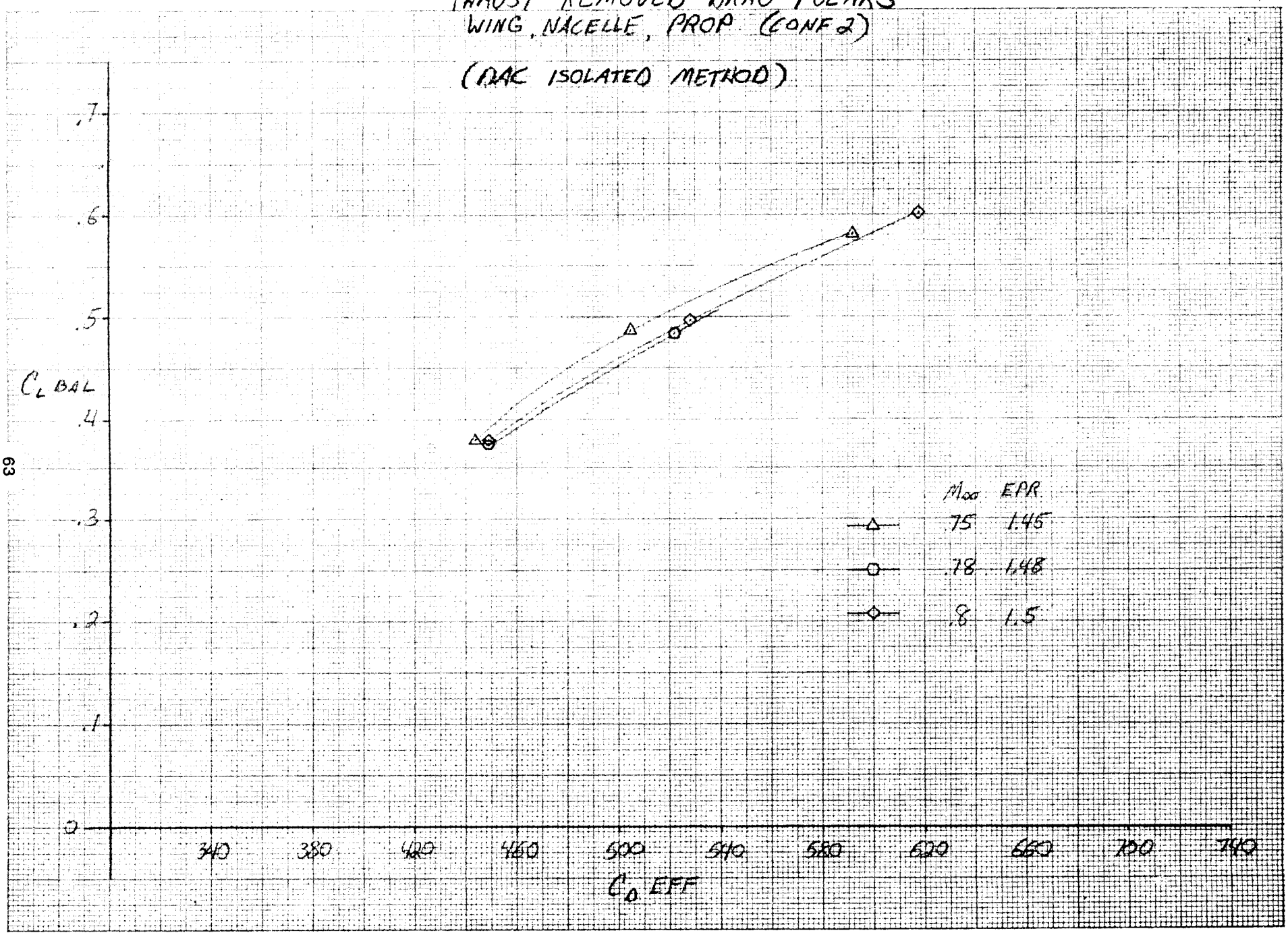

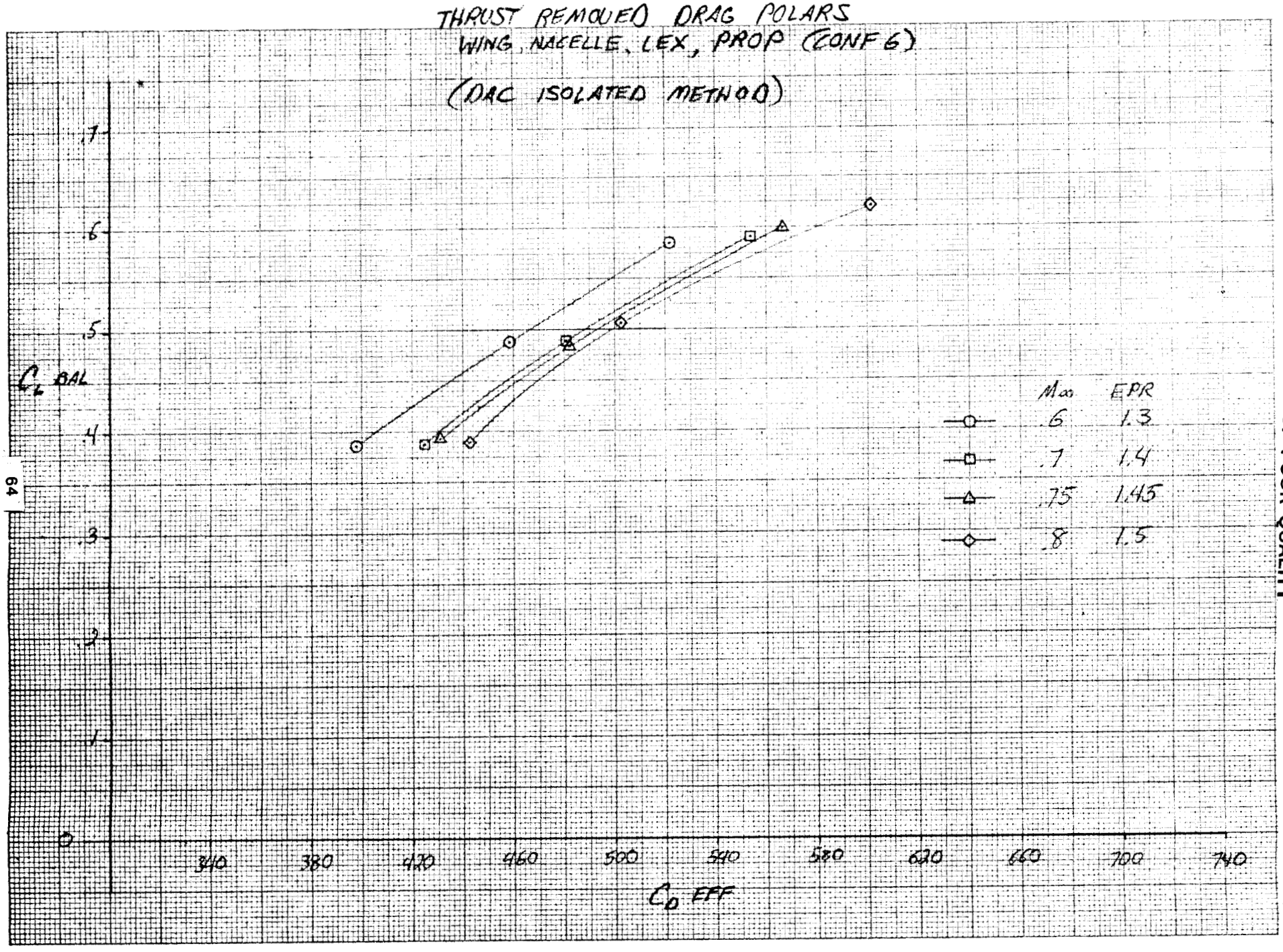

THRUST REMOVED DRAG POLARS
WING, NACELLE, LEX, FILLET, PROP (CONFIG)
(DAC ISOLATED METHOD)

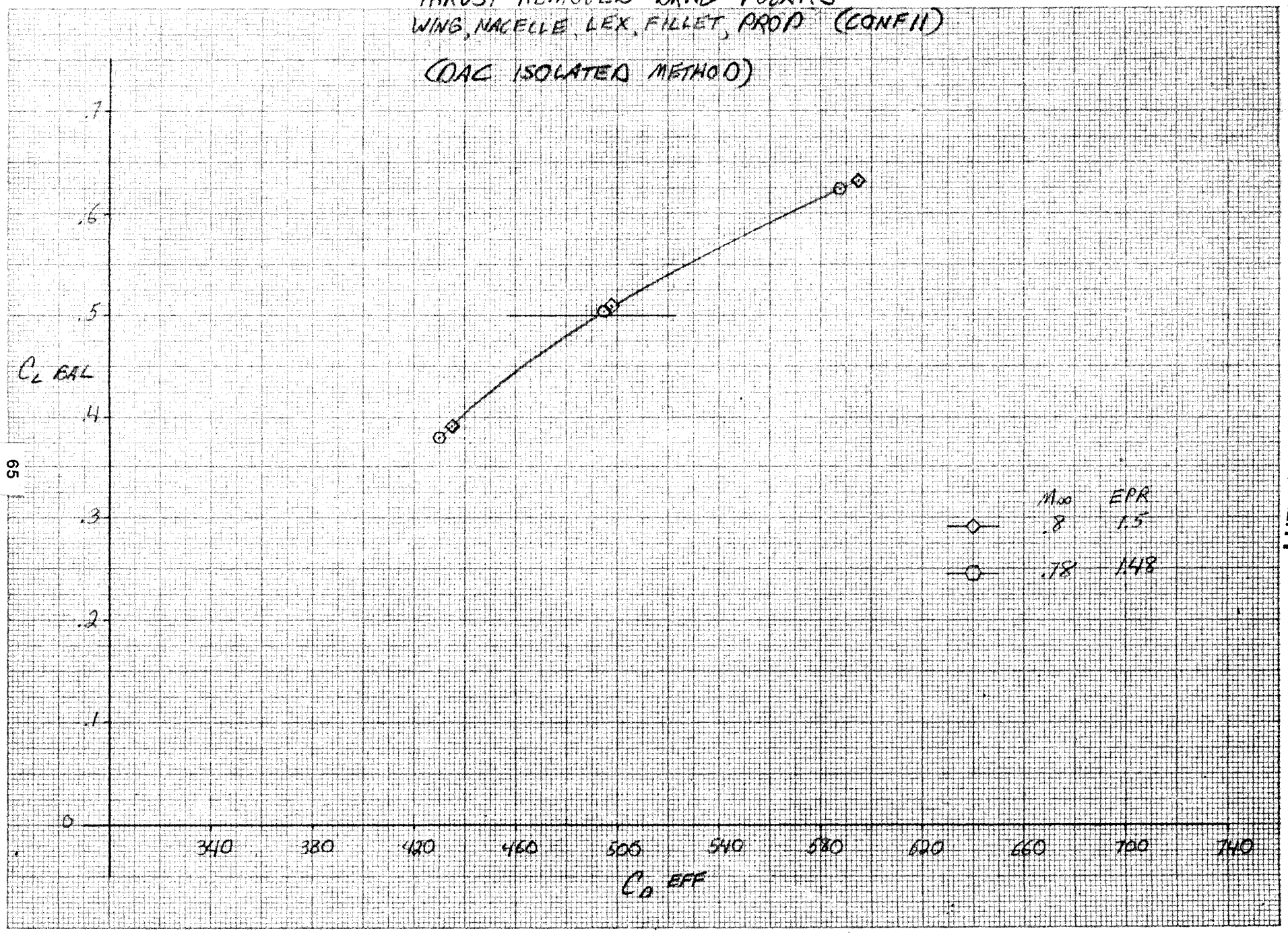

9.0 REFERENCES

(1) (A) H. R. Welge, and J. P. Crowder, "Simulated Propeller Slipstream Effects on a Supercritical Wing." (Douglas Aircraft Company; NASA Contract NAS2-9472.) NASA CR-152138, June 1978.

(2) H. R. Welge, D. H. Neuhart and J. A. Dahlin, "Analysis of Mach Number 0.8 Turboprop Slipstreams Wing/Nacelle Interactions." NASA CR 166214, August 1981.

(3) Turboprop Model Calibration and Proof Tests (TD 1234M), TR80-111.

(4) Smith, R. C. and Levin, A. D.: "Propfan Installation Aerodynamics of a Supercritical Swept Wing Transport Configuration," AIAA Report 81-1563, July 1981.

(5) J. DeYoung, C. W. Harper, "Theoretical Symmetric Span Loading at Subsonic Speeds for Wings Having Arbitrary Plan Form" NACA TR 921, May 1950.

(6) D. P. Mack and S. M. Schimke, "User's Manual For a Fully Automatic Three-Dimensional Potential Flow Calculation Methods." Report MDC J7644/01, August 1977.

(7) P. A. Henne and R. M. Hicks, "Wing Analysis Using a Transonic Potential Flow Computation Method." NASA TM78464, July 1978.

(8) H. R. Welge, "Prop-Fan Integration at Cruise Speeds." AGARD PAPER 33, Douglas Paper 6970, May 1981.

10.0 FIGURES

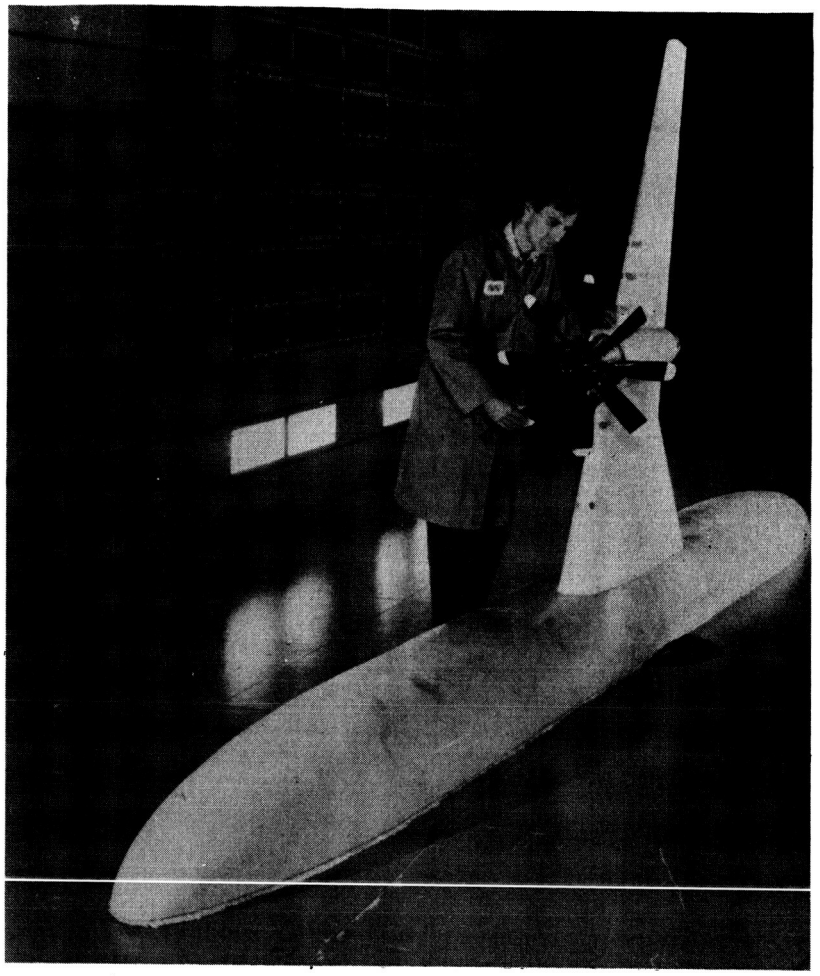

FIGURE 1. STRAIGHT UNDERWING NACELLE MODEL IN AMES TUNNEL

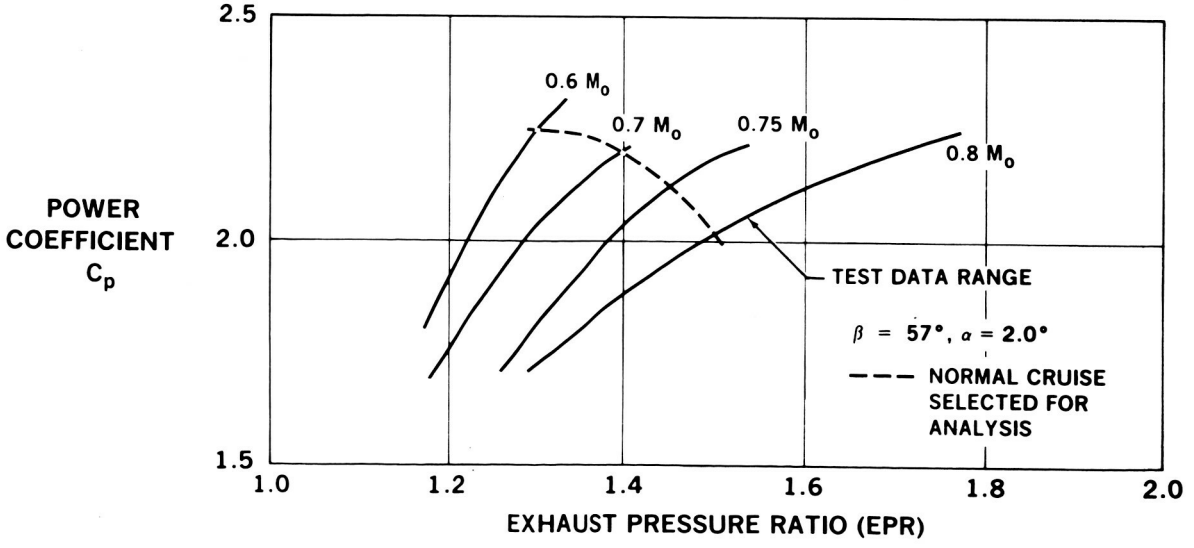

FIGURE 2. TEST CONDITIONS SELECTED FOR ANALYSIS

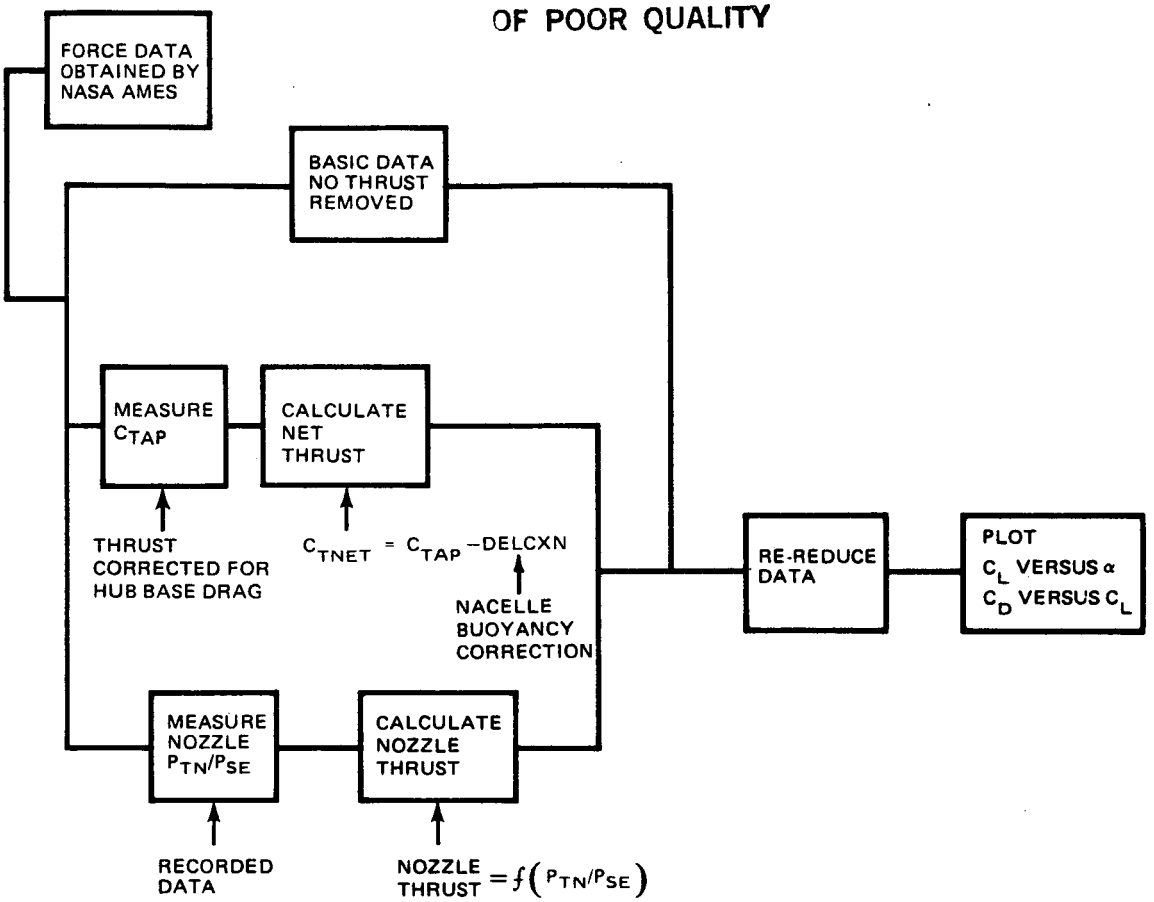

FIGURE 3. INSTALLED PERFORMANCE METHOD

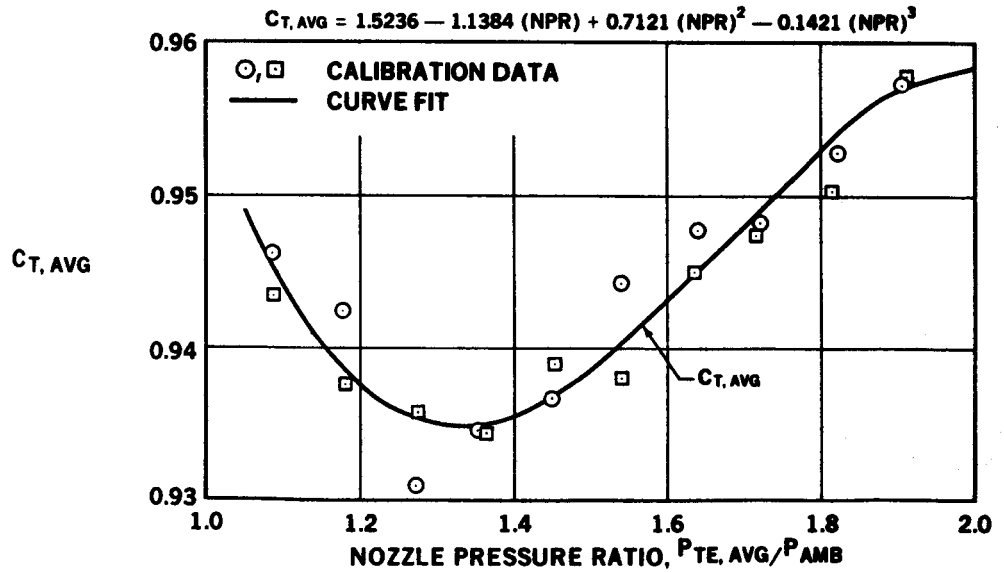

FIGURE 4. EXHAUST DUCT THRUST COEFFICIENT CALIBRATION

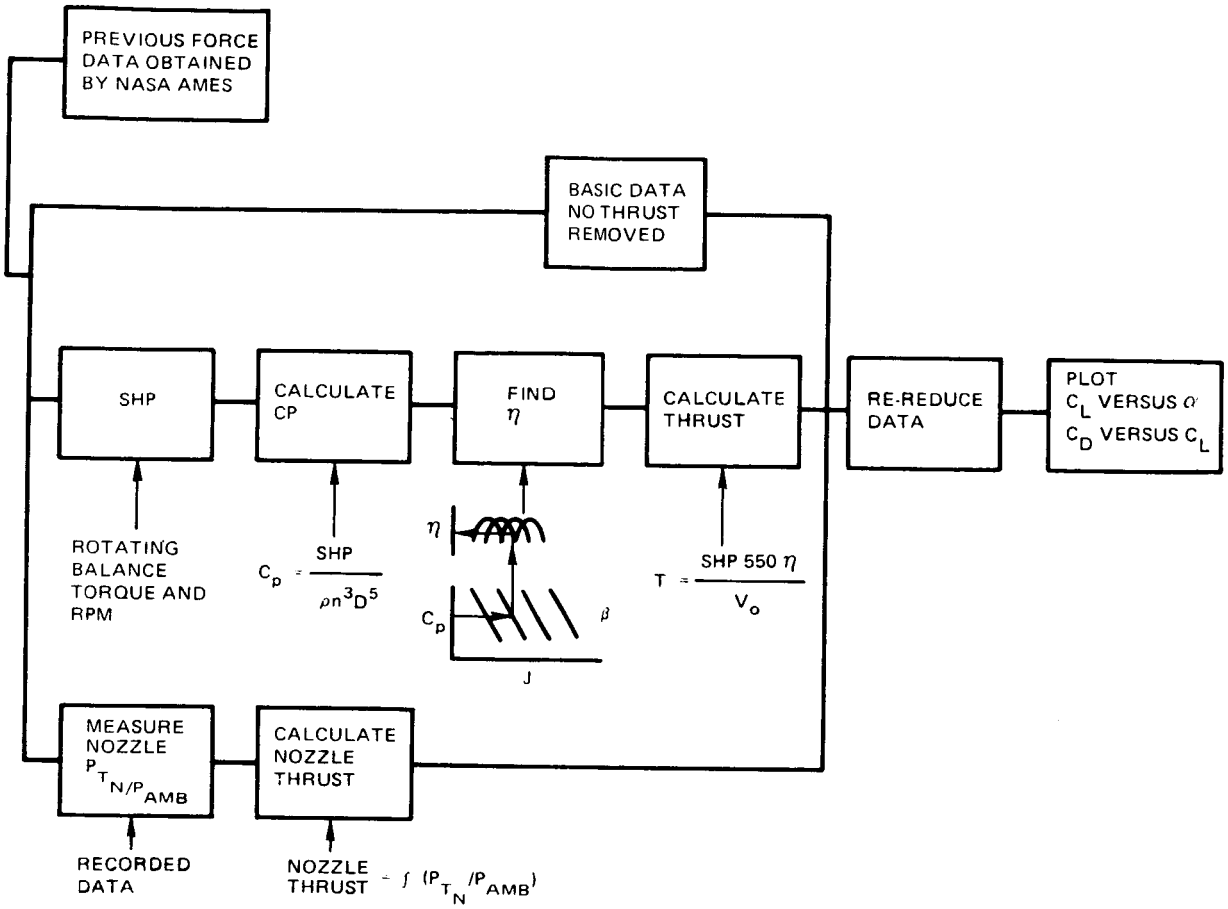

FIGURE 5. DAC ISOLATED PERFORMANCE METHOD

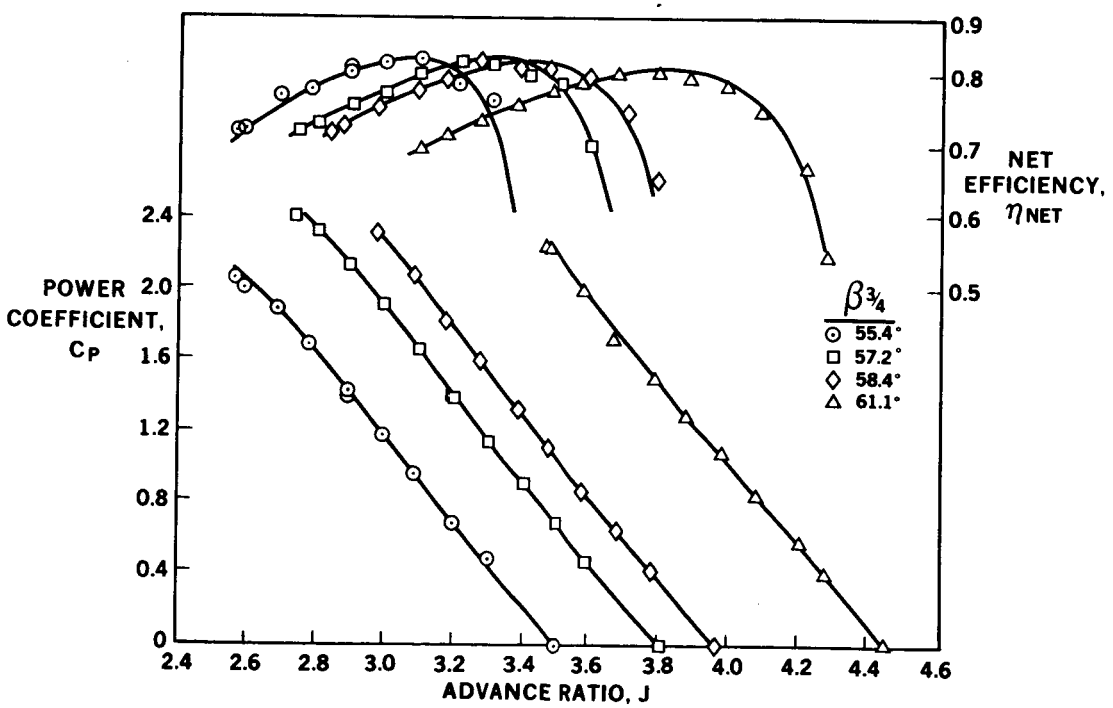

FIGURE 6. SR-2C PROPELLER PERFORMANCE M_o = 0.7

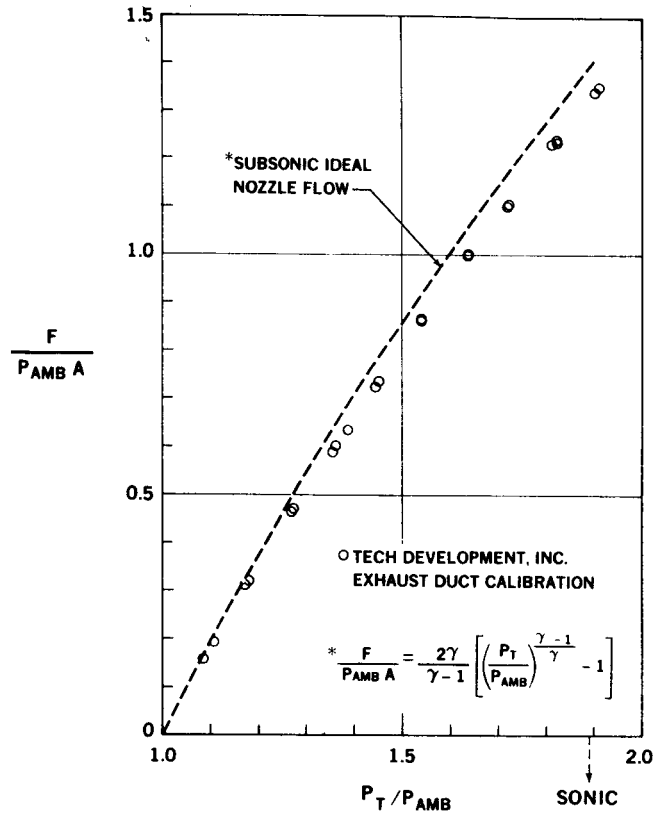

FIGURE 7. ISOLATED EXHAUST NOZZLE CALIBRATION (SUBSONIC IDEAL NOZZLE FLOW)

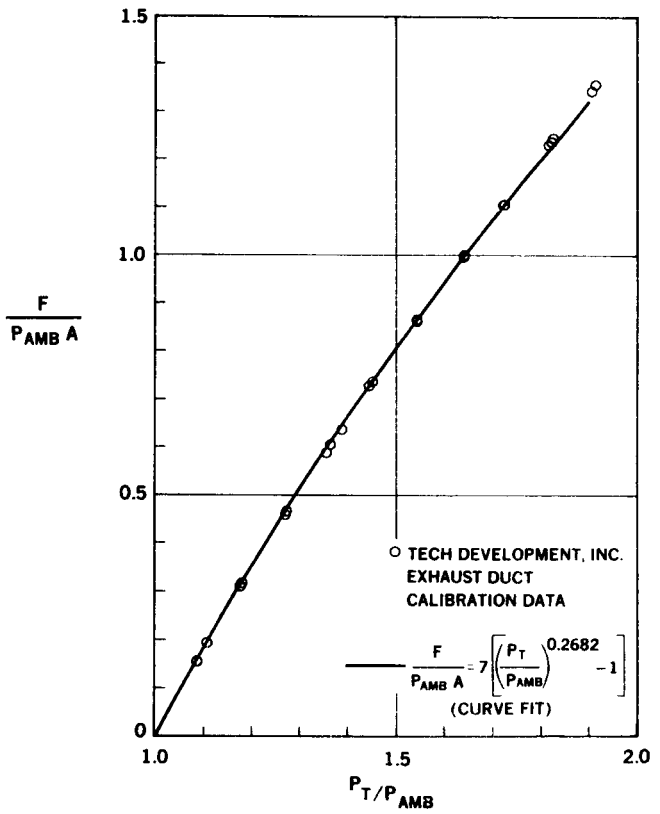

FIGURE 8. ISOLATED EXHAUST NOZZLE CALIBRATION (EXPERIMENTAL DATA CURVE FIT)

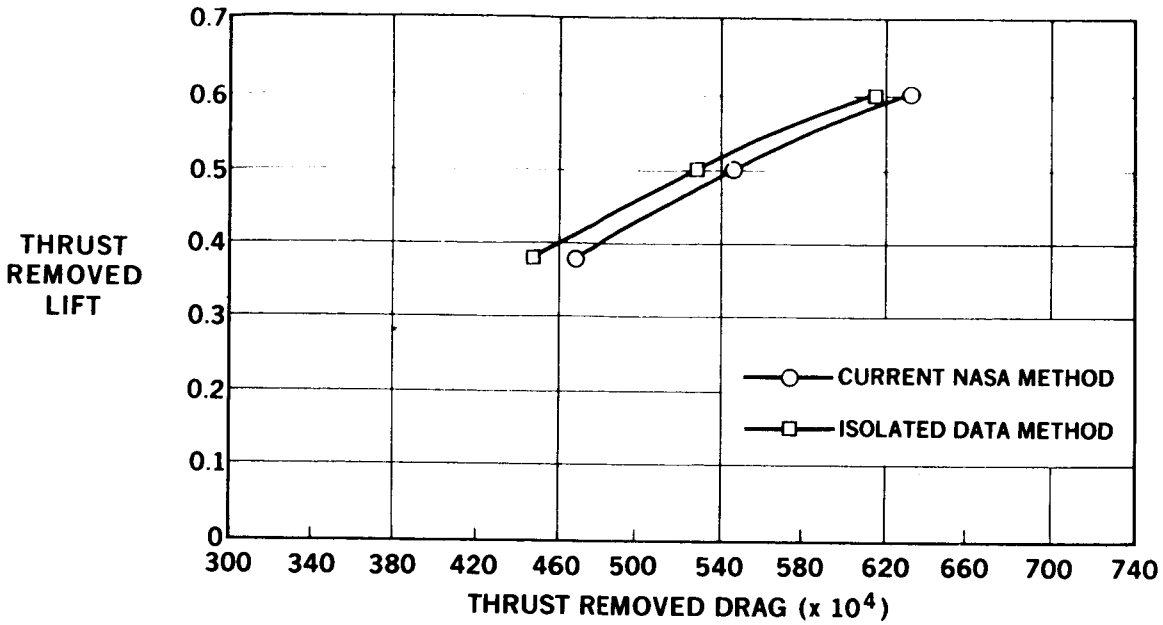

FIGURE 9. THRUST REMOVED DRAG POLAR COMPARISON FOR WING, NACELLE WITH POWER, M_o = 0.8

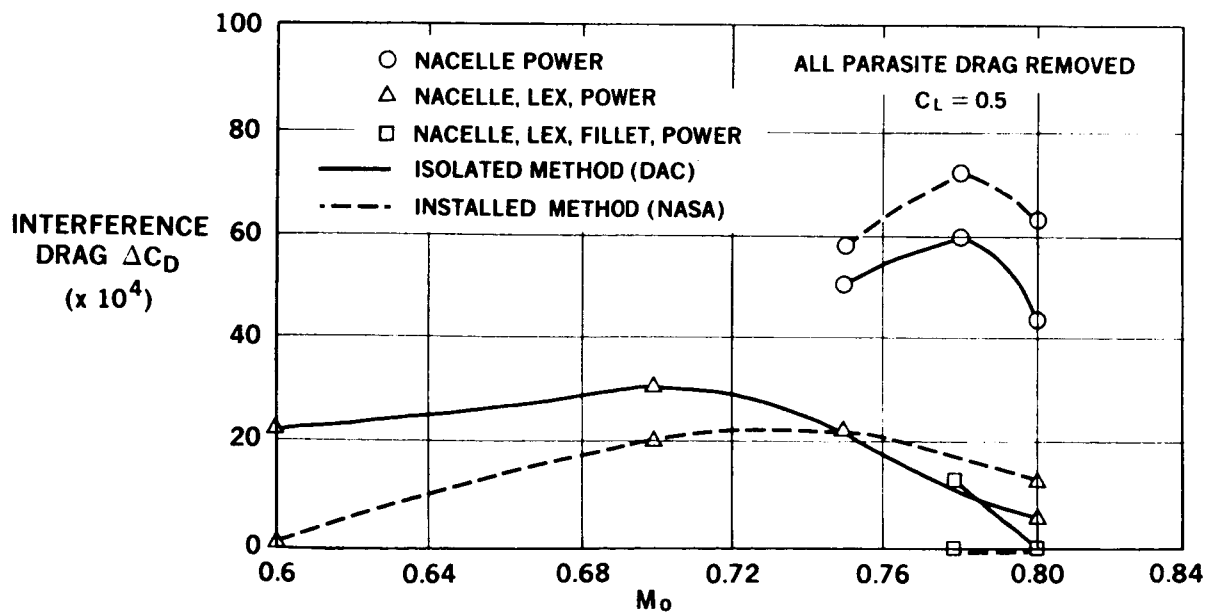

FIGURE 10. THRUST/DRAG BOOKEEPING COMPARISON, INTERFERENCE DRAG LEVELS

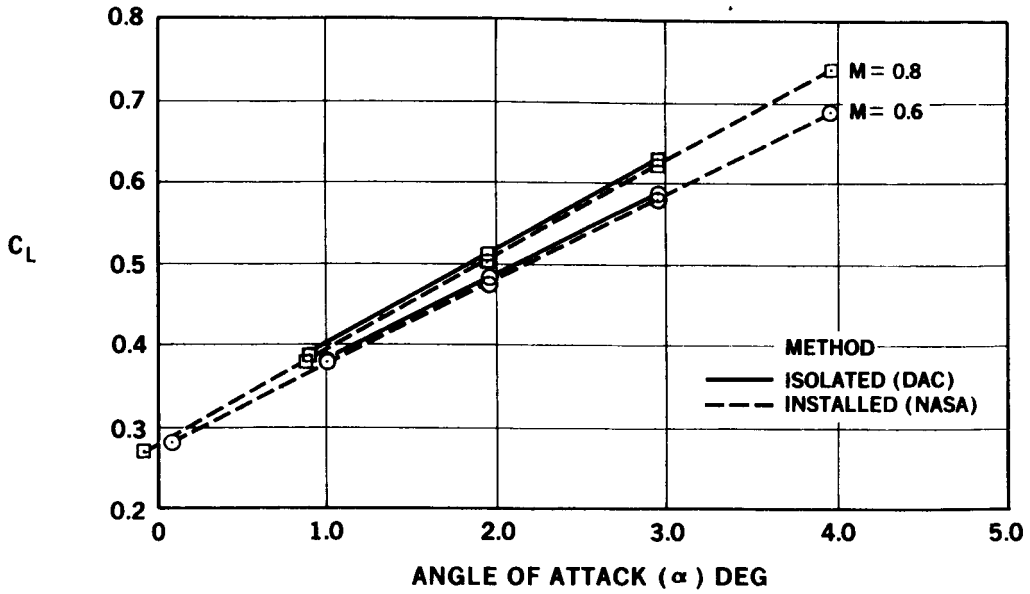

FIGURE 11. THRUST REMOVED LIFT CURVE COMPARISON FOR WING, NACELLE, LEX, PROP

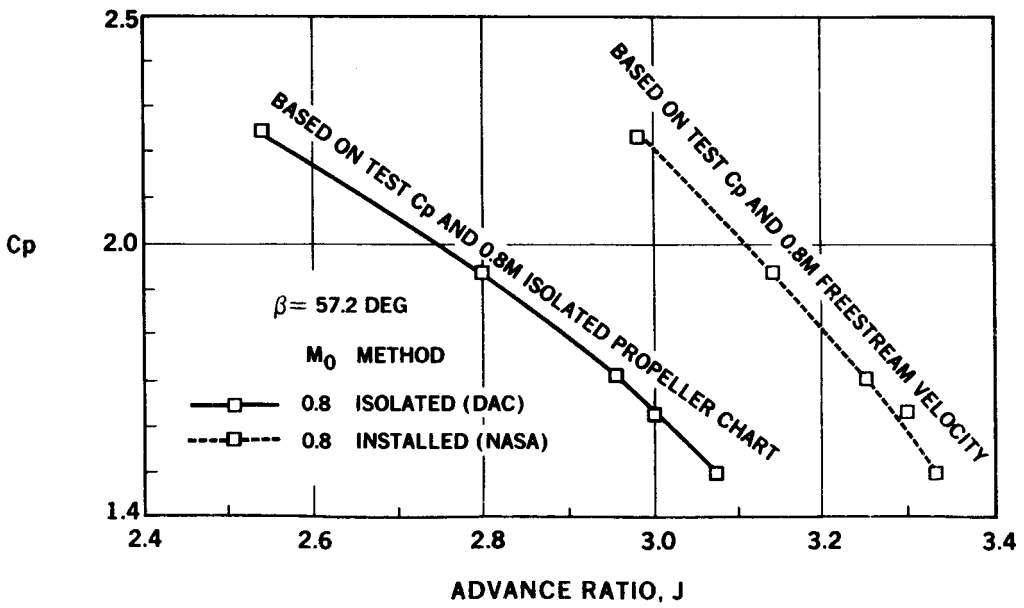

FIGURE 12. POWER COEFFICIENT VERSUS ADVANCED RATIO

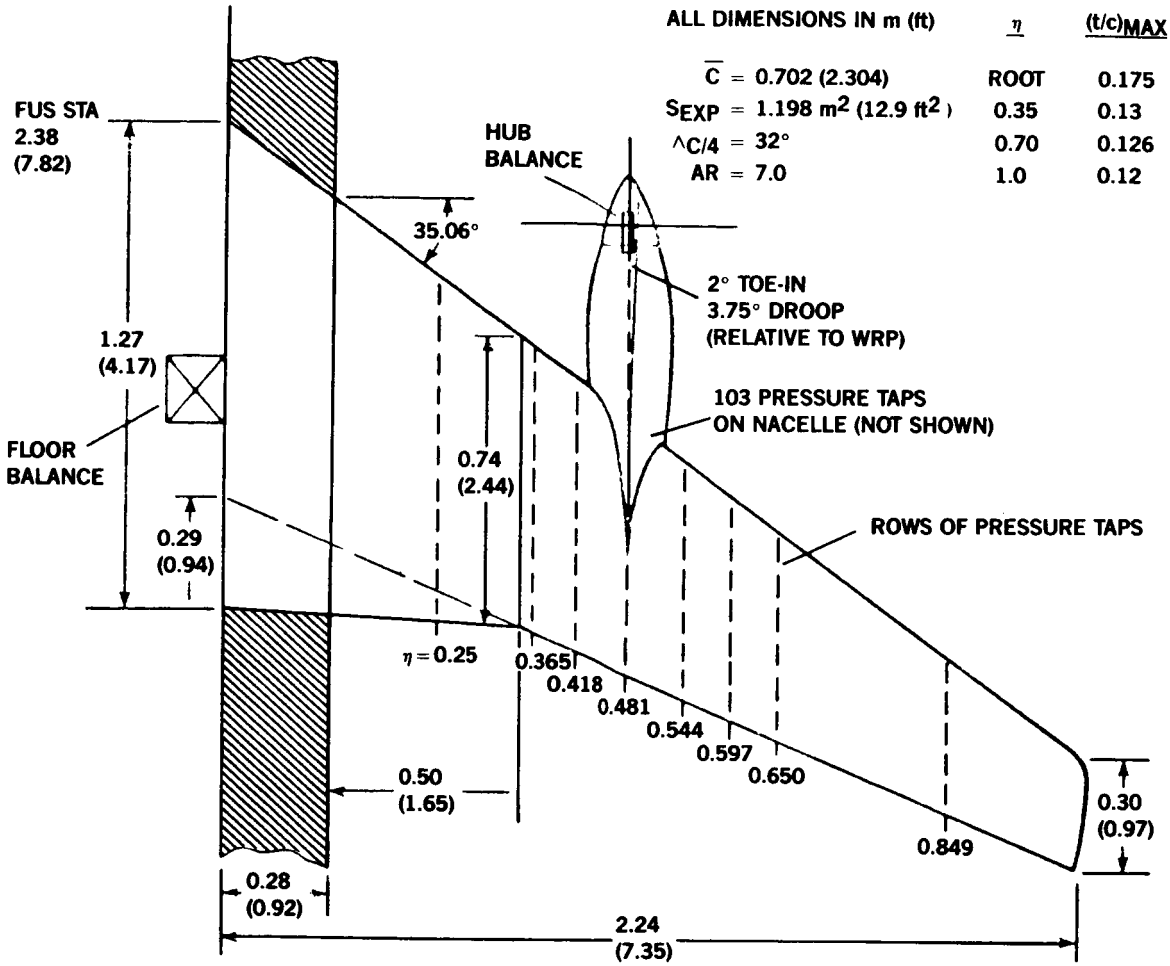

FIGURE 13. WING GEOMETRY AND INSTRUMENTATION (TOP VIEW)

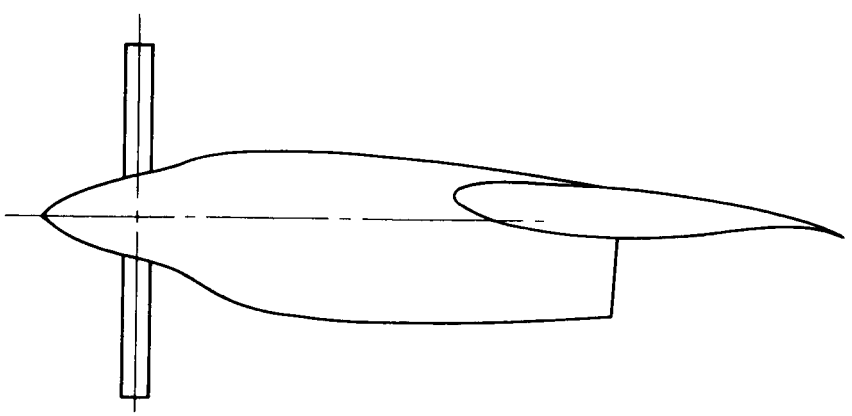

FIGURE 14. SIDE VIEW OF UNDERWING NACELLE

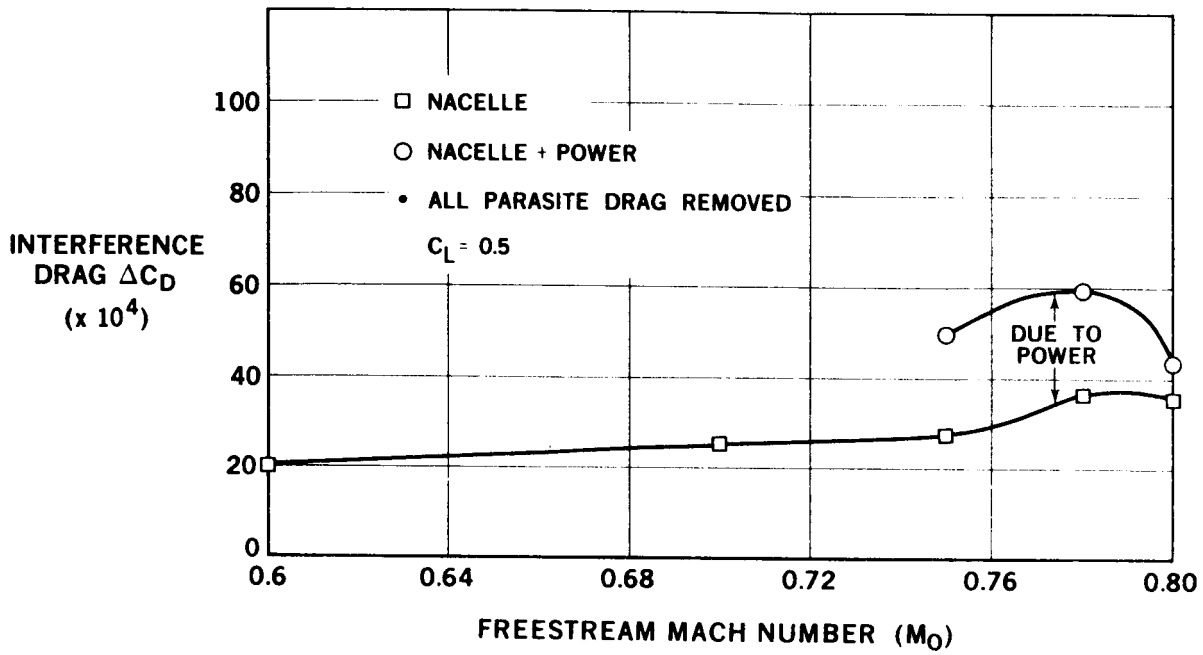

FIGURE 15. INTERFERENCE DRAG LEVELS FOR STRAIGHT UNDERWING NACELLE

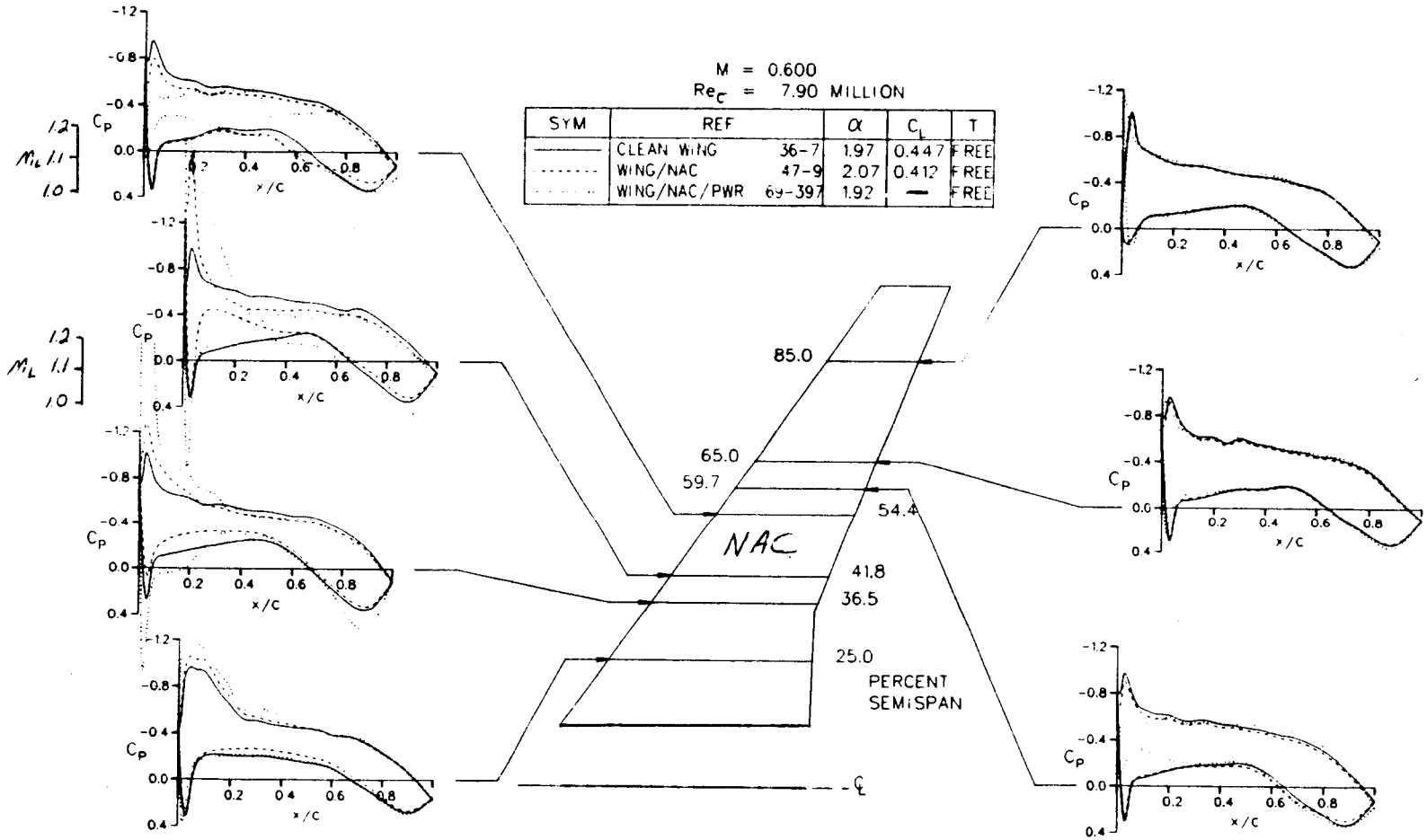

FIGURE 16. EXPERIMENTAL CHORDWISE PRESSURE DISTRIBUTIONS FOR STRAIGHT UNDERWING NACELLE, $0.6M_o$, α = 2 DEGREES

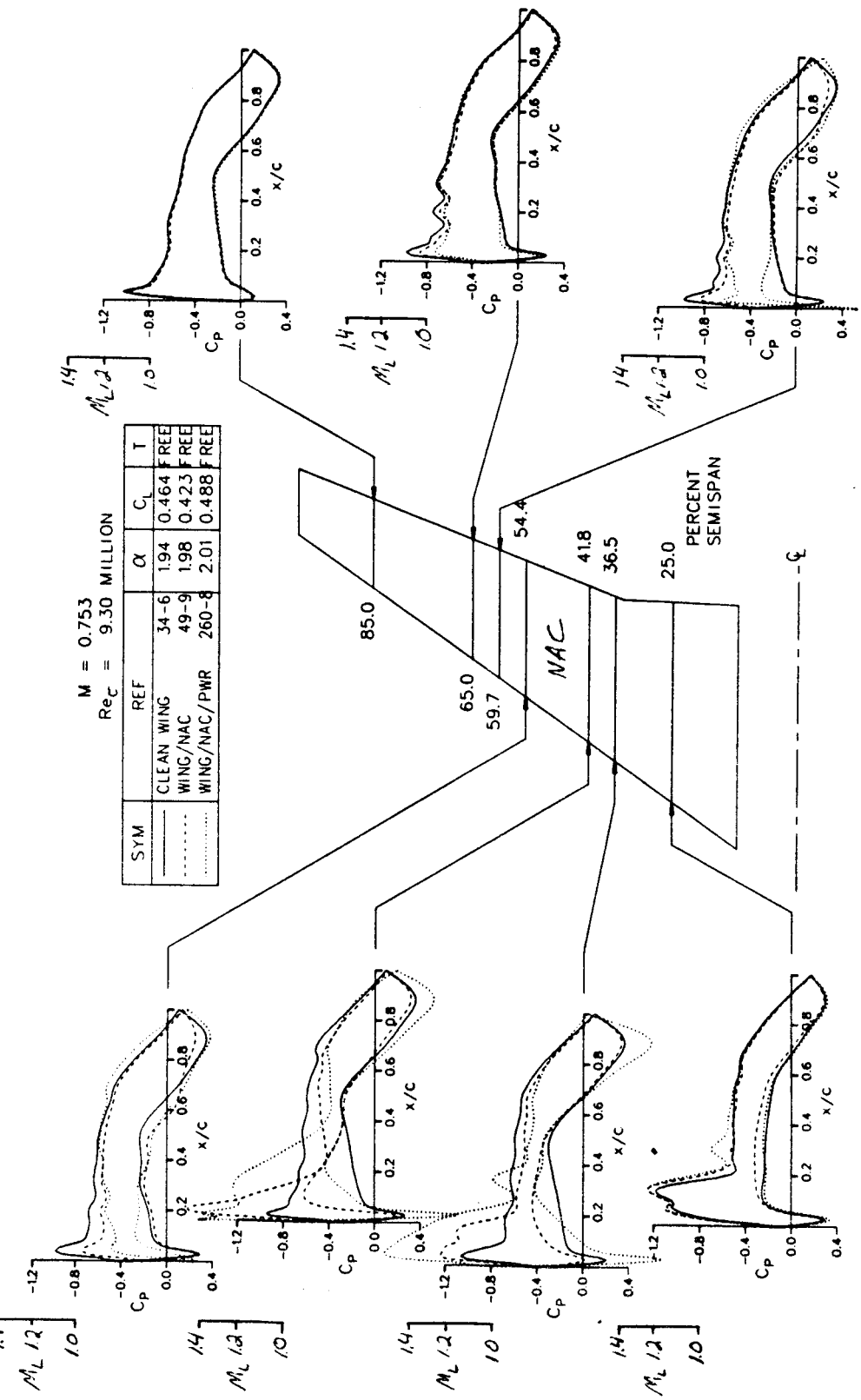

FIGURE 17. EXPERIMENTAL CHORDWISE PRESSURE DISTRIBUTIONS FOR STRAIGHT UNDERWING NACELLE, $0.75M_{\sigma}$, α = 2 DEGREES

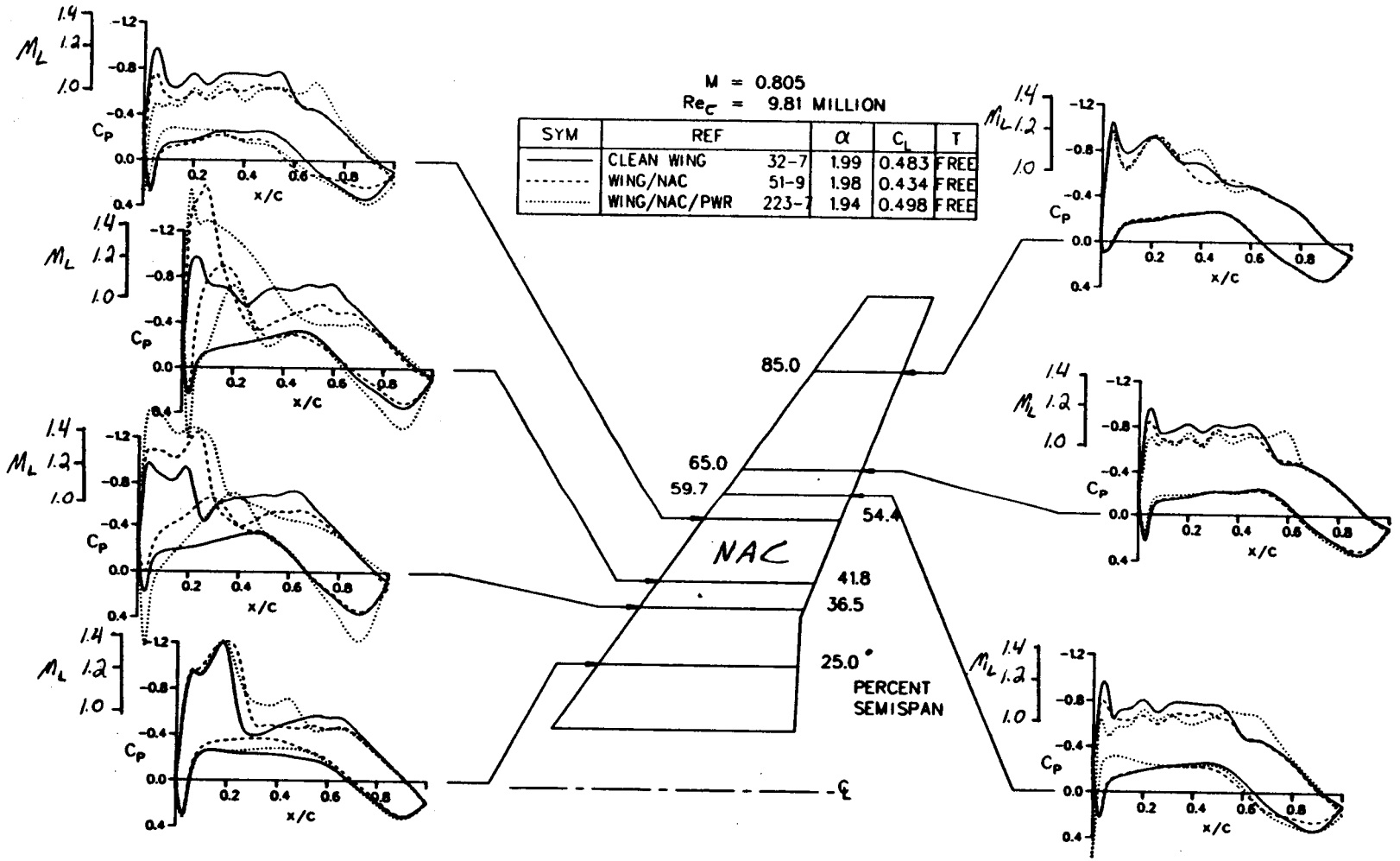

FIGURE 18. EXPERIMENTAL CHORDWISE PRESSURE DISTRIBUTIONS FOR STRAIGHT UNDERWING NACELLE, 0.8M$_O$, α = 2 DEGREES

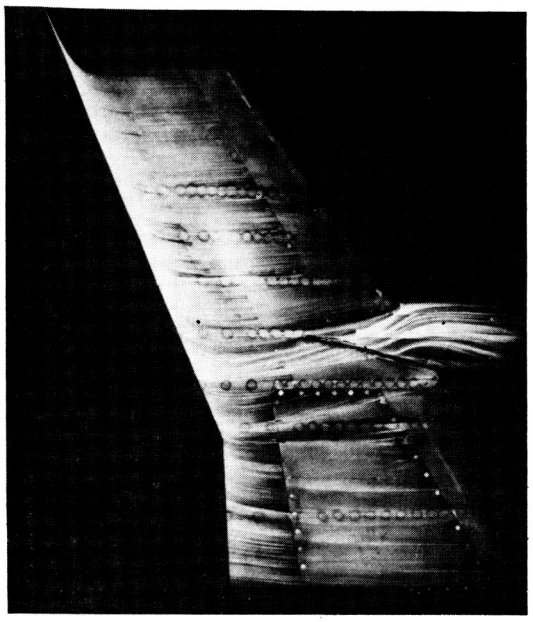

M_o = 0.75
α = 2 DEG
WINDMILL
UPPER SURFACE

FIGURE 19. OIL FLOW PHOTOGRAPH FOR STRAIGHT UNDERWING NACELLE AT M_o = 0.75 – WINDMILL CONDITIONS

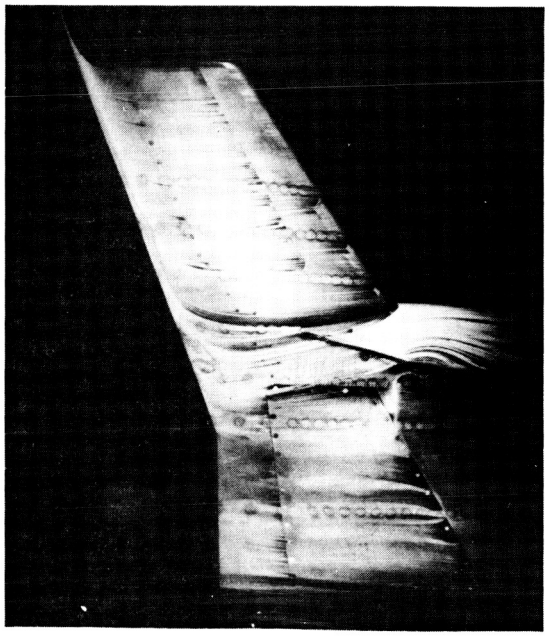

M_o = 0.8
α = 2 DEG
WINDMILL
UPPER SURFACE

FIGURE 20. OIL FLOW PHOTOGRAPH FOR STRAIGHT UNDERWING NACELLE AT M_o = 0.8 – WINDMILL CONDITIONS

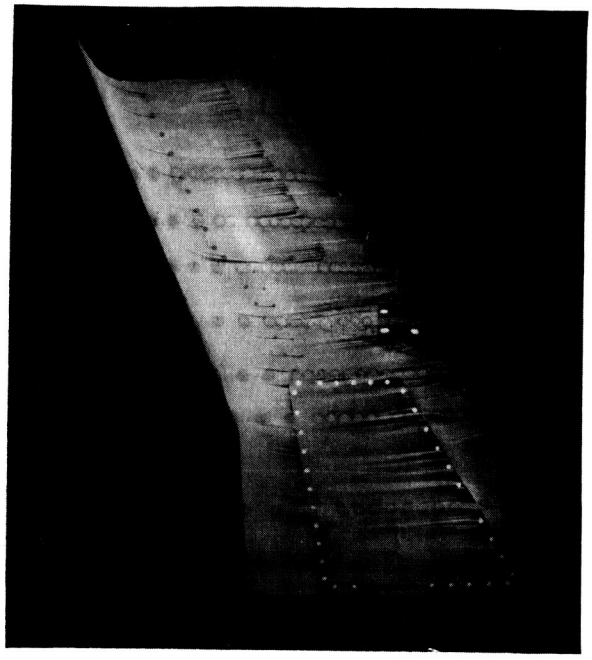

M_o = 0.8
α = 2 DEG

FIGURE 21. OIL FLOW PHOTOGRAPH FOR CLEAN WING W4 AT M_o = 0.8

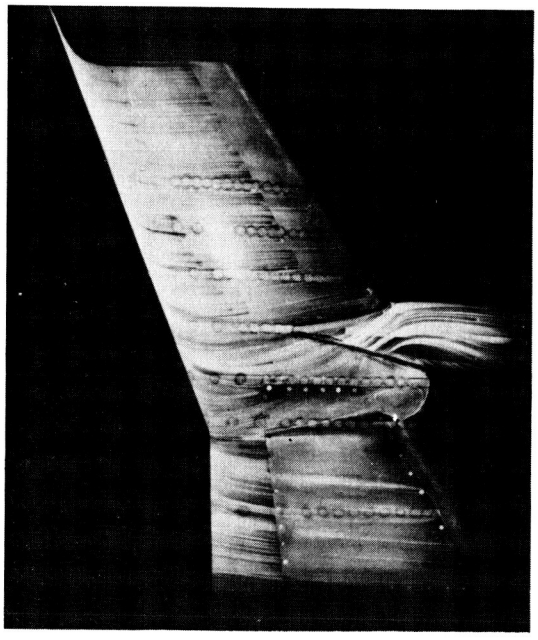

M_o = 0.75
α = 2 DEG
8,100 RPM
UPPER SURFACE

FIGURE 22. OIL FLOW PHOTOGRAPH FOR STRAIGHT UNDERWING NACELLE AT M_o = 0.75 – WITH POWER

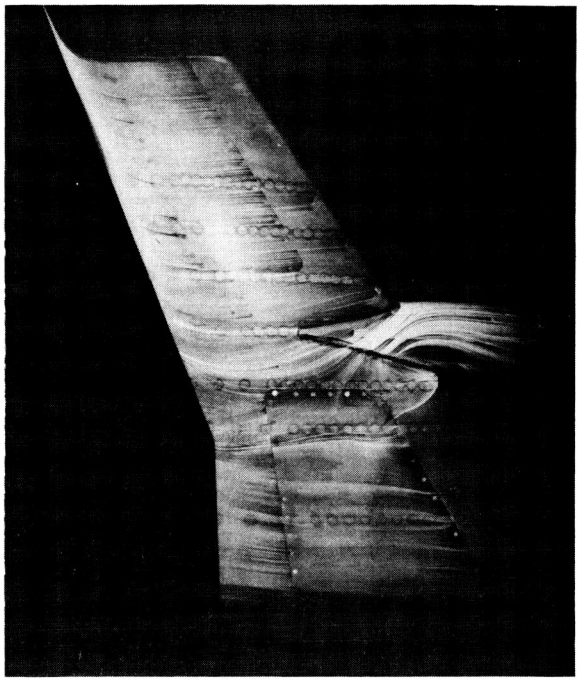

FIGURE 23. OIL FLOW PHOTOGRAPH AT M_o = 0.8 – MAXIMUM POWER

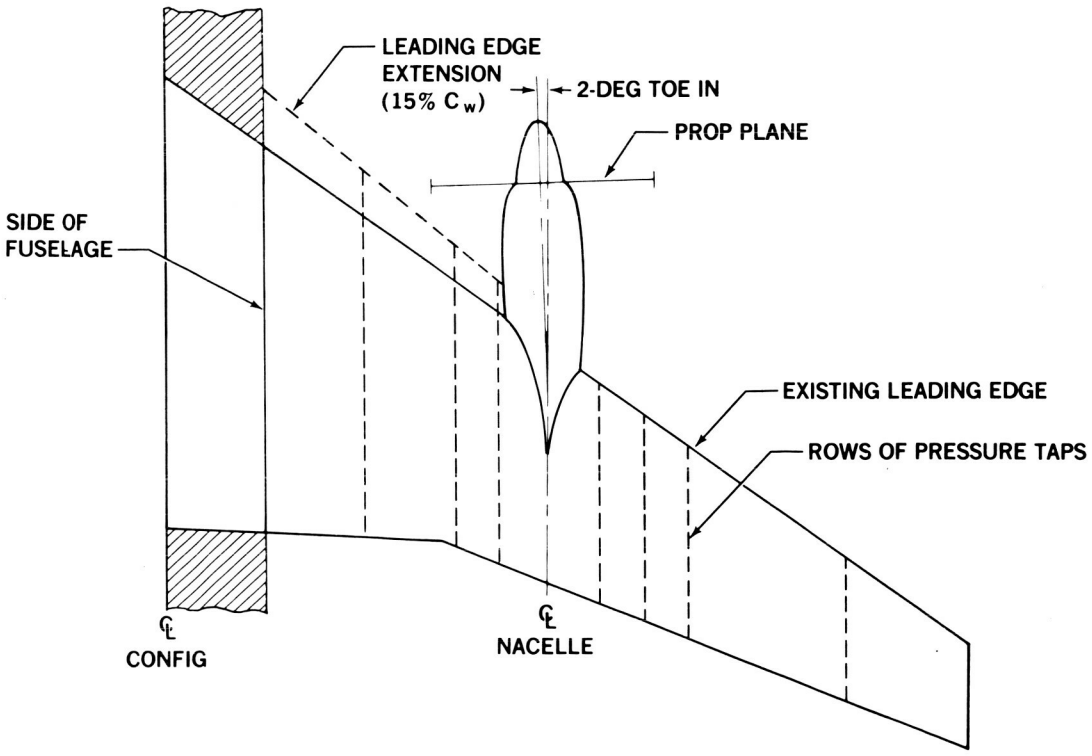

FIGURE 24. PLAN VIEW OF STRAIGHT UNDERWING NACELLE WITH LEX

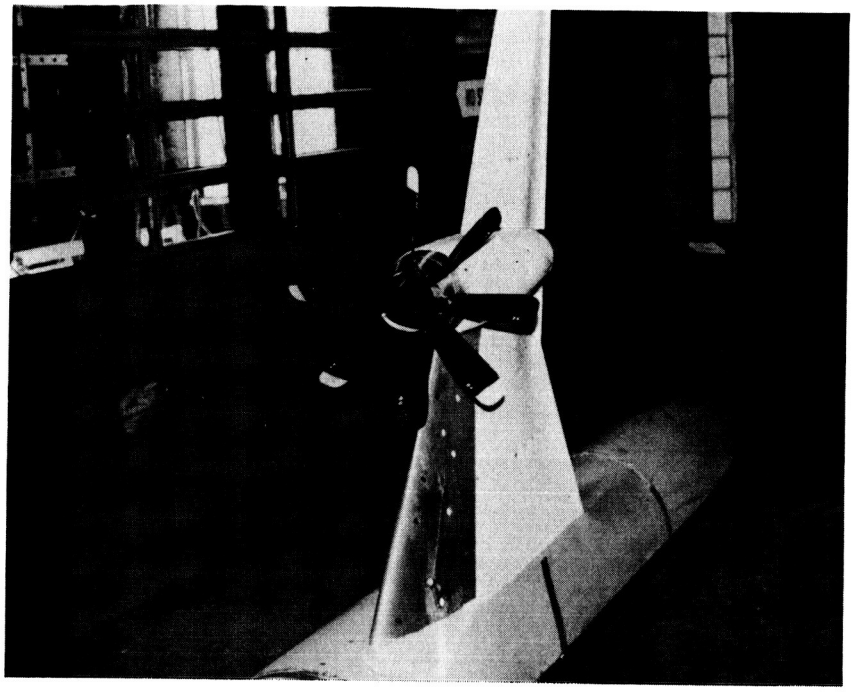

FIGURE 25. STRAIGHT UNDERWING NACELLE WITH LEX MODEL INSTALLED IN AMES 11-FOOT TUNNEL

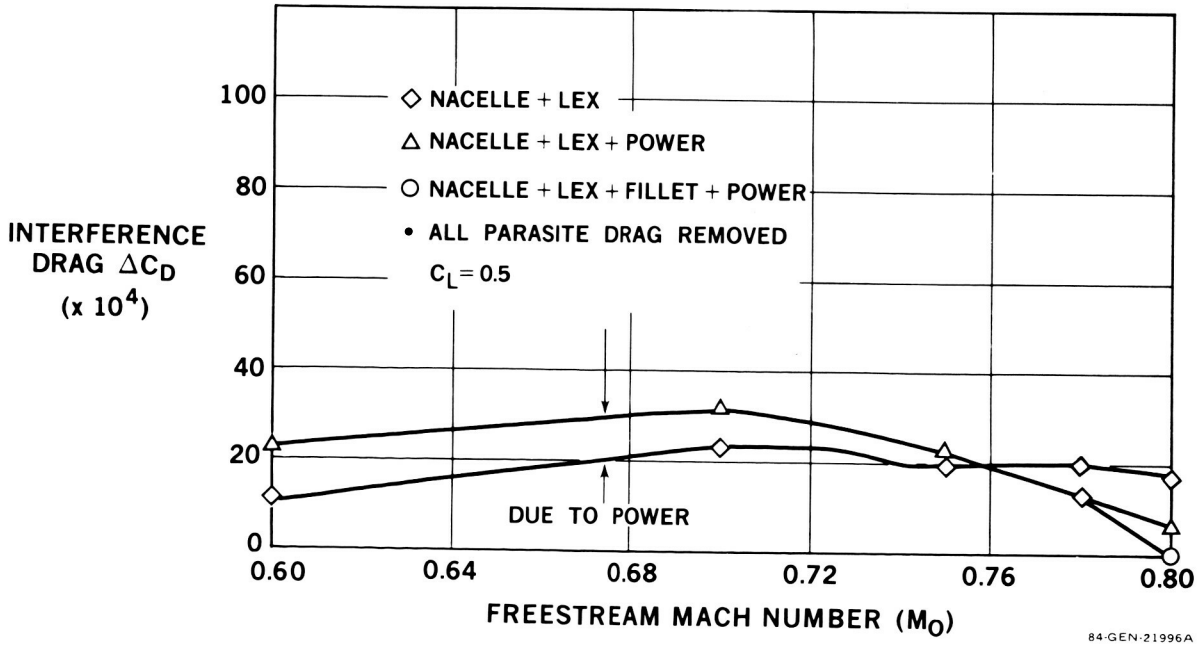

FIGURE 26. INTERFERENCE DRAG LEVELS FOR STRAIGHT UNDERWING NACELLE WITH LEX

ORIGINAL PAGE IS
OF POOR QUALITY

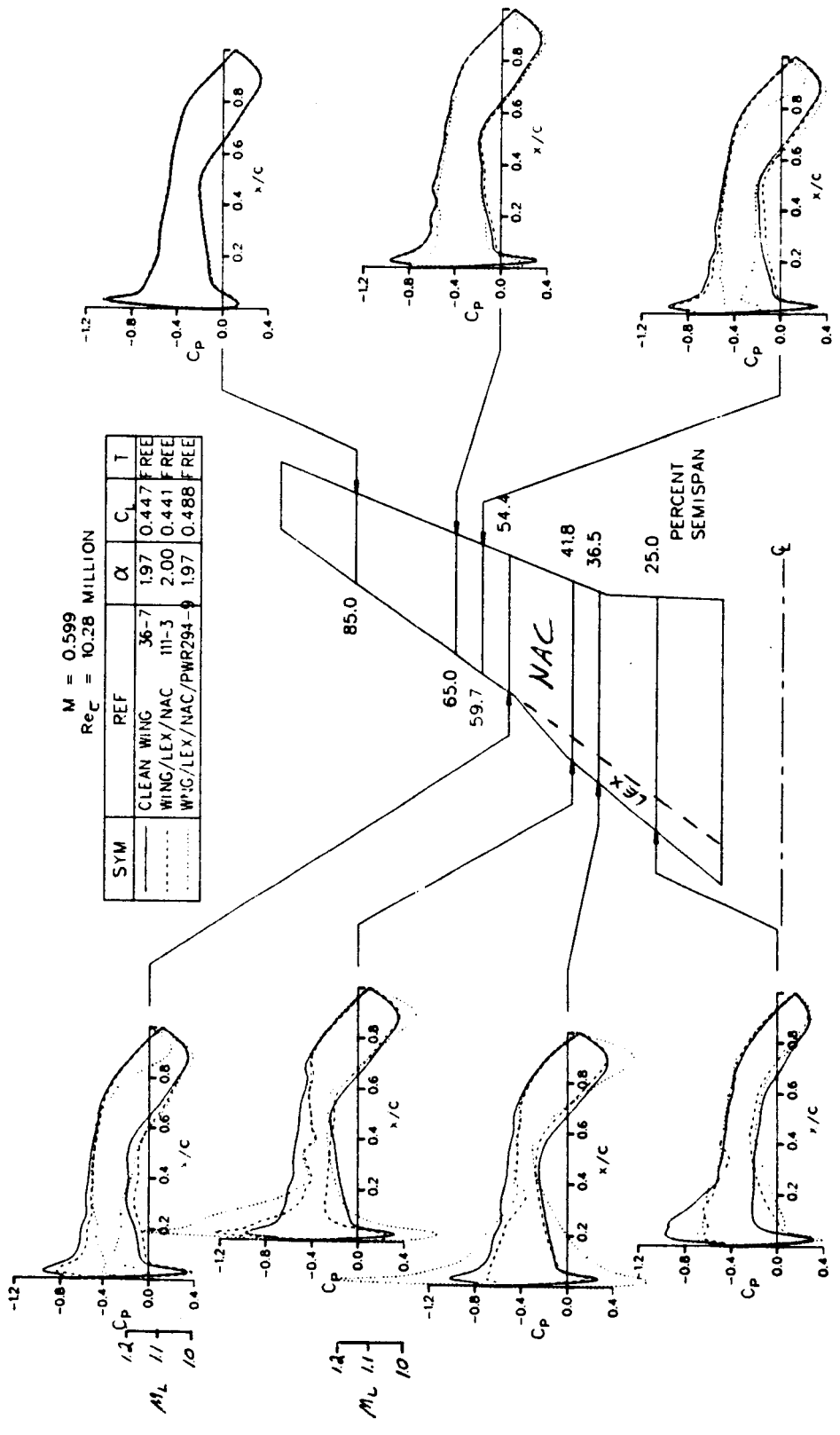

FIGURE 27. EXPERIMENTAL CHORDWISE PRESSURE DISTRIBUTIONS FOR STRAIGHT UNDERWING NACELLE WITH LEX, $0.6M_o$, α = 2 DEGREES

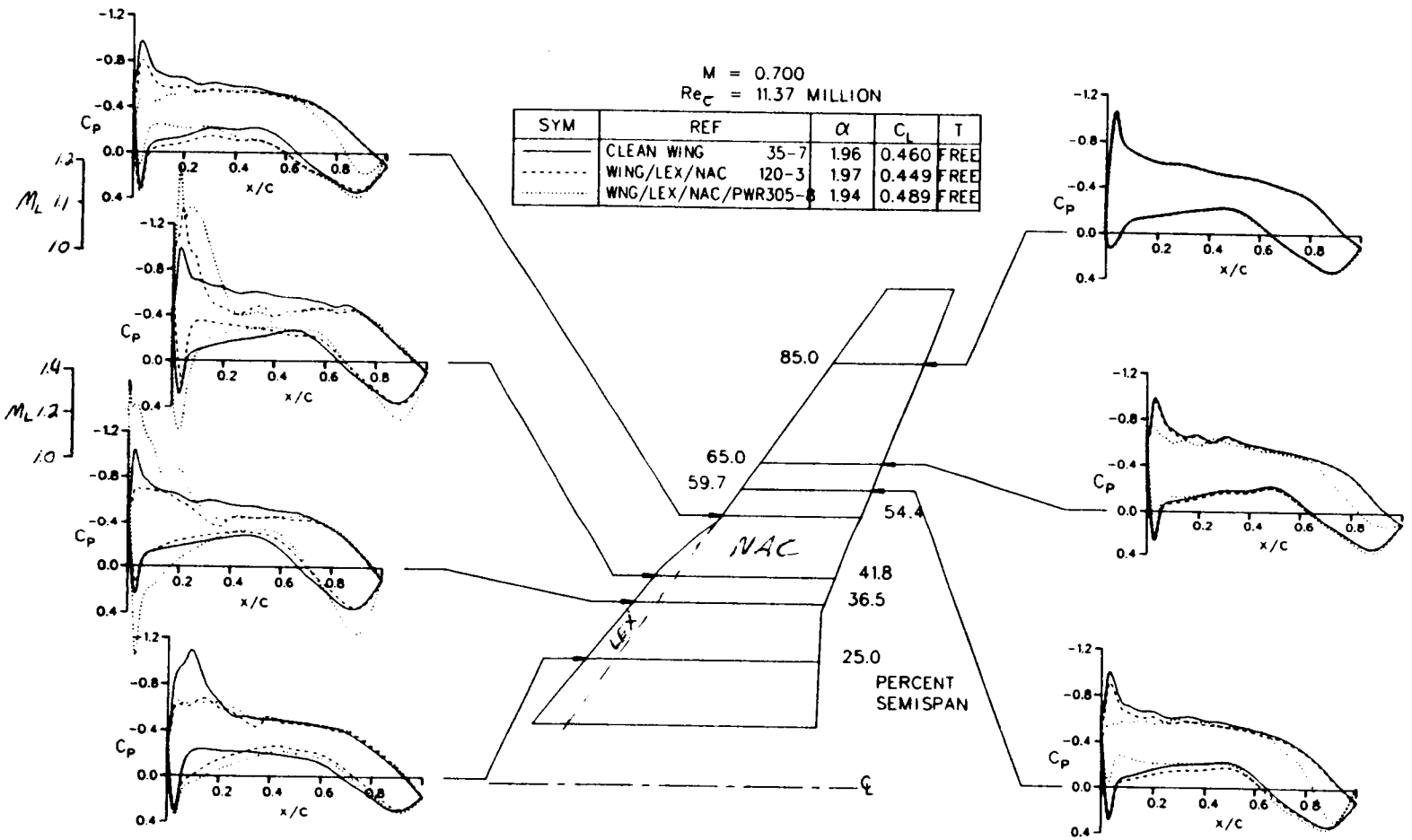

FIGURE 28. EXPERIMENTAL CHORDWISE PRESSURE DISTRIBUTIONS FOR STRAIGHT UNDERWING NACELLE WITH LEX, 0.7M$_o$, α = 2 DEGREES

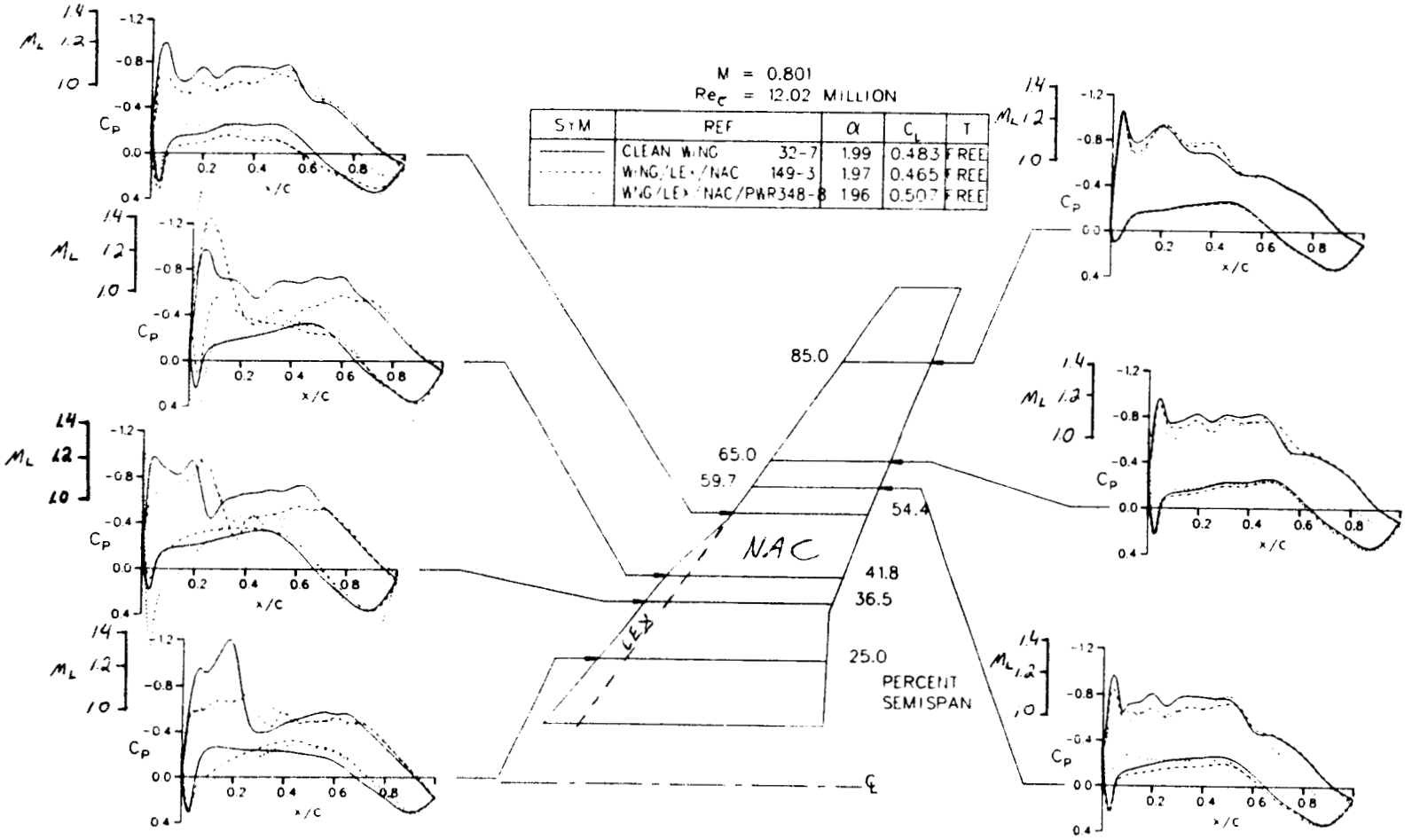

FIGURE 29. EXPERIMENTAL CHORDWISE PRESSURE DISTRIBUTIONS FOR STRAIGHT UNDERWING NACELLE WITH LEX, 0.8M_o, α = 2 DEGREES

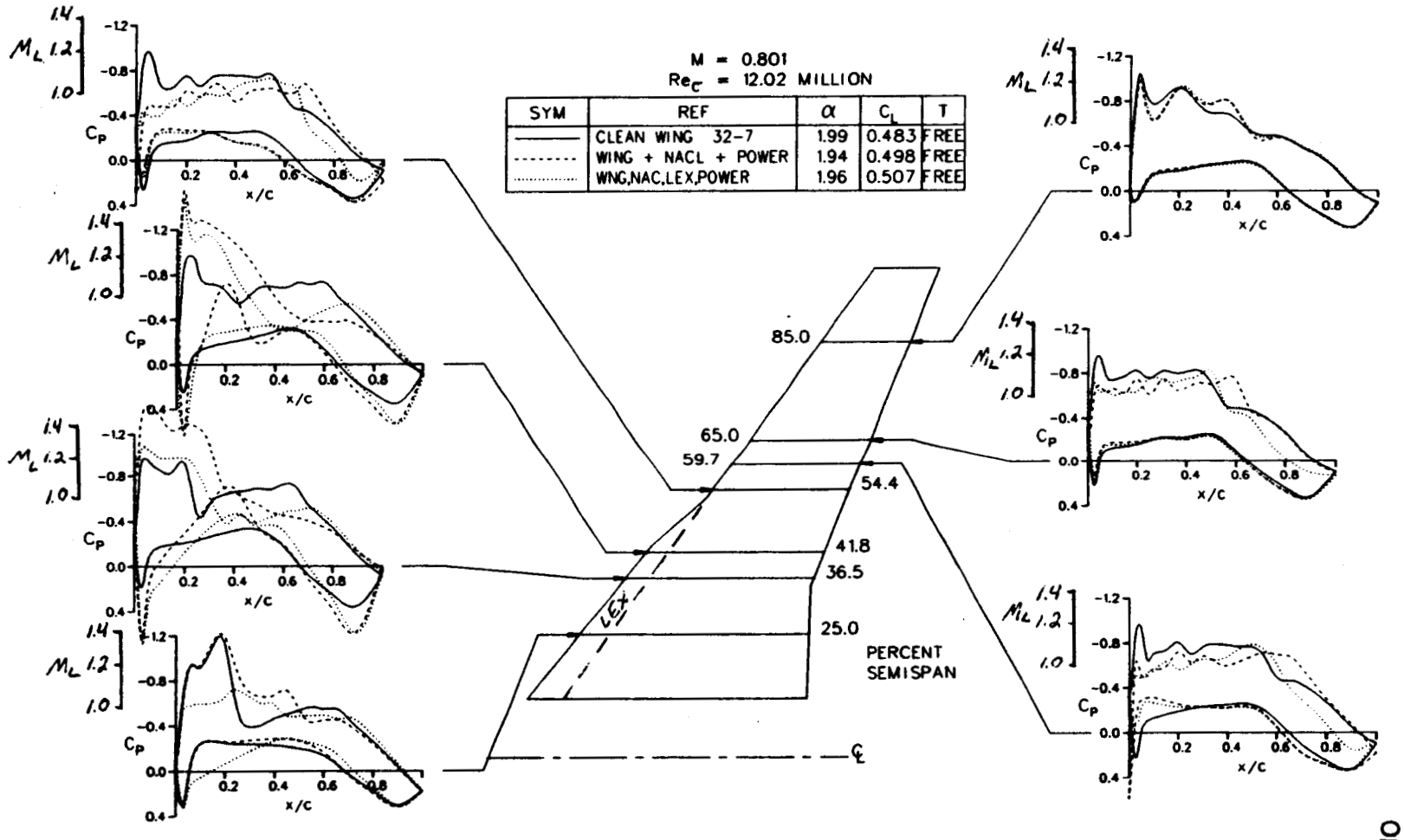

FIGURE 30. EXPERIMENTAL CHORDWISE PRESSURE DISTRIBUTIONS FOR STRAIGHT UNDERWING NACELLE WITH AND WITHOUT LEX AT M_o = 0.8 – WITH POWER

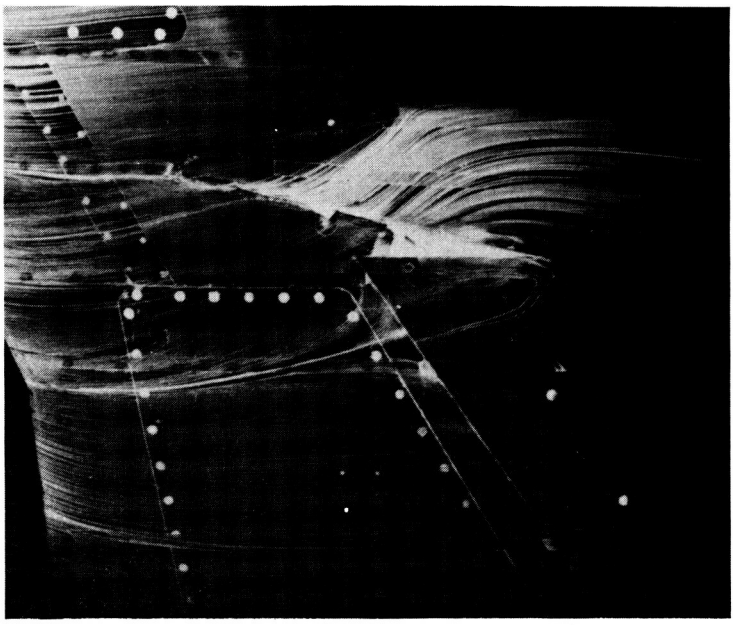

FIGURE 31. OIL FLOW PHOTOGRAPH FOR STRAIGHT UNDERWING NACELLE WITH LEX AT M_o = 0.8 – WITH POWER

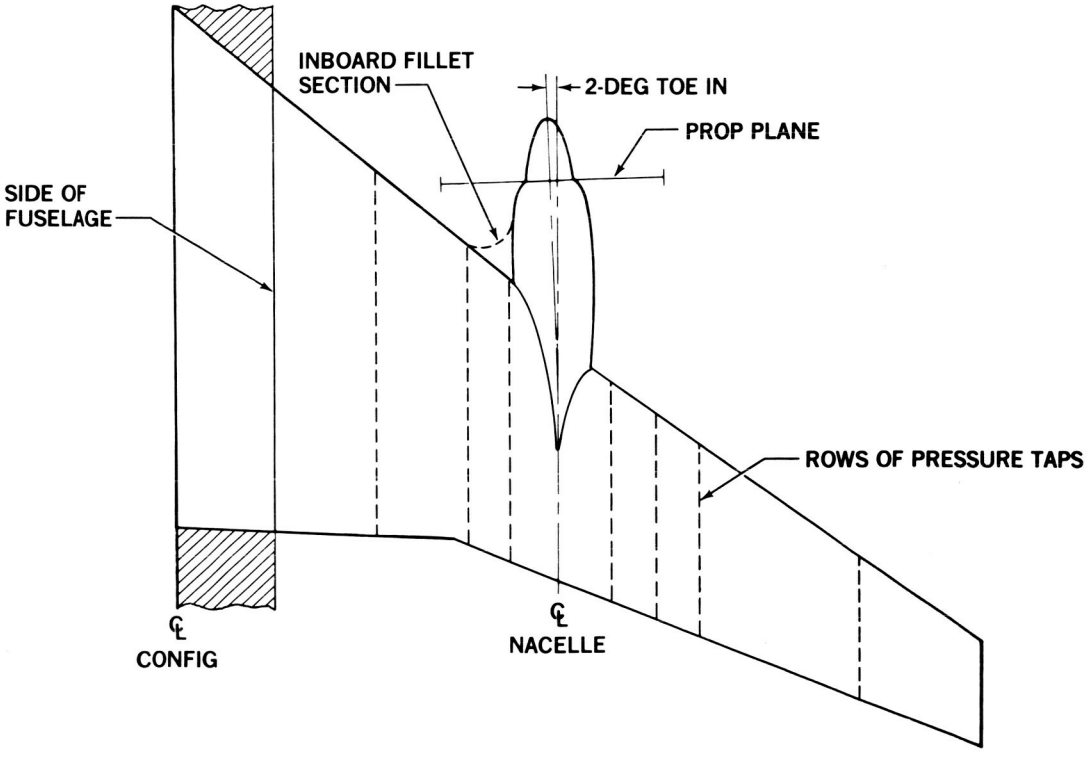

FIGURE 32. PLAN VIEW OF STRAIGHT UNDERWING NACELLE WITH LEX AND FILLET

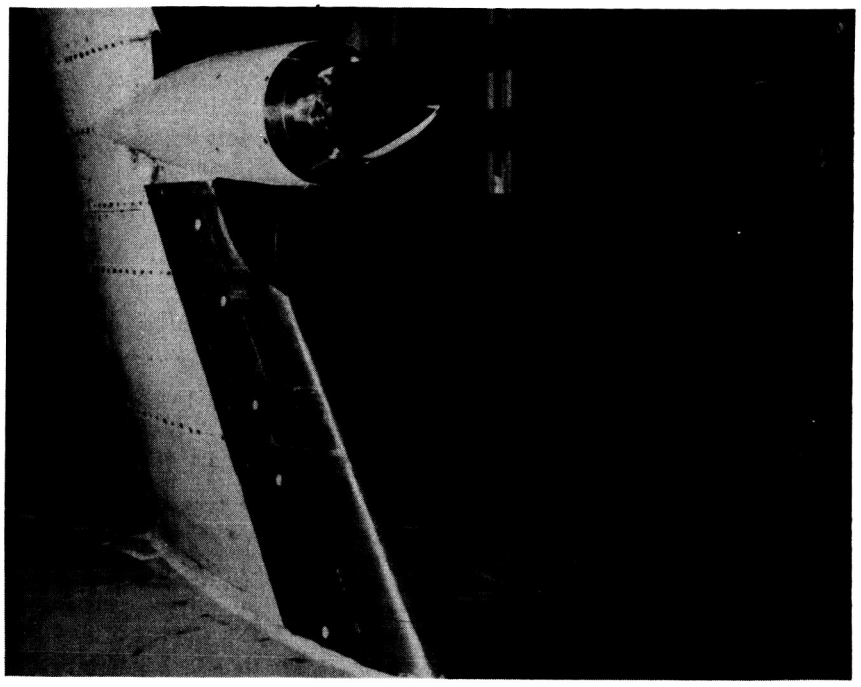

FIGURE 33. STRAIGHT UNDERWING NACELLE WITH LEX AND FILLET

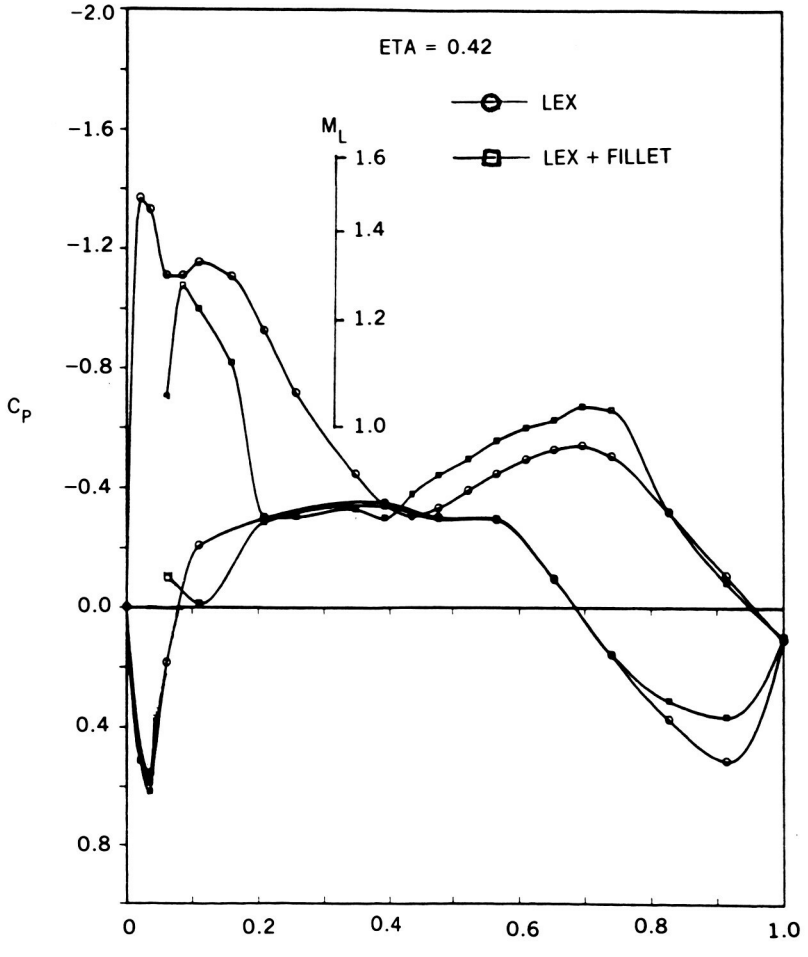

FIGURE 34. EXPERIMENTAL CHORDWISE PRESSURE DISTRIBUTION FOR STRAIGHT UNDERWING NACELLE WITH LEX AND FILLET – WITH POWER, 8250 RPM, $0.8M_o$, α = 2 DEGREES

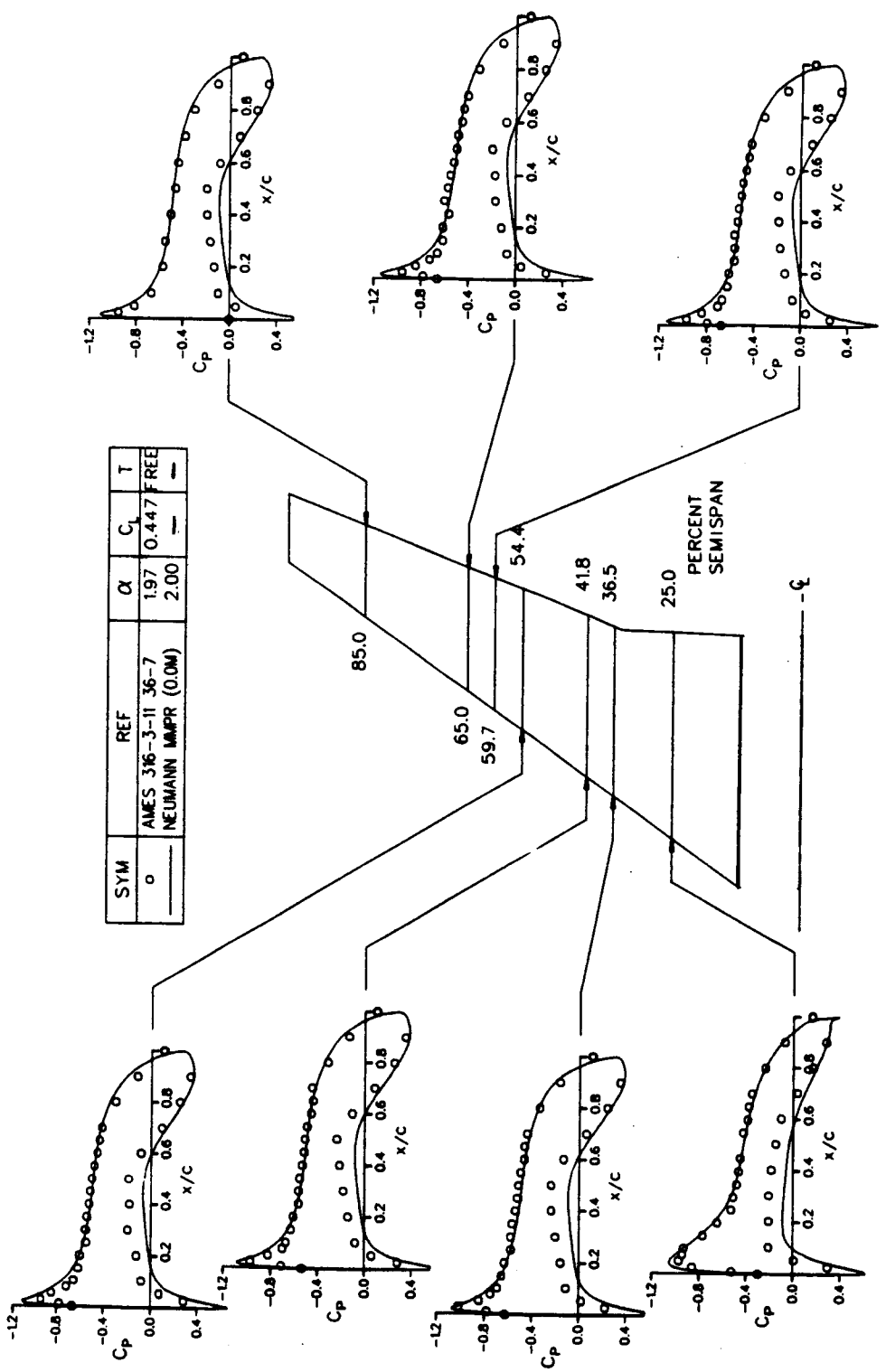

FIGURE 35. COMPARISON OF DAC-NEUMANN AND 0.6M_o DATA FOR CLEAN WING W4, α = 2 DEGREES

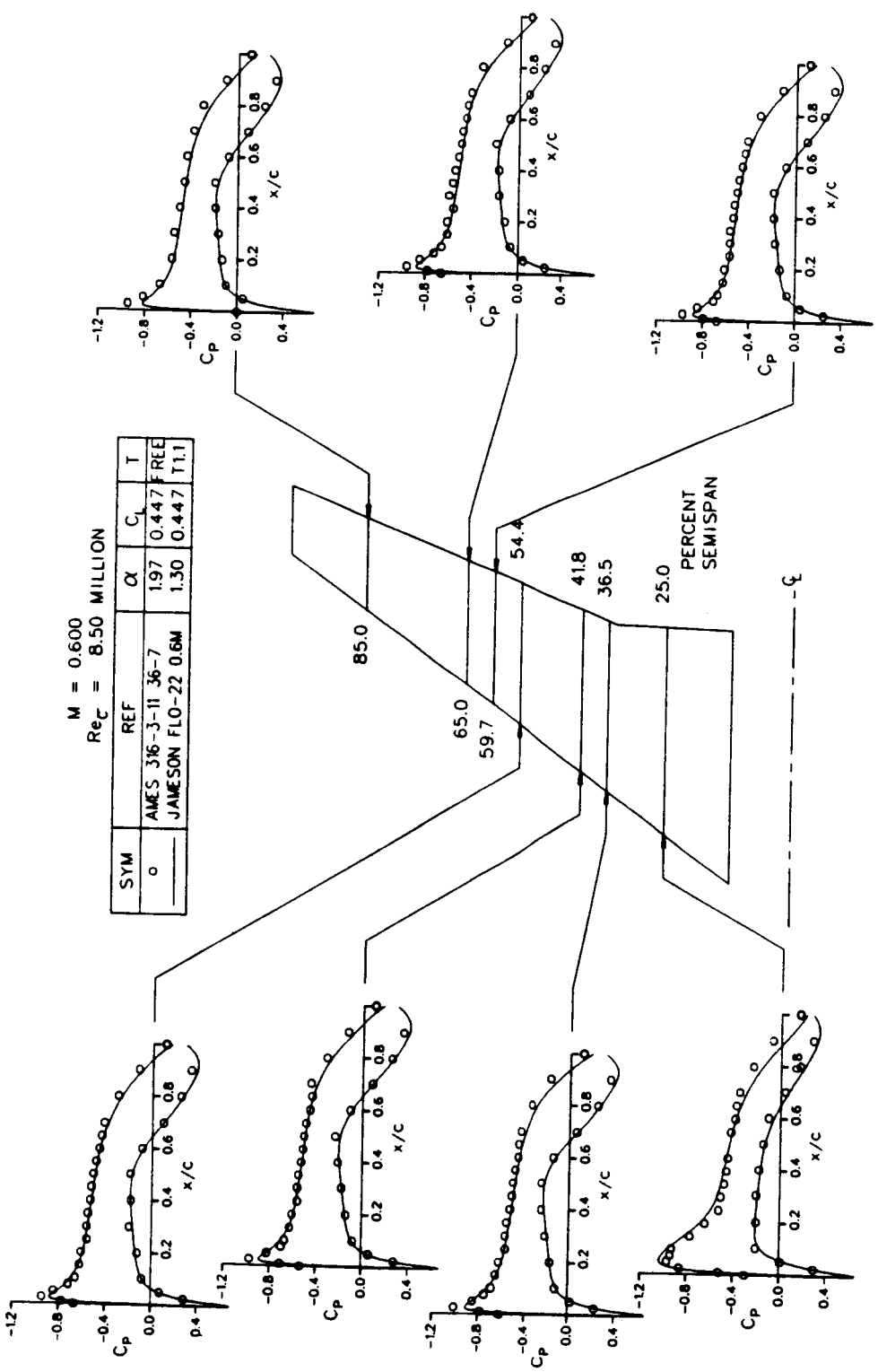

FIGURE 36. COMPARISON OF DAC-JAMESON AND DATA FOR CLEAN WING W4, $0.6M_D$, C_L = 0.45

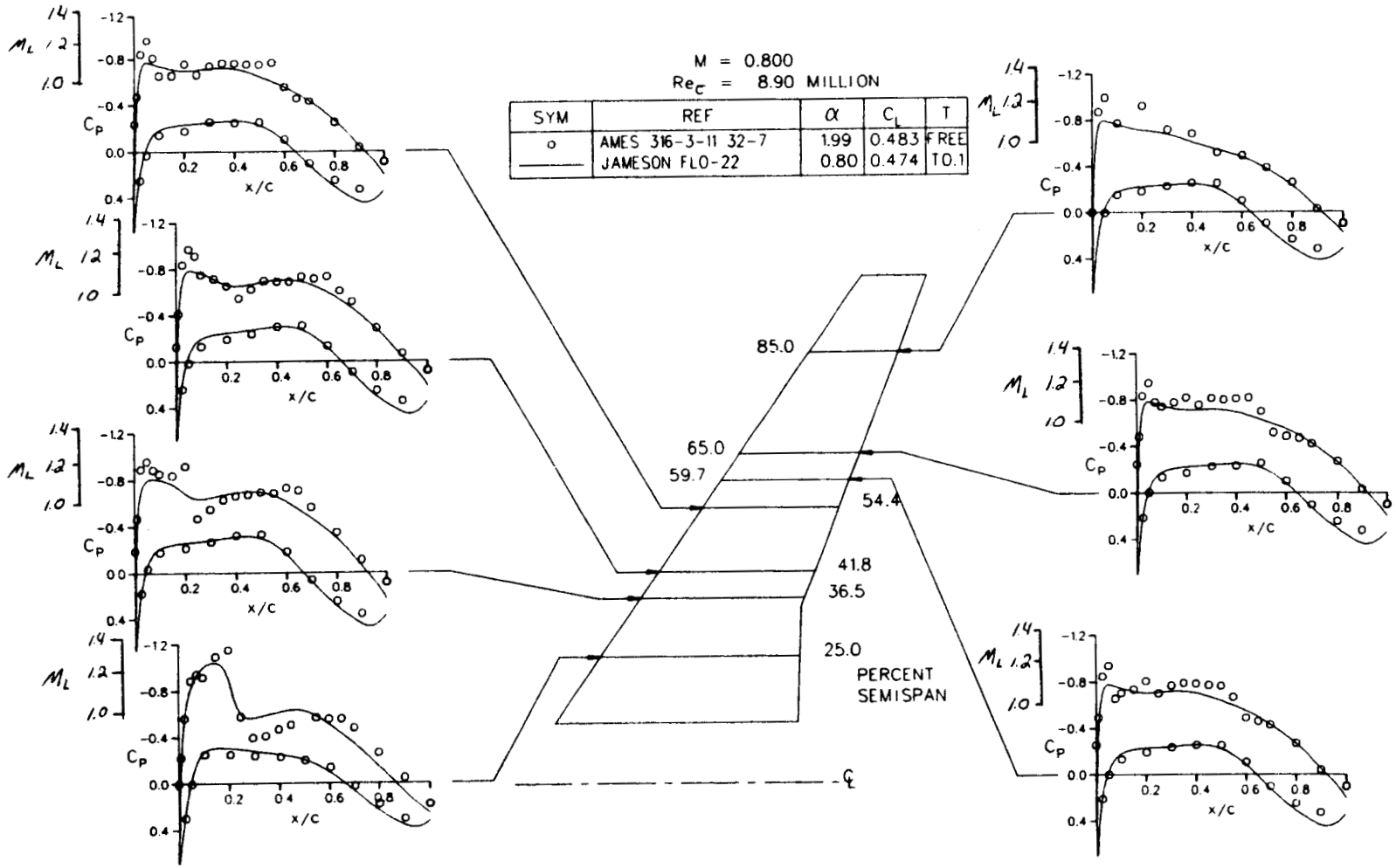

FIGURE 37. COMPARISON OF DAC-JAMESON AND DATA FOR CLEAN WING W4, 0.8M$_o$, C$_L$ = 0.48

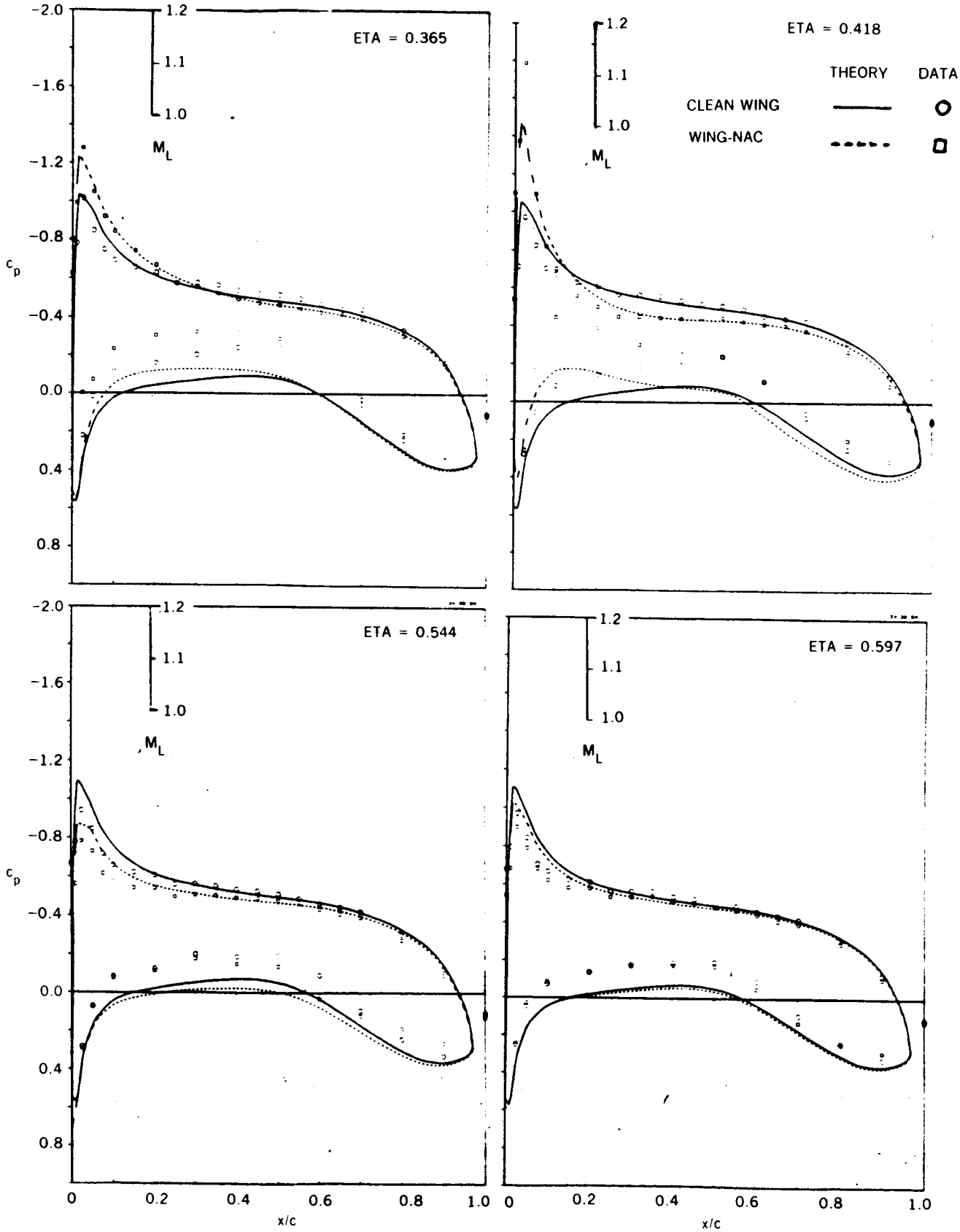

FIGURE 38. COMPARISON OF DAC-NEUMANN AND 0.6M_o DATA FOR STRAIGHT UNDERWING NACELLE — NO POWER, α = 2 DEGREES

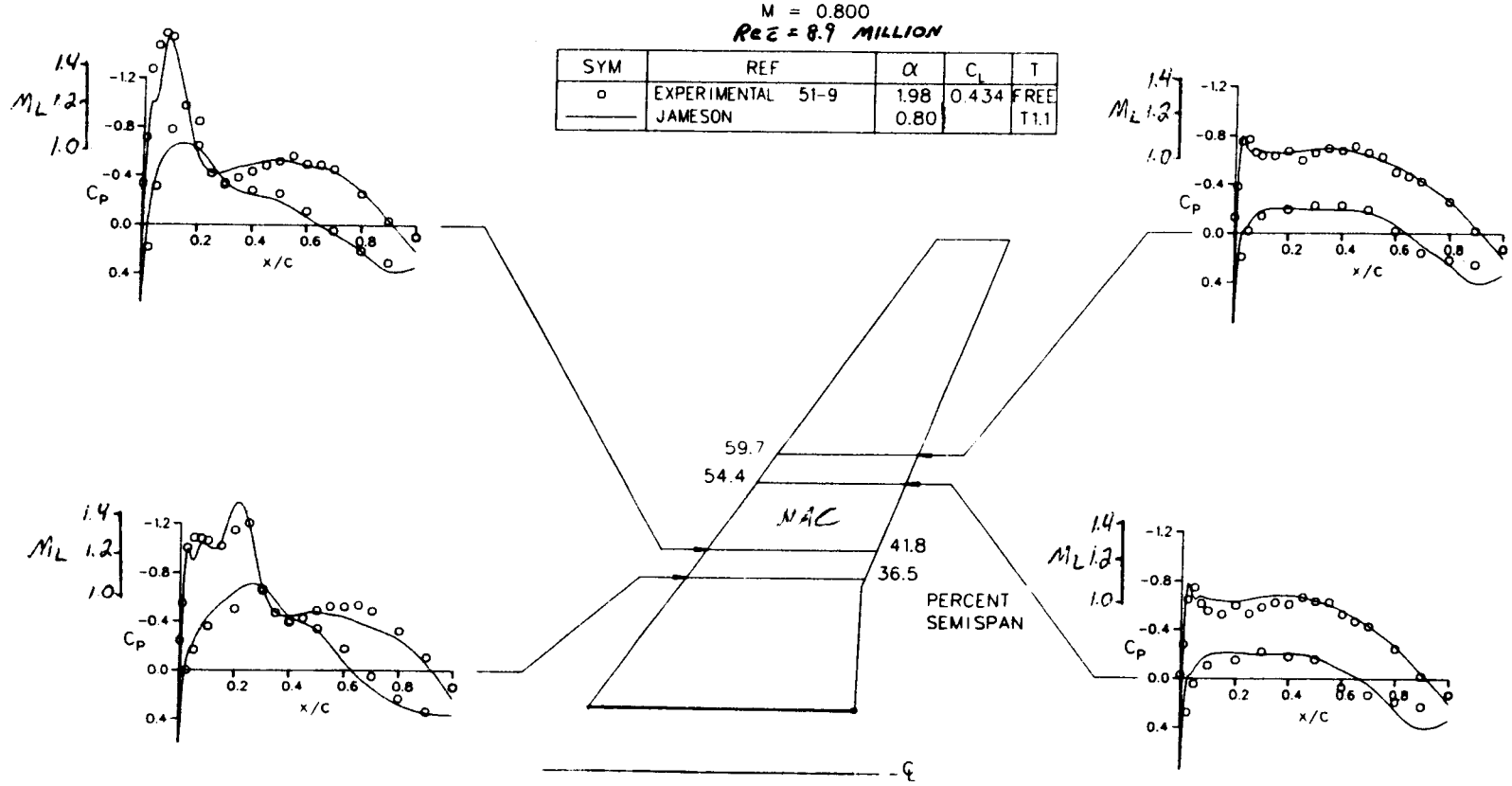

FIGURE 39. COMPARISON OF DAC-JAMESON AND DATA FOR STRAIGHT UNDERWING NACELLE – NO POWER, $0.8M_o$

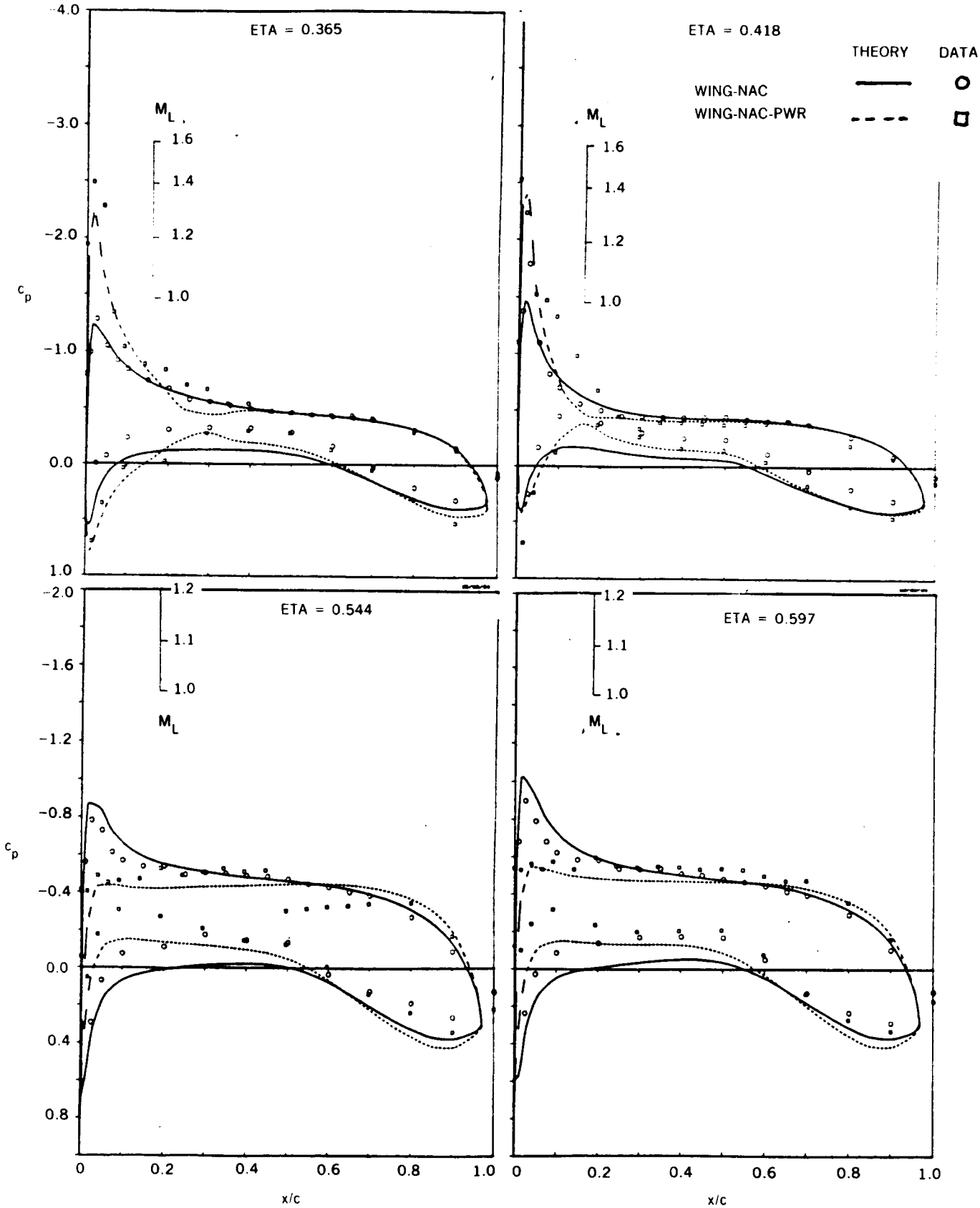

FIGURE 40. COMPARISON OF DAC-NEUMANN AND 0.6M_o DATA FOR STRAIGHT UNDERWING NACELLE — WITH POWER, α = 2 DEGREES

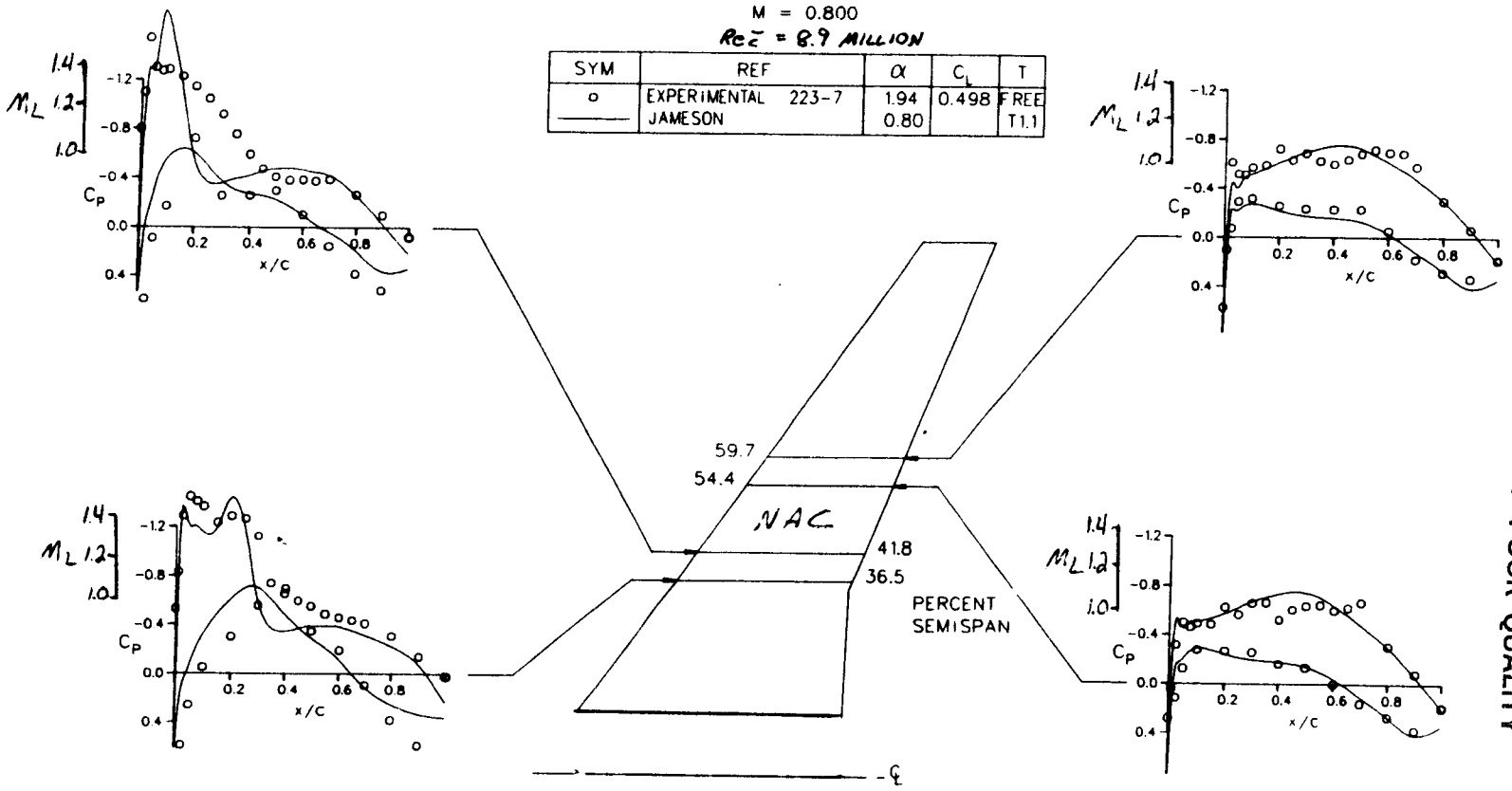

FIGURE 41. COMPARISON OF DAC-JAMESON AND DATA FOR STRAIGHT UNDERWING NACELLE – WITH POWER, $0.8M_o$

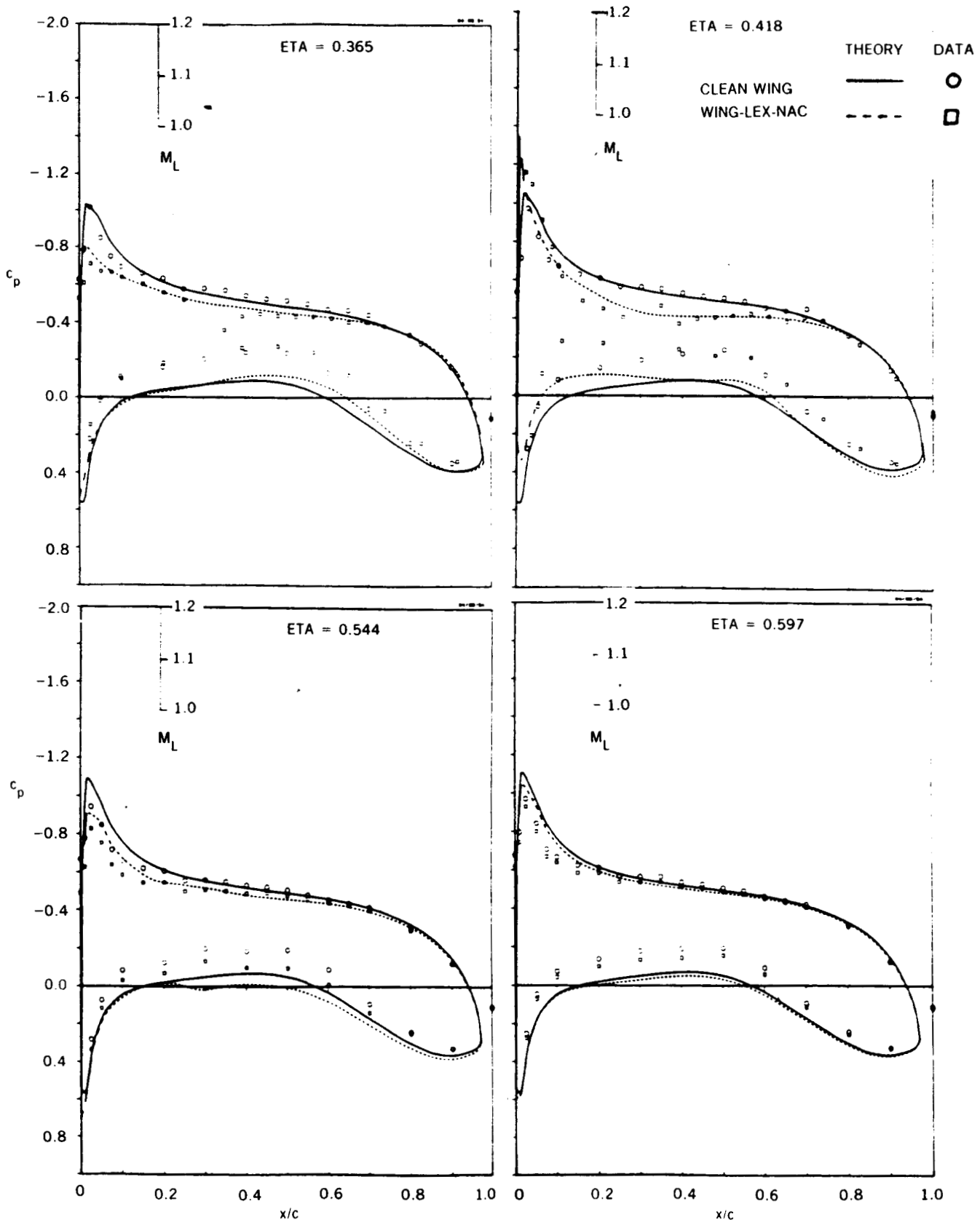

FIGURE 42. COMPARISON OF DAC-NEUMANN AND 0.6M_0 DATA FOR STRAIGHT UNDERWING NACELLE WITH LEX – NO POWER, α = 2 DEGREES

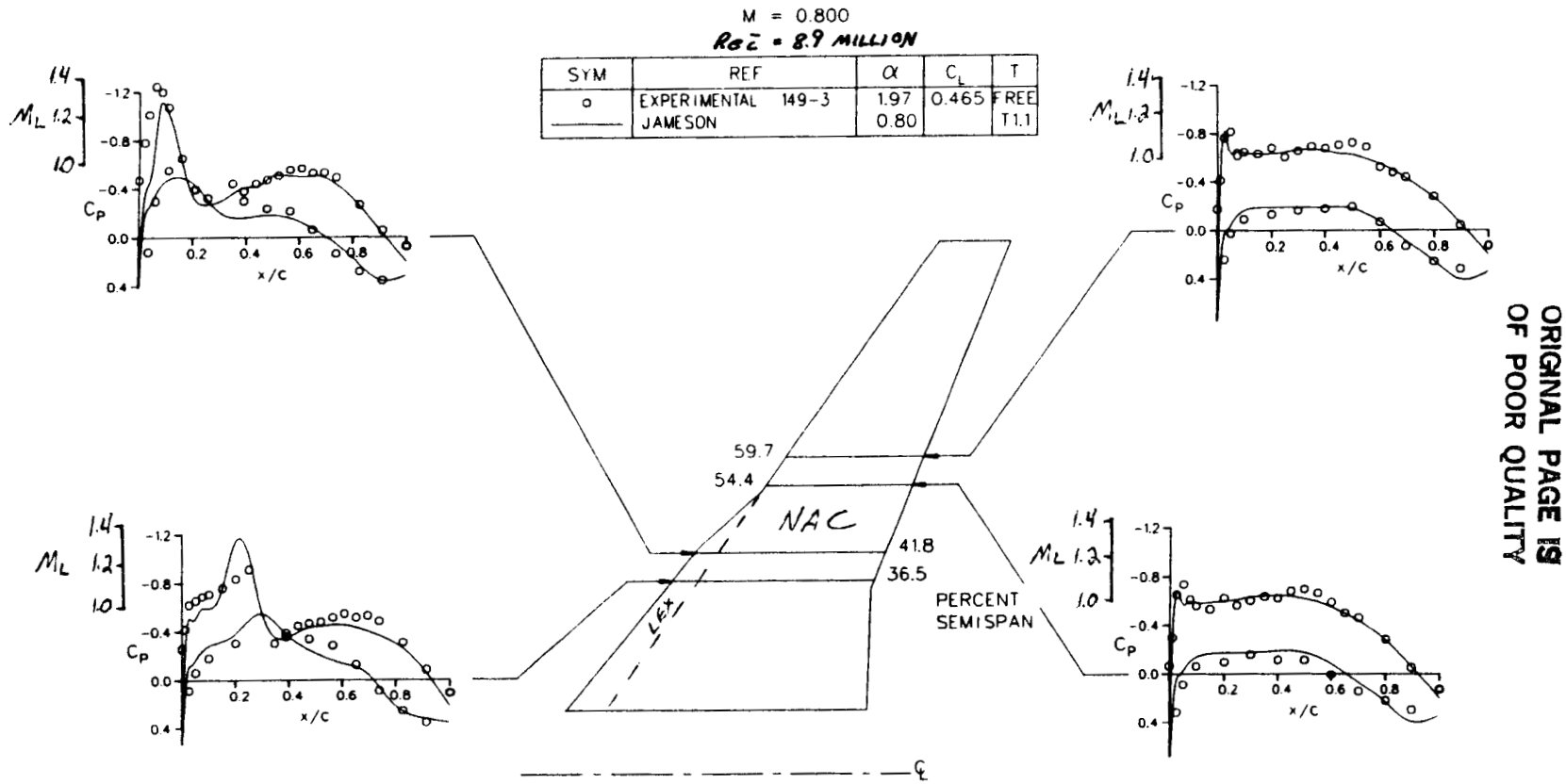

FIGURE 43. COMPARISON OF DAC-JAMESON AND DATA FOR STRAIGHT UNDERWING NACELLE WITH LEX – NO POWER, 0.8M_o

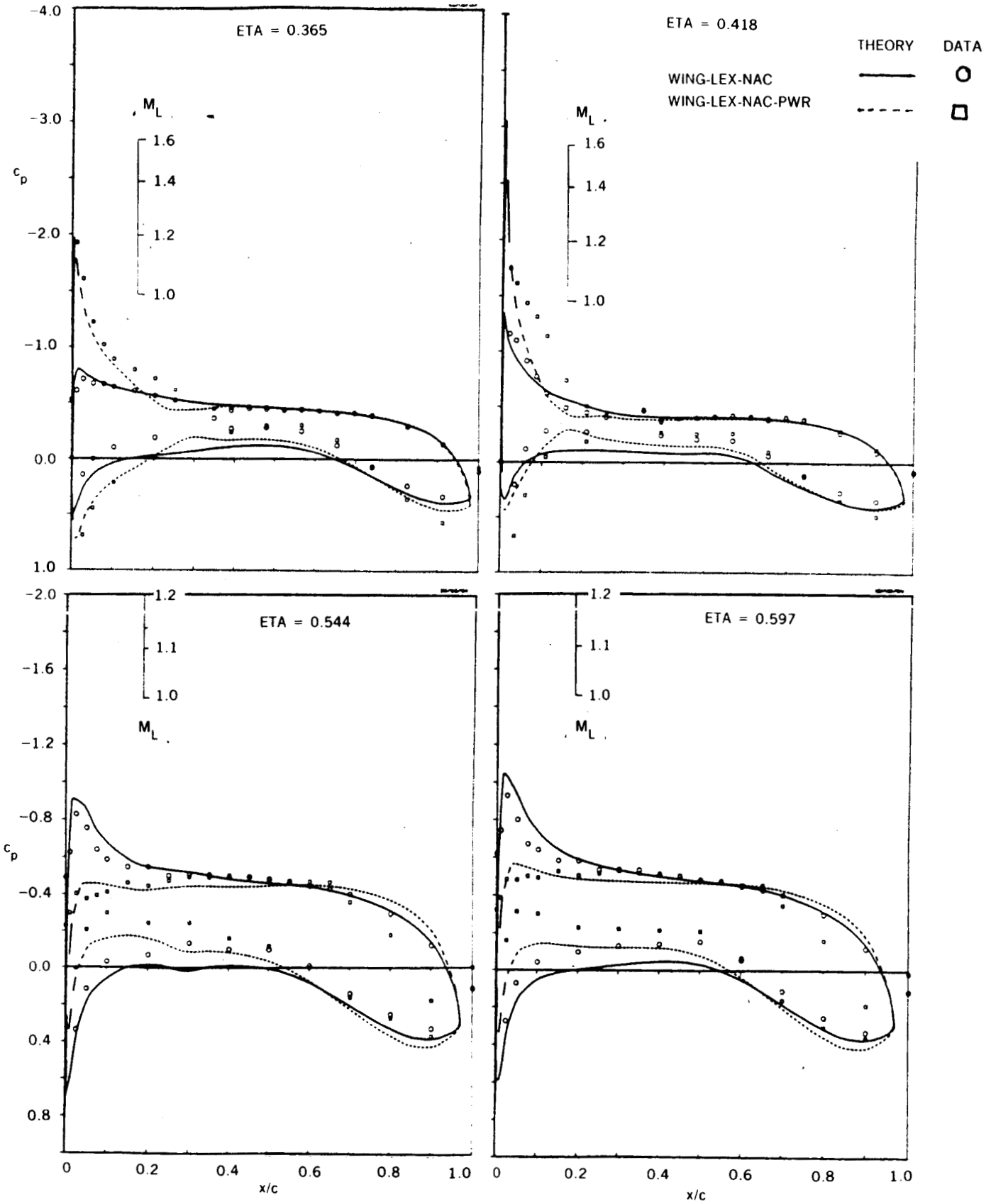

FIGURE 44. COMPARISON OF DAC-NEUMANN AND 0.6M_o DATA FOR STRAIGHT UNDERWING NACELLE WITH LEX – WITH POWER, α = 2 DEGREES

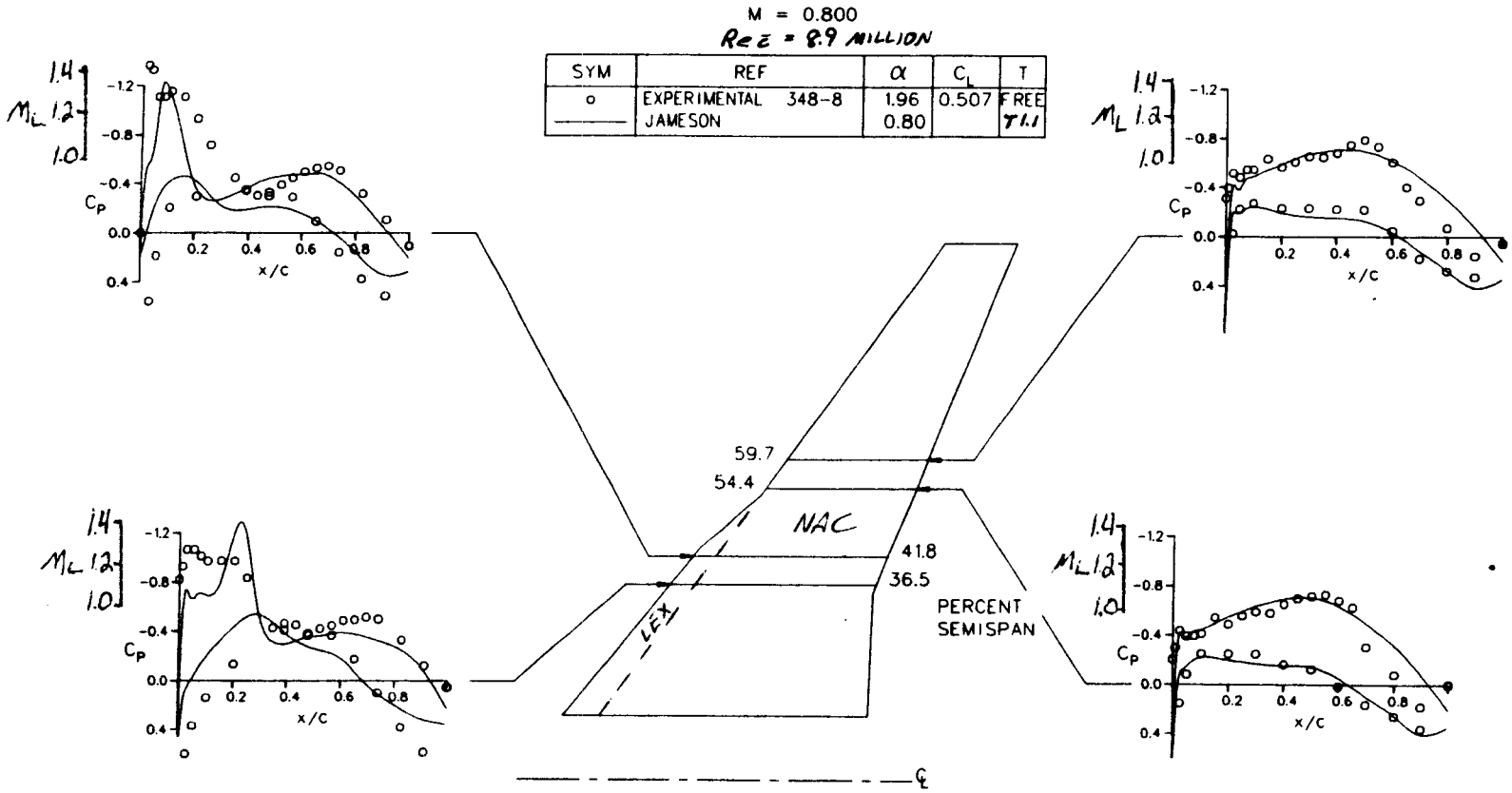

FIGURE 45. COMPARISON OF DAC-JAMESON AND DATA FOR STRAIGHT UNDERWING NACELLE WITH LEX – WITH POWER, $0.8M_o$

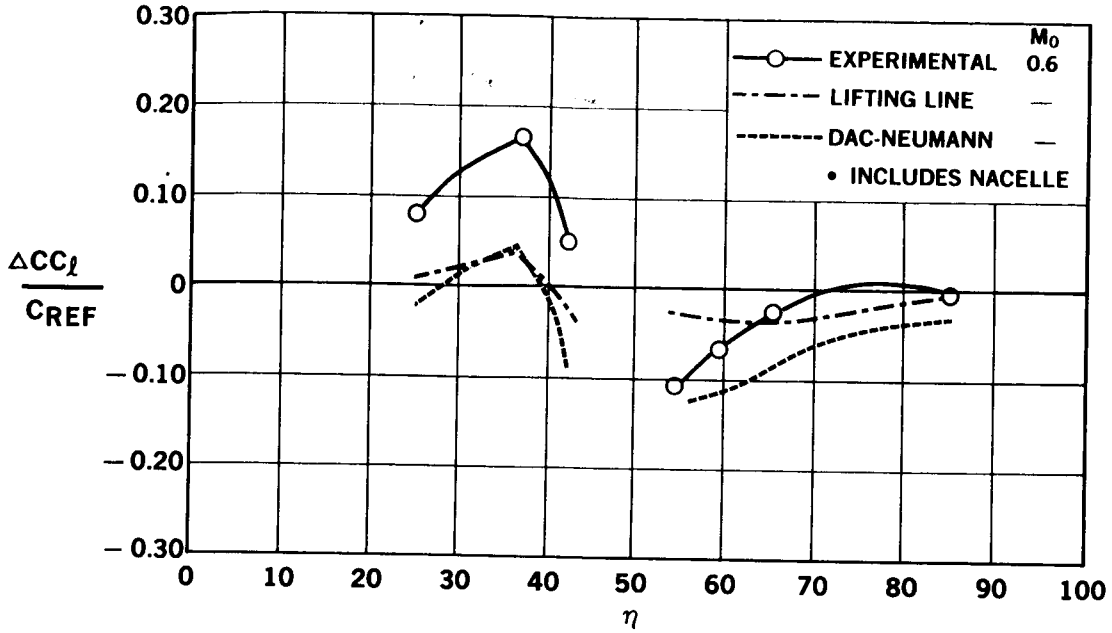

FIGURE 46. DATA-THEORY COMPARISON OF SPAN LOADING INCREMENTS DUE TO POWER FOR STRAIGHT UNDERWING NACELLE

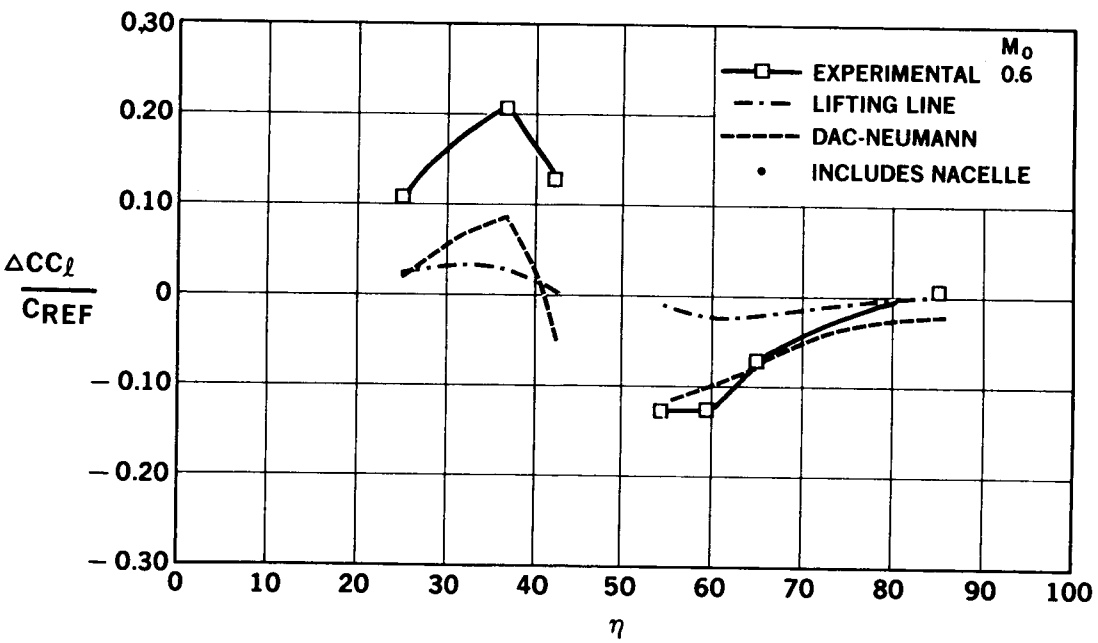

FIGURE 47. DATA-THEORY COMPARISON OF SPAN LOADING INCREMENTS DUE TO POWER FOR STRAIGHT UNDERWING NACELLE WITH LEX

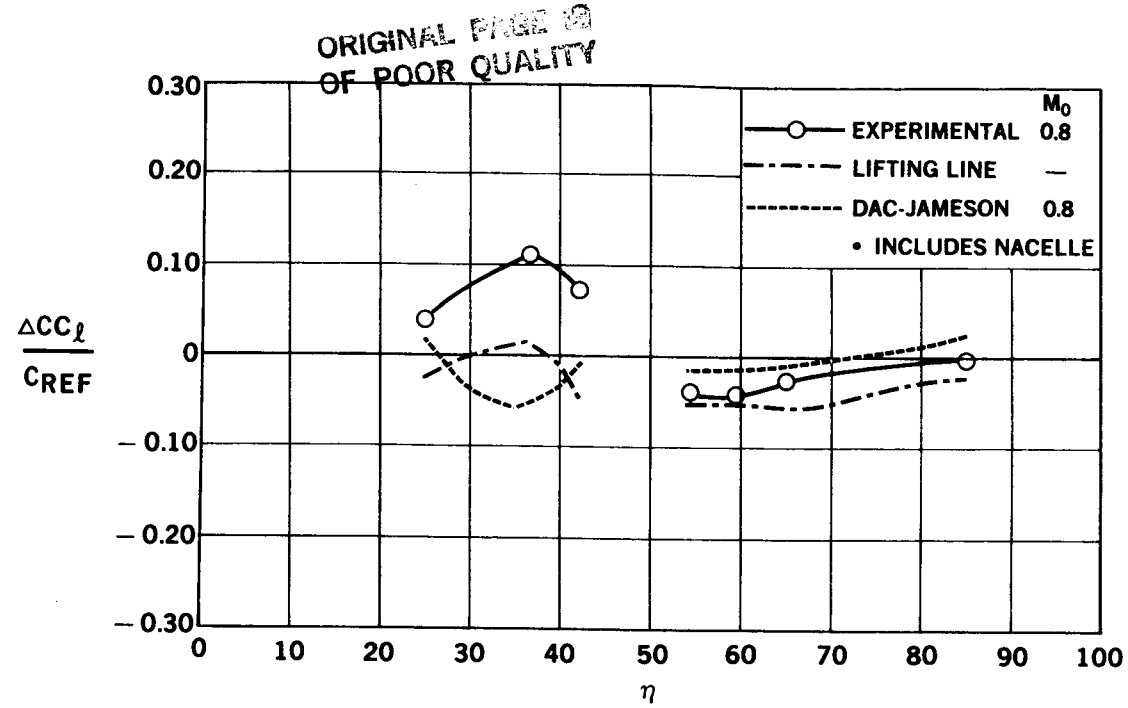

FIGURE 48. DATA-THEORY COMPARISON OF SPAN LOADING INCREMENTS DUE TO POWER FOR STRAIGHT UNDERWING NACELLE

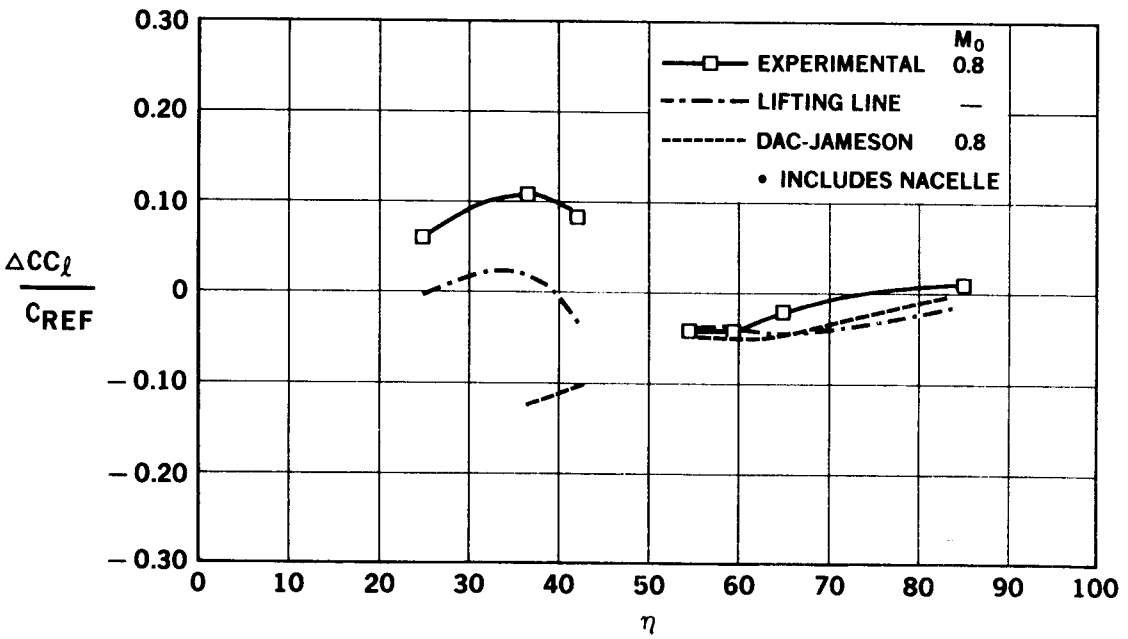

FIGURE 49. DATA-THEORY COMPARISON OF SPAN LOADING INCREMENTS DUE TO POWER FOR STRAIGHT UNDERWING NACELLE WITH LEX

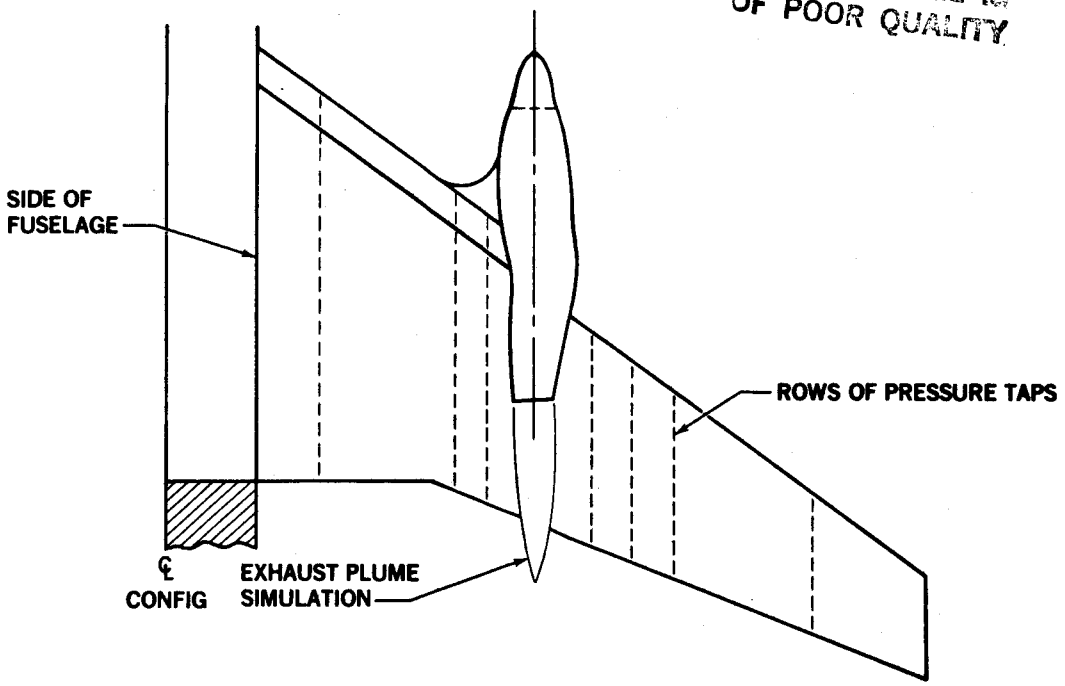

FIGURE 50. PLAN VIEW OF OVERWING CONTOURED NACELLE

FIGURE 51. SIDE VIEW OF OVERWING CONTOURED NACELLE

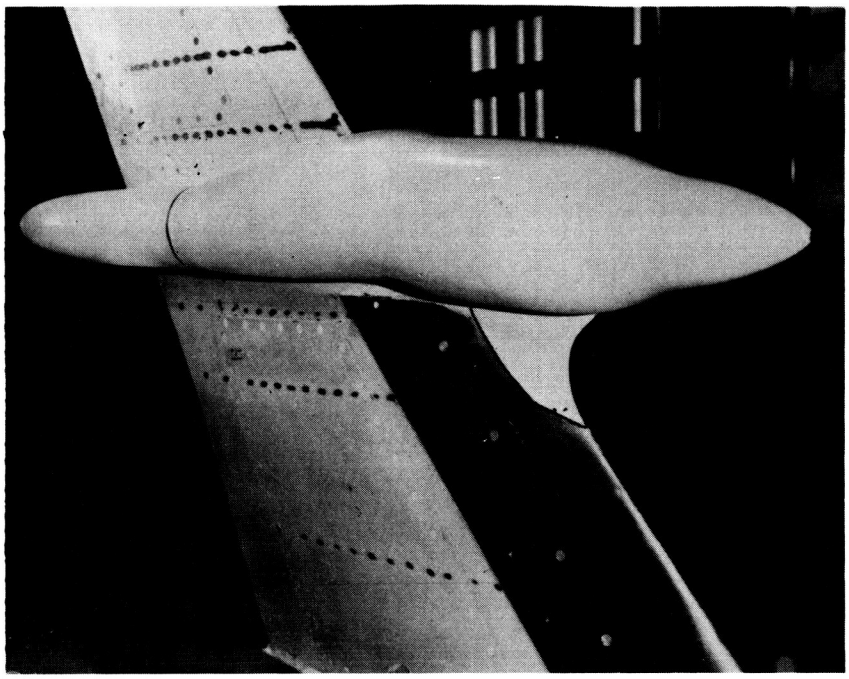

FIGURE 52. CONTOURED OVERWING NACELLE WITH LEX AND FILLET INSTALLED IN AMES 11-FOOT TUNNEL

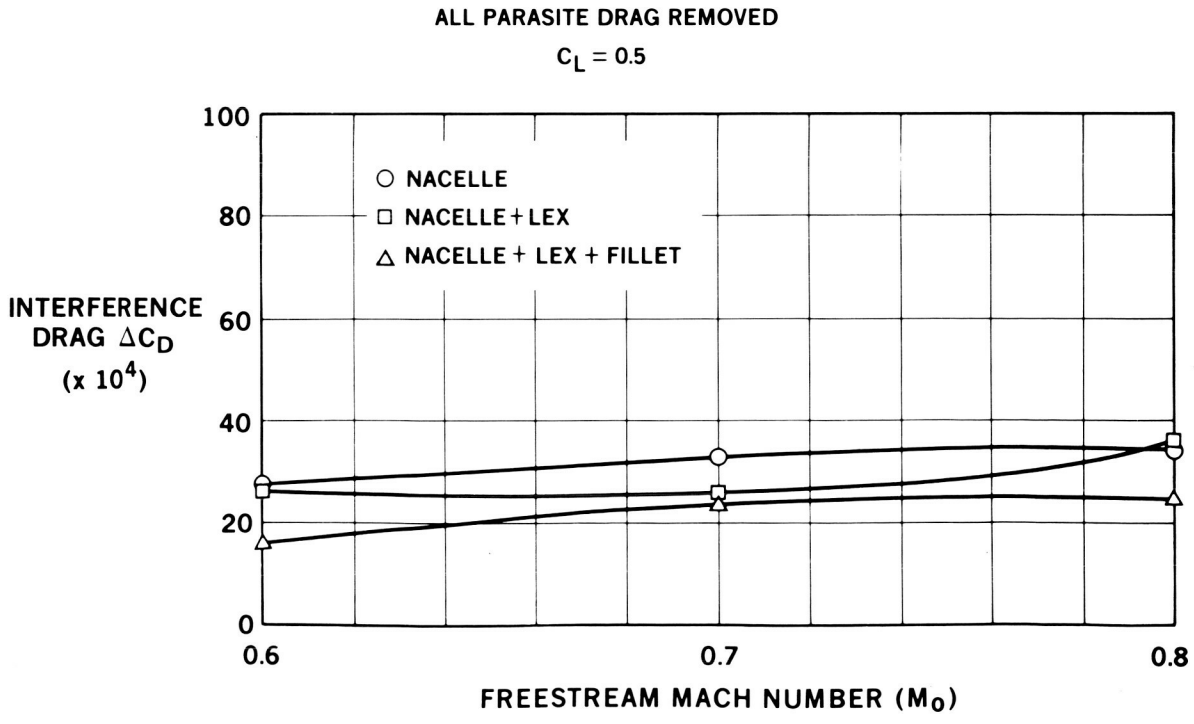

FIGURE 53. INTERFERENCE DRAG LEVELS FOR CONTOURED OVERWING NACELLE

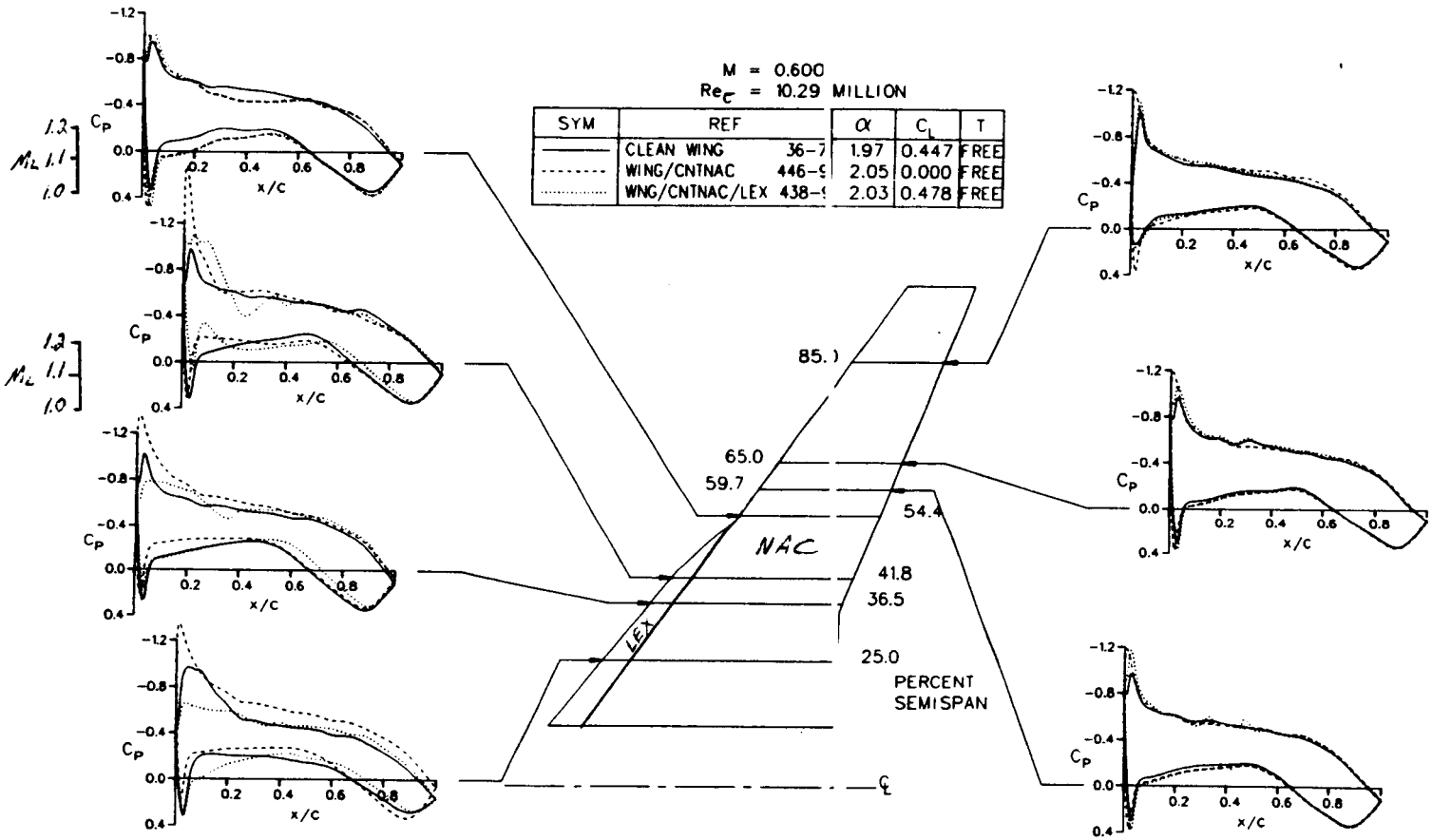

FIGURE 54. EXPERIMENTAL CHORDWISE PRESSURE DISTRIBUTIONS FOR CONTOURED OVERWING NACELLE, 0.6 M_0, α = 2 DEGREES

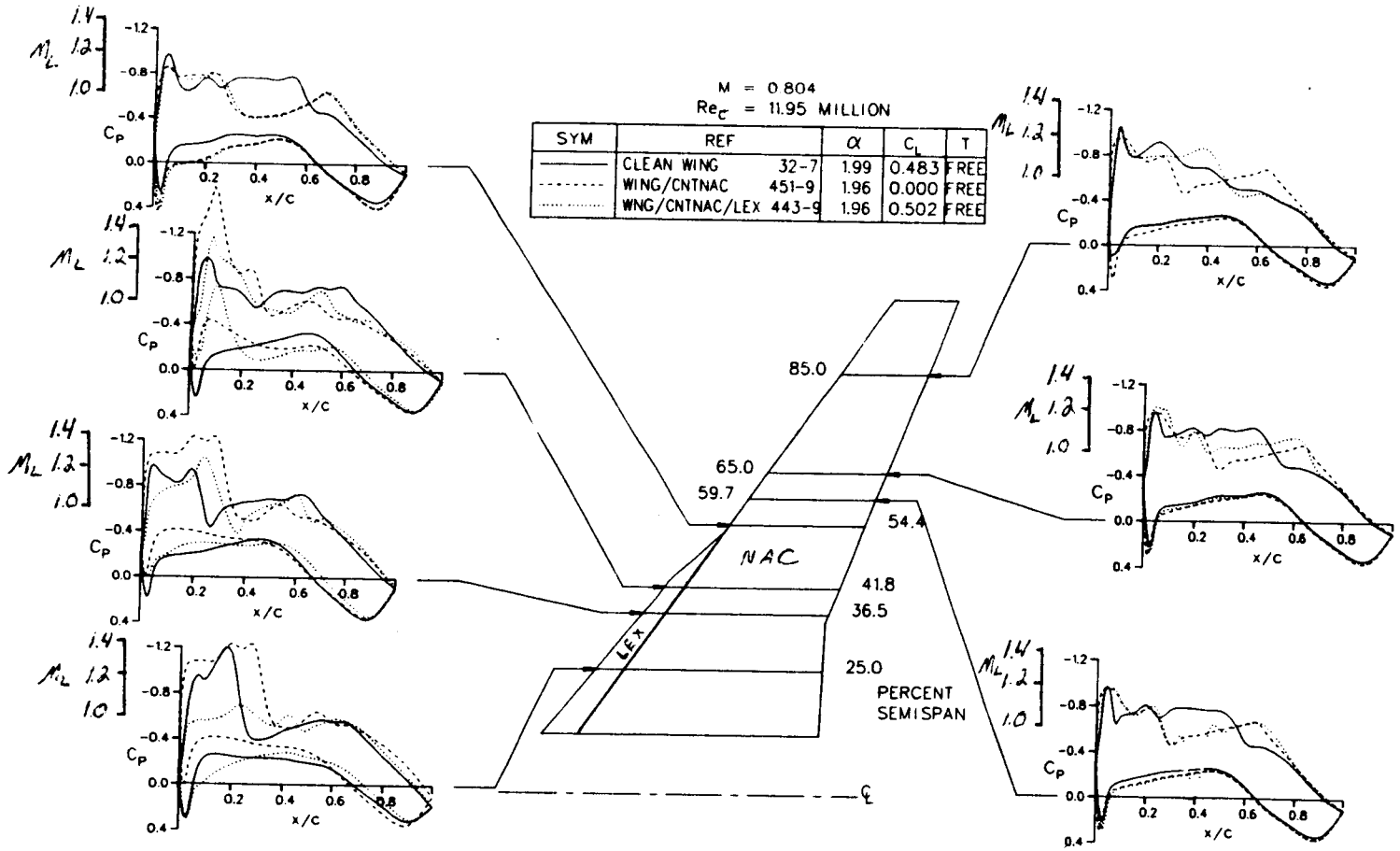

FIGURE 55. EXPERIMENTAL CHORDWISE PRESSURE DISTRIBUTIONS FOR CONTOURED OVERWING NACELLE, 0.8 M_o, α = 2 DEGREES

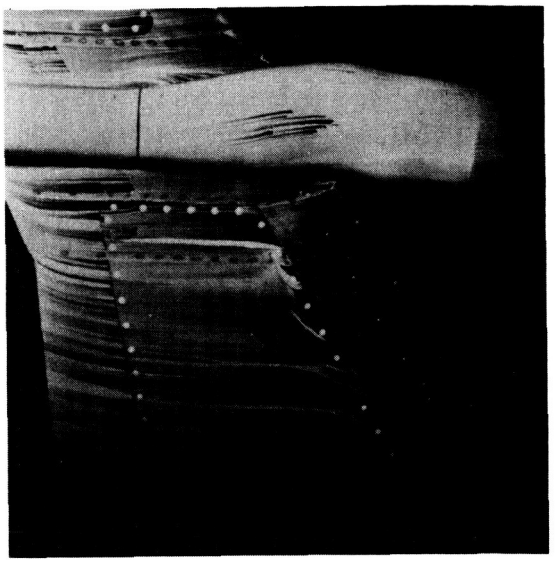

$M_0 = 0.8$
$\alpha = 2$ DEG

FIGURE 56. OIL FLOW-PHOTOGRAPH FOR CONTOURED OVERWING NACELLE, NO POWER

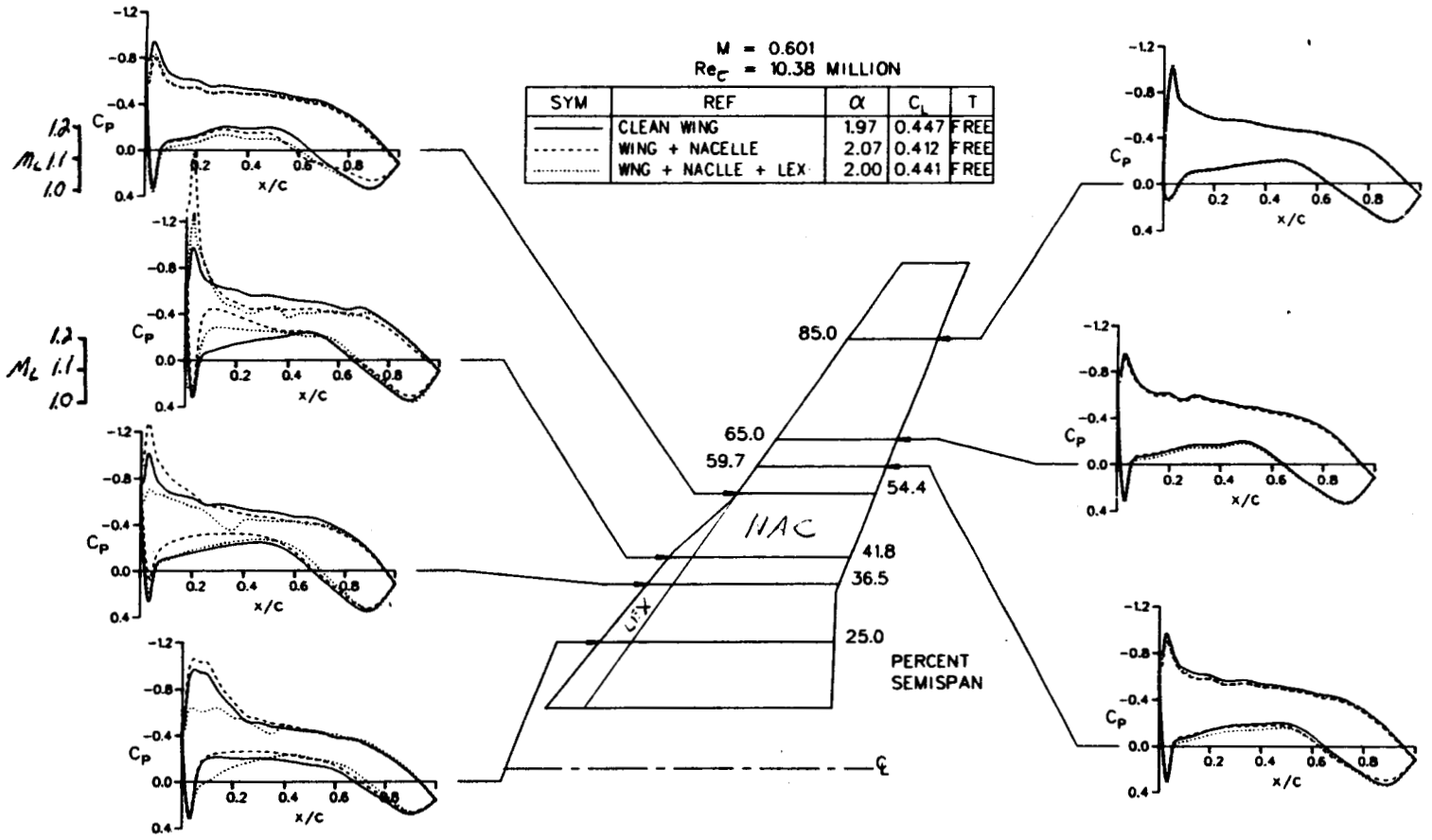

FIGURE 57. EXPERIMENTAL CHORDWISE PRESSURE DISTRIBUTIONS FOR STRAIGHT UNDERWING NACELLE WITH AND WITHOUT LEX, M_o = 0.6, α = 2 DEGREES

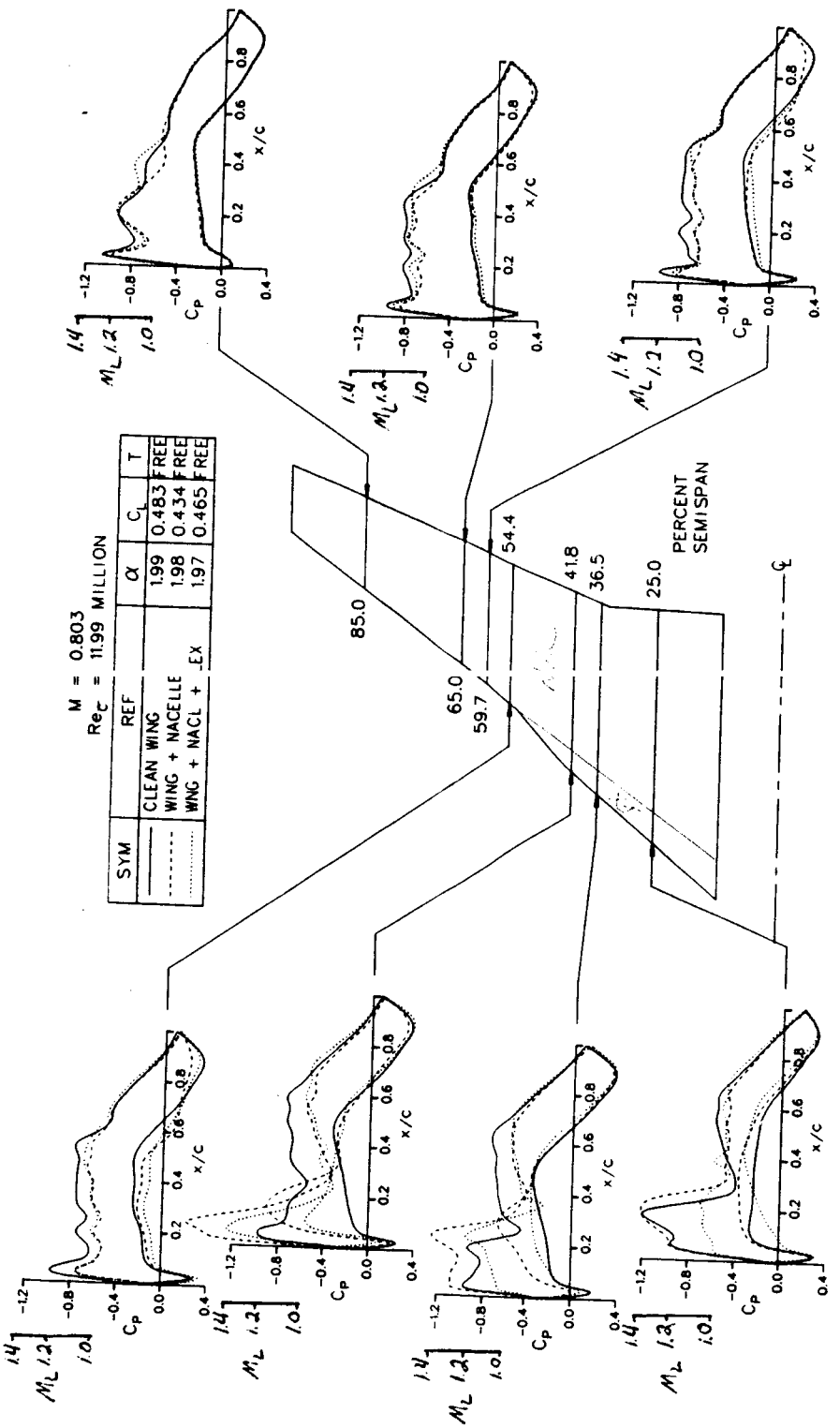

FIGURE 58. EXPERIMENTAL CHORDWISE PRESSURE DISTRIBUTIONS FOR STRAIGHT UNDERWING NACELLE WITH AND WITHOUT LEX, M_o = 0.8, α = 2 DEGREES

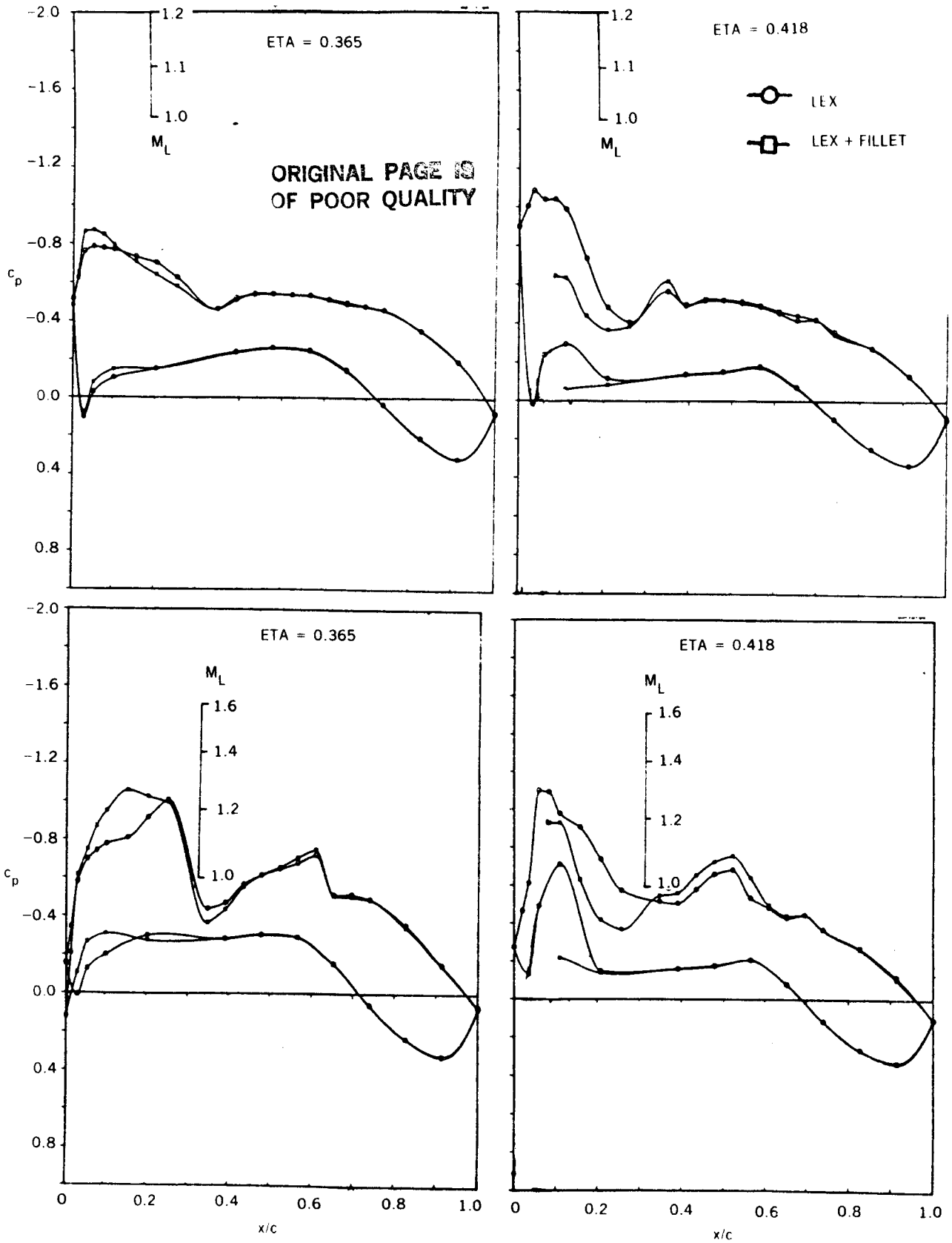

FIGURE 59. EXPERIMENTAL CHORDWISE PRESSURE DISTRIBUTIONS FOR CONTOURED OVERWING NACELLE WITH LEX AND FILLET, M_o = 0.6 AND 0.8, α = 2 DEGREES

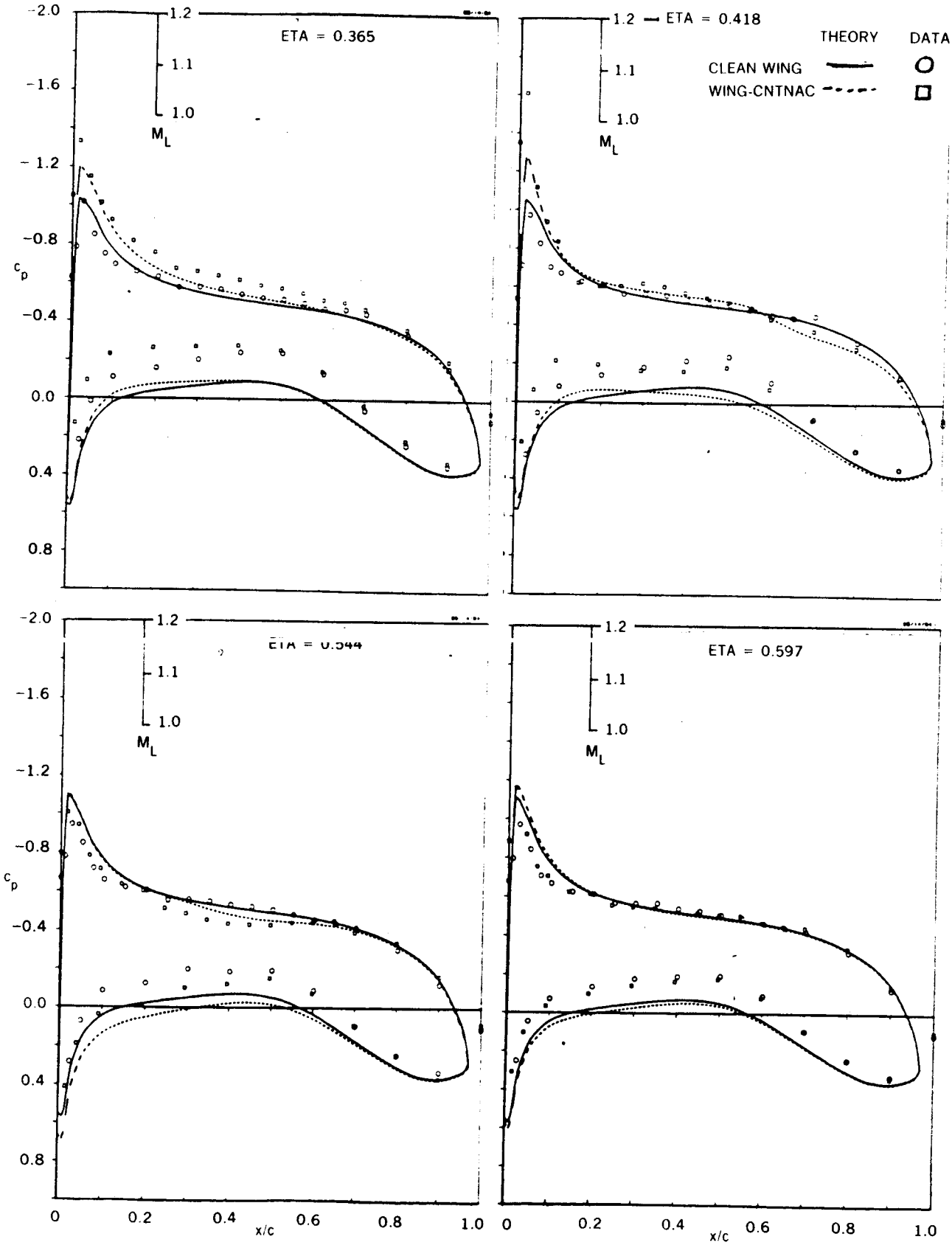

FIGURE 60. COMPARISON OF DAC-NEUMANN AND DATA FOR CONTOURED OVERWING NACELLE – NO POWER

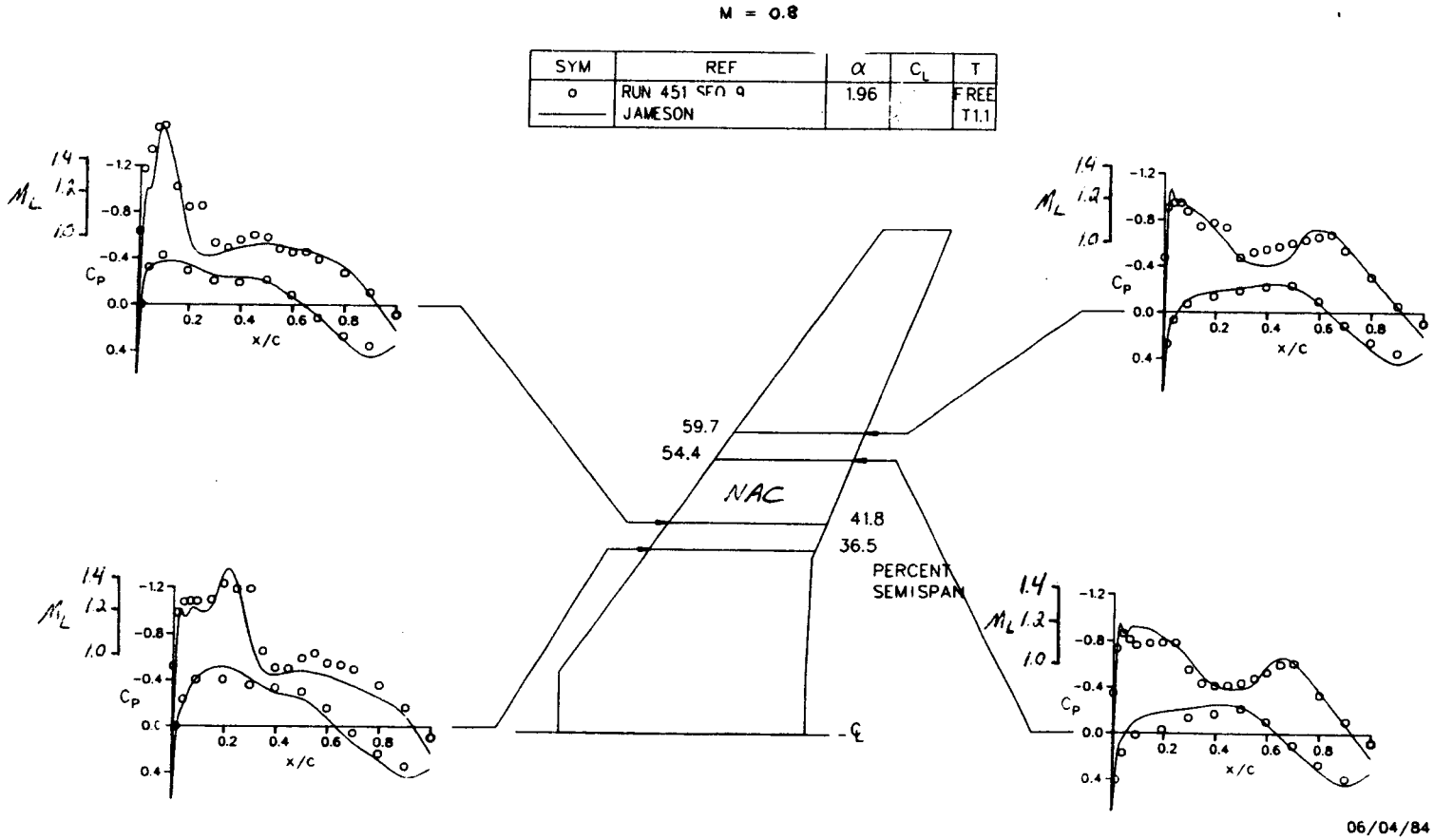

FIGURE 61. COMPARISON OF DAC-JAMESON AND DATA FOR CONTOURED OVERWING NACELLE – NO POWER

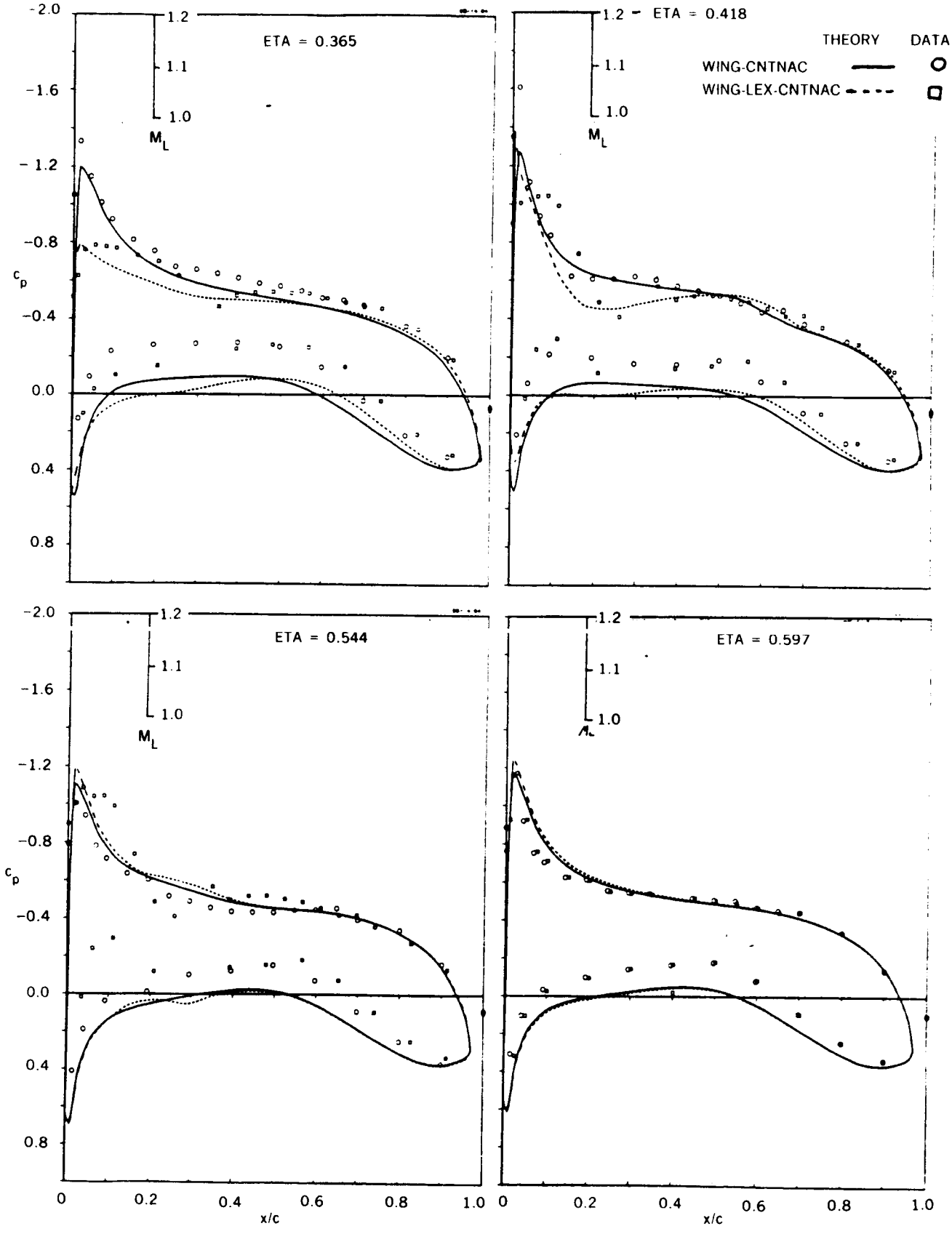

FIGURE 62. COMPARISON OF DAC-NEUMANN AND DATA FOR CONTOURED OVERWING NACELLE WITH LEX – NO POWER

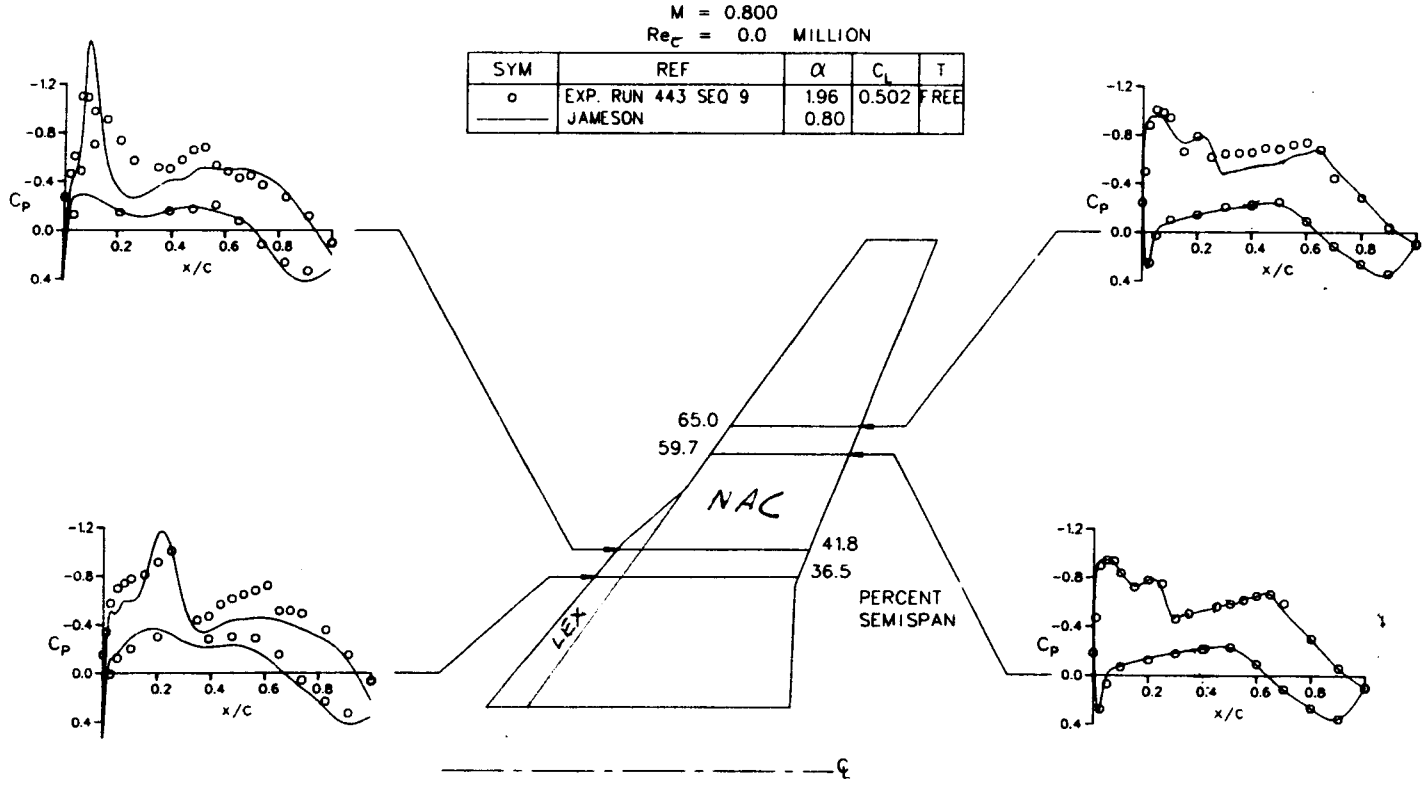

FIGURE 63. COMPARISON OF DAC-JAMESON AND DATA FOR CONTOURED OVERWING NACELLE WITH LEX – NO POWER

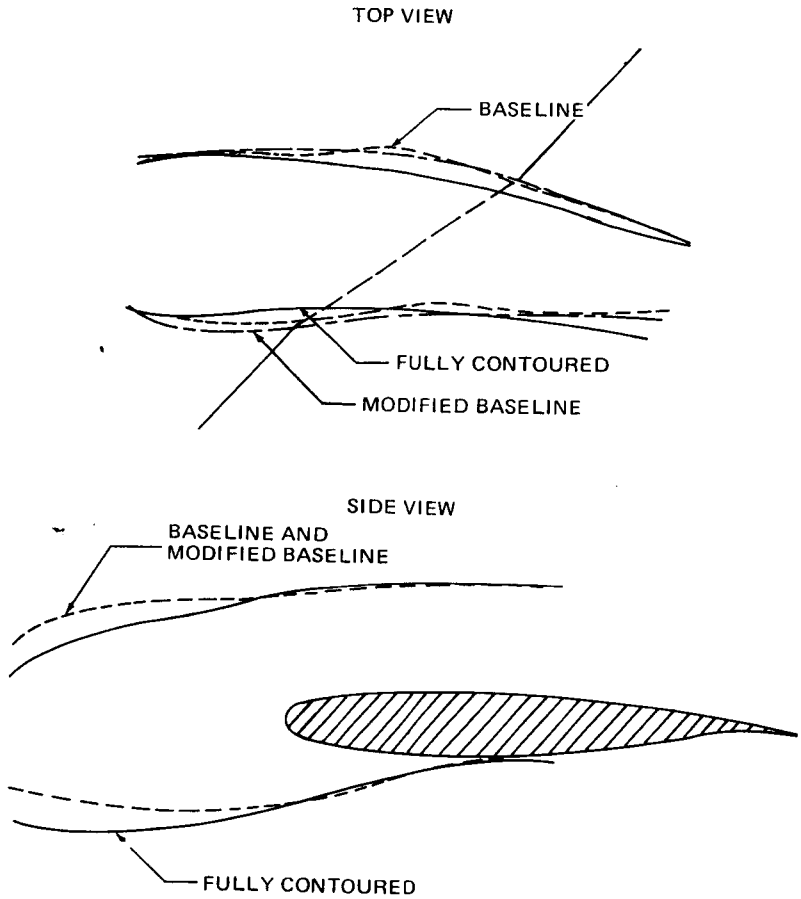

FIGURE 64. OVERWING CONTOURED NACELLE MODIFICATIONS, GEOMETRY COMPARISON

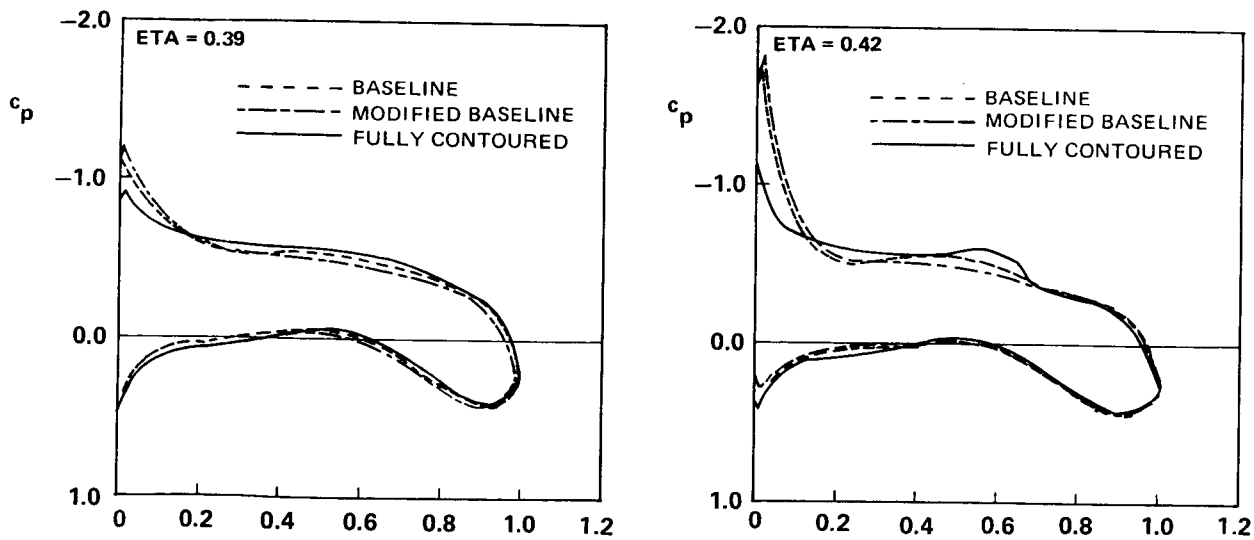

FIGURE 65. OVERWING CONTOURED NACELLE MODIFICATIONS, NEUMANN CHORDWISE PRESSURE COMPARISONS

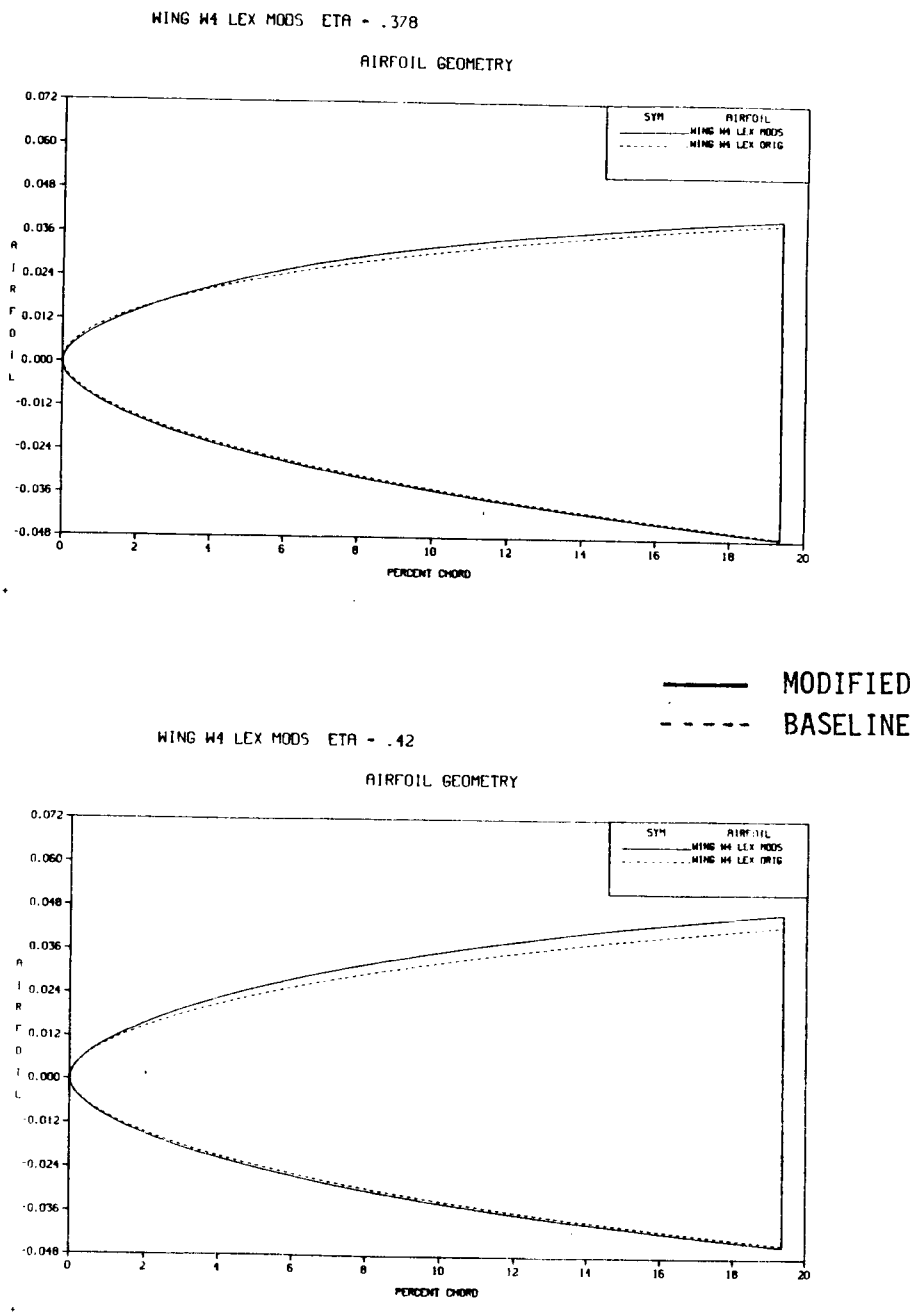

FIGURE 66. OVERWING CONTOURED NACELLE LEX MODIFICATIONS, GEOMETRY COMPARISONS

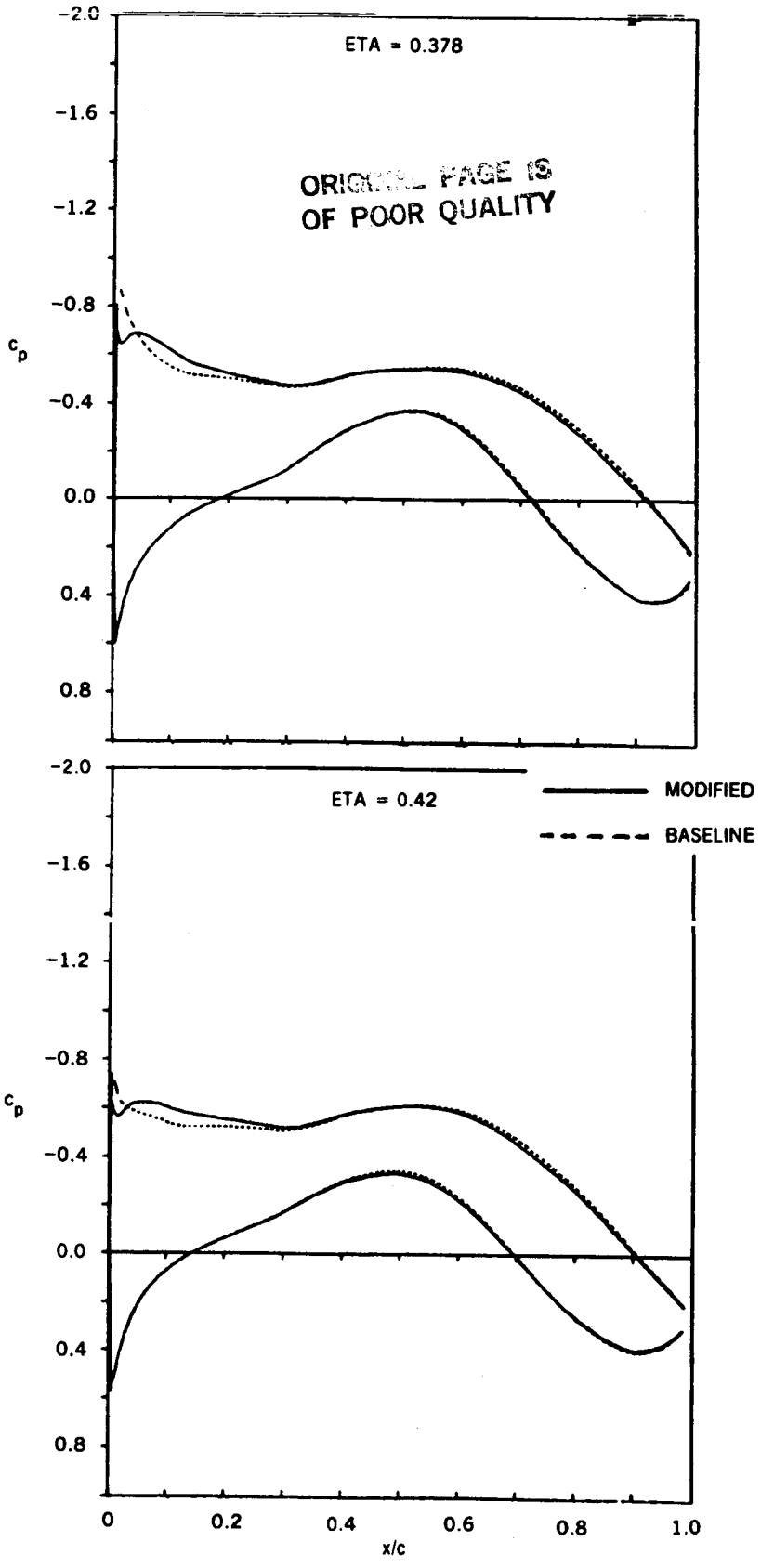

FIGURE 67. OVERWING CONTOURED NACELLE LEX MODIFICATIONS, JAMESON CHORDWISE PRESSURE COMPARISONS

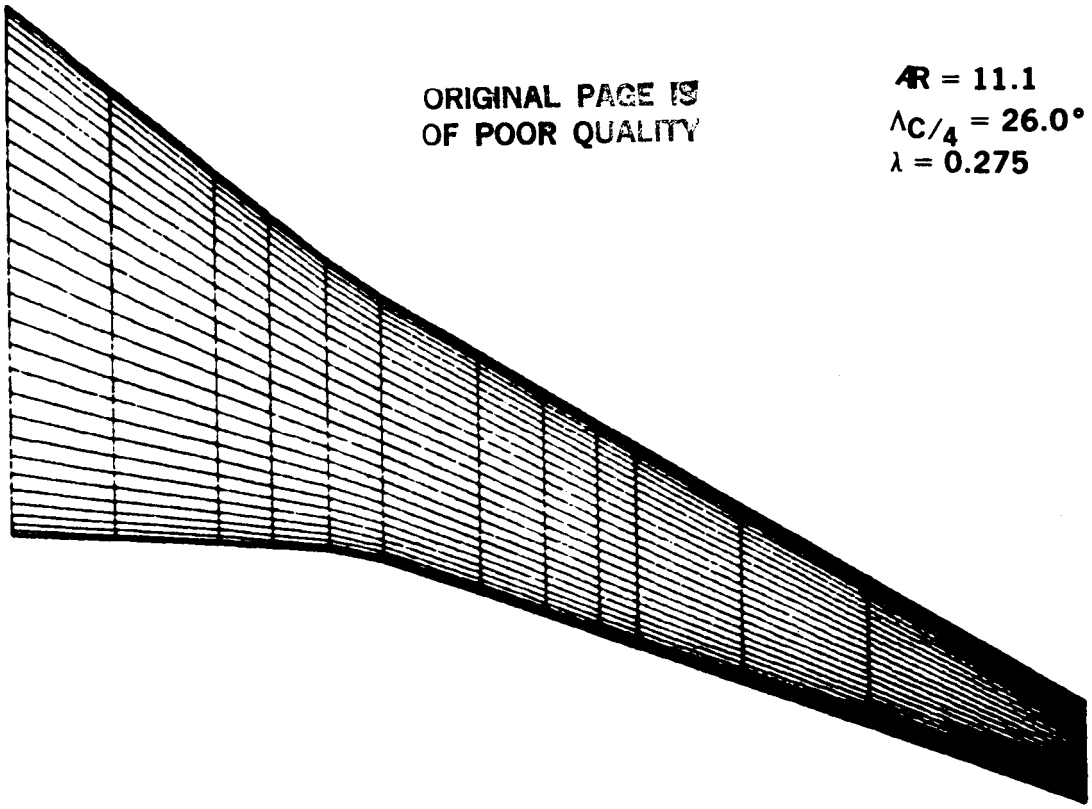

FIGURE 68. BASELINE WING W1 GEOMETRY

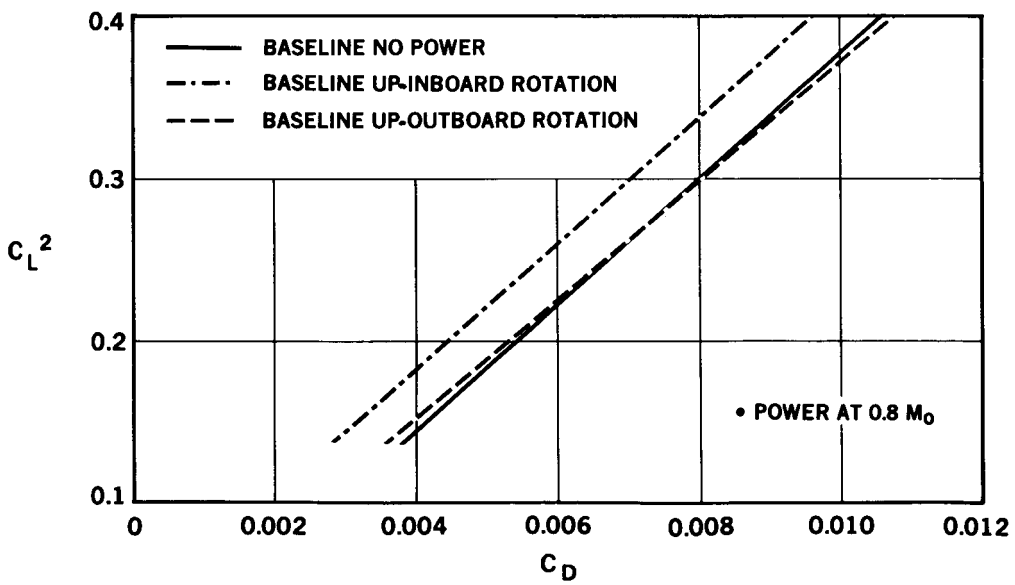

FIGURE 69. LIFTING LINE INDUCED DRAG POLARS, BASELINE WING

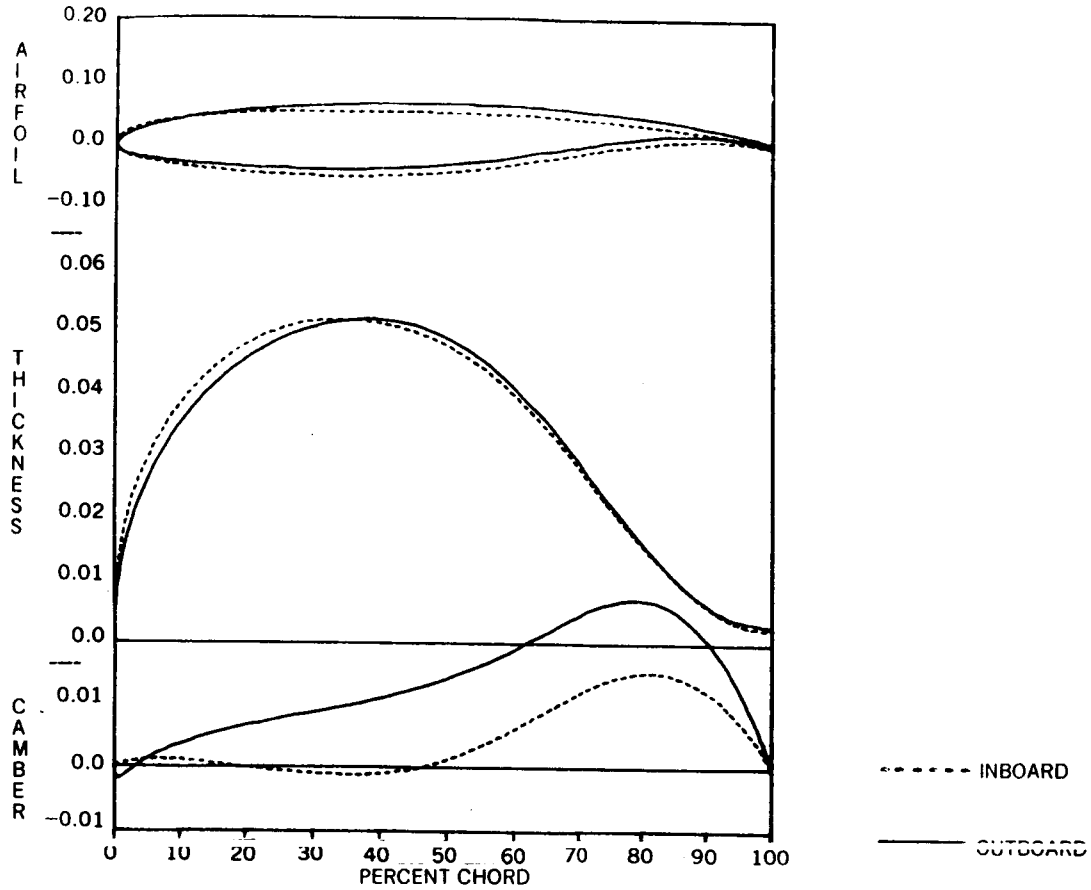

FIGURE 70. COMPARISON OF AIRFOIL GEOMETRIES FOR UP-OUTBOARD PROP ROTATION WING AT 70% PROP BLADE RADIUS

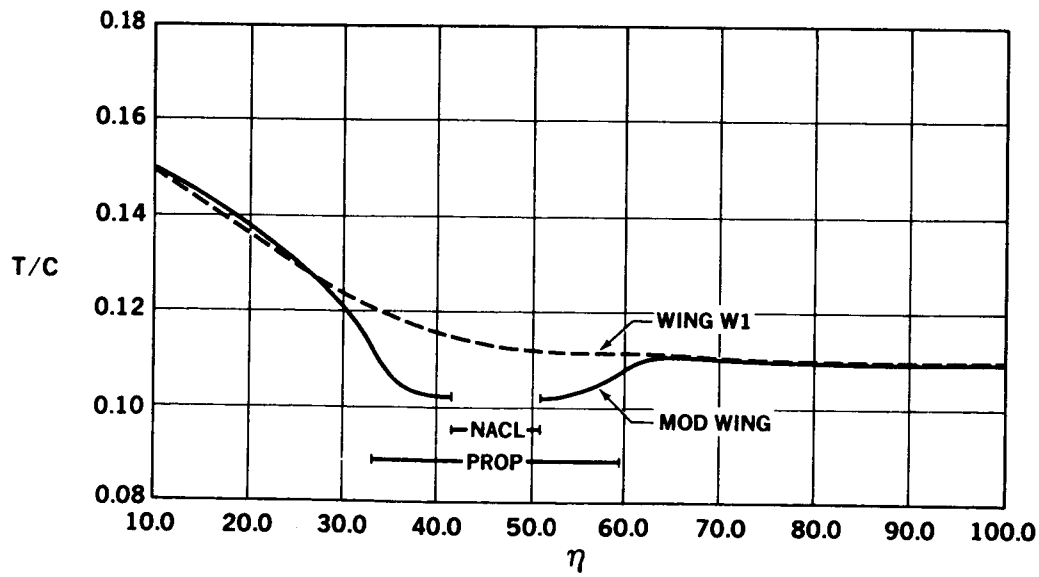

FIGURE 71. COMPARISON OF WING W1 AND MODIFIED WING THICKNESS DISTRIBUTIONS

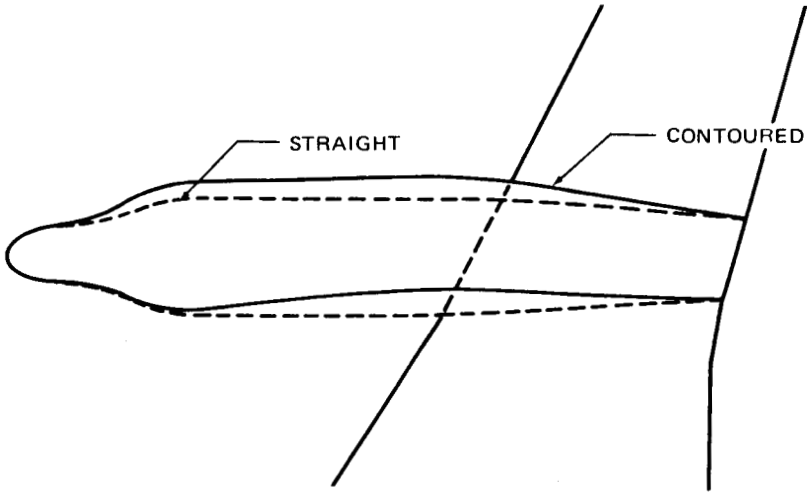

FIGURE 72. COMPARISON OF STRAIGHT AND CONTOURED OVERWING NACELLE SHAPES – TOP VIEW

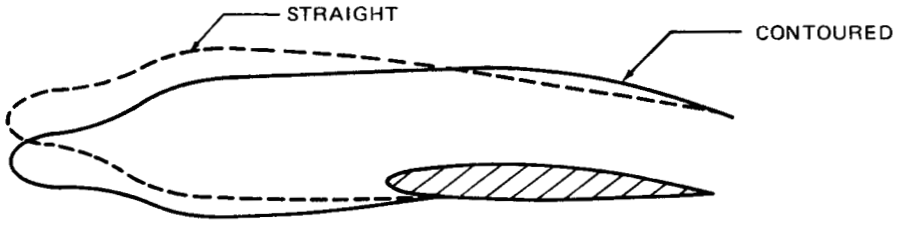

FIGURE 73. COMPARISON OF STRAIGHT AND CONTOURED OVERWING NACELLE SHAPES – SIDE VIEW

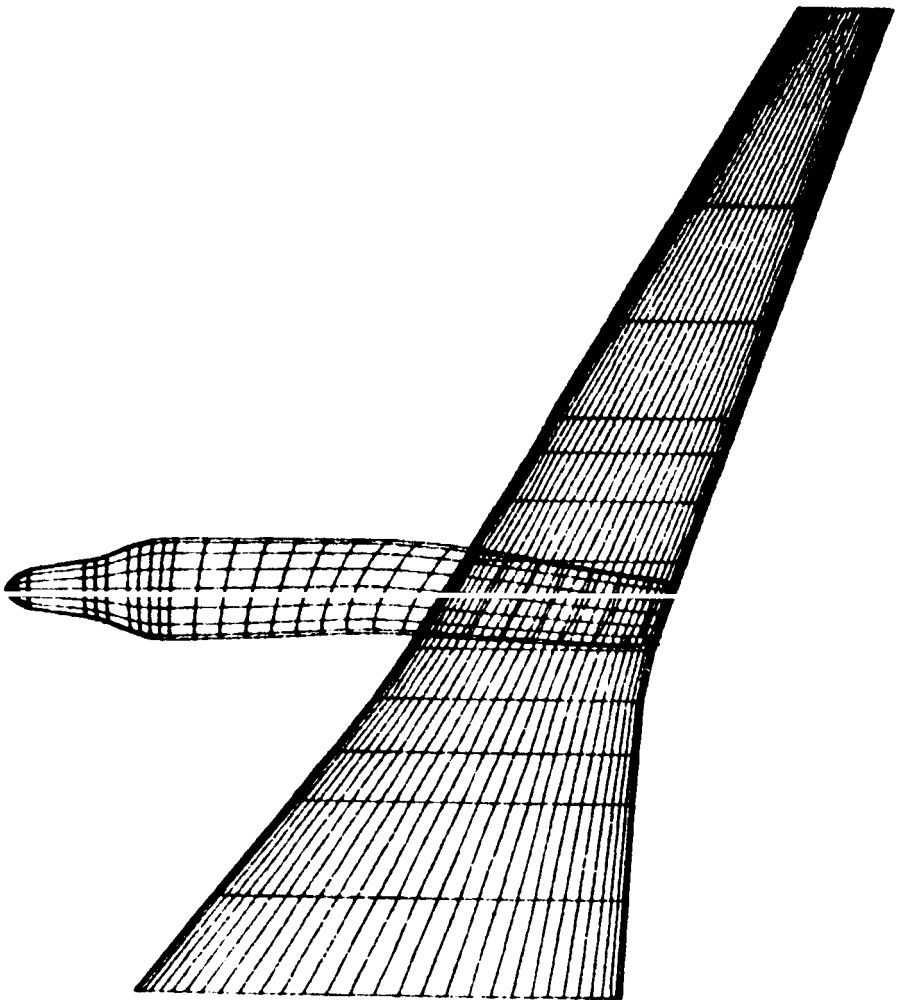

FIGURE 74. MODIFIED WING AND CONTOURED NACELLE GEOMETRY, TOP VIEW

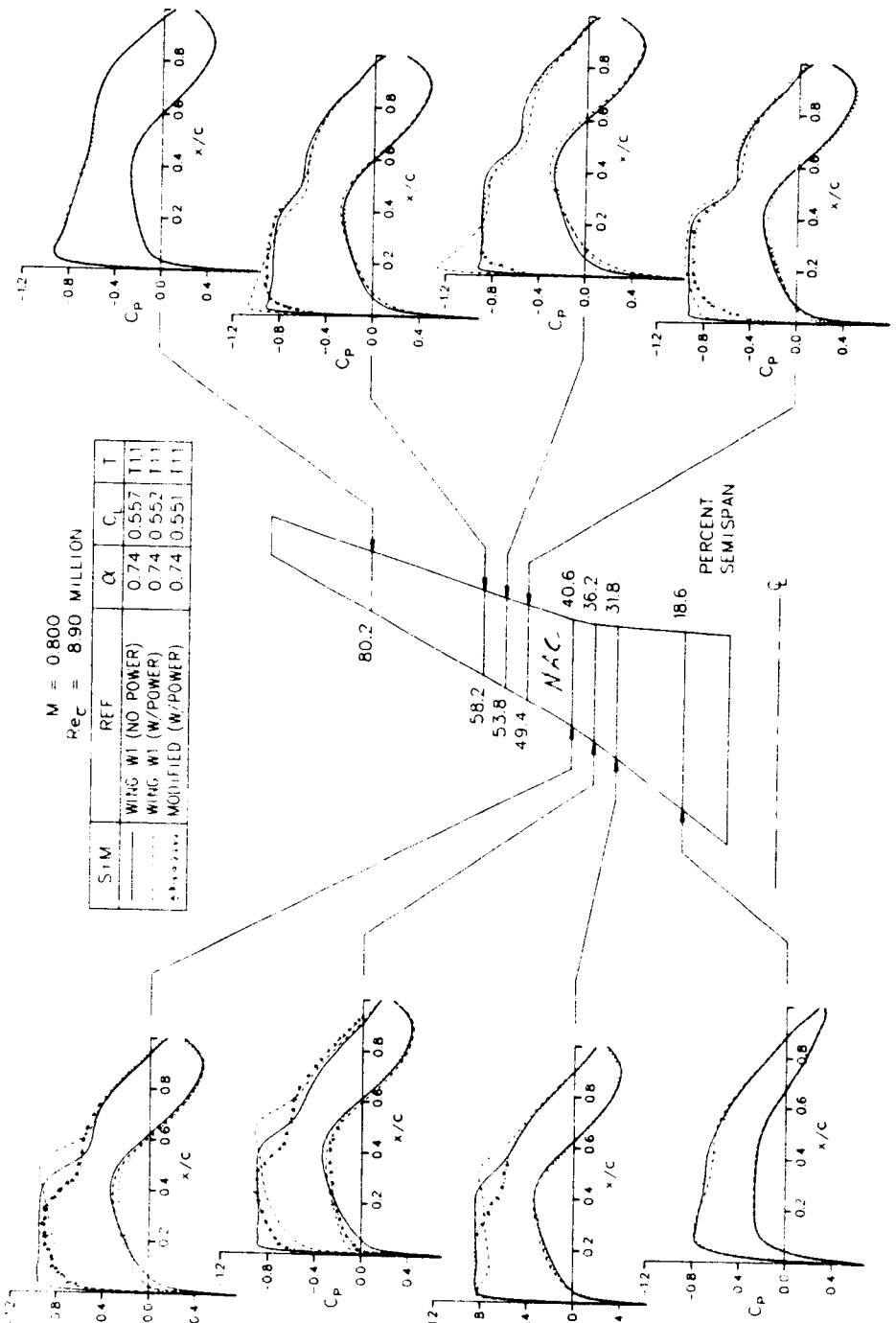

FIGURE 75. CHORDWISE PRESSURE DISTRIBUTIONS FOR MODIFIED AND BASELINE WINGS

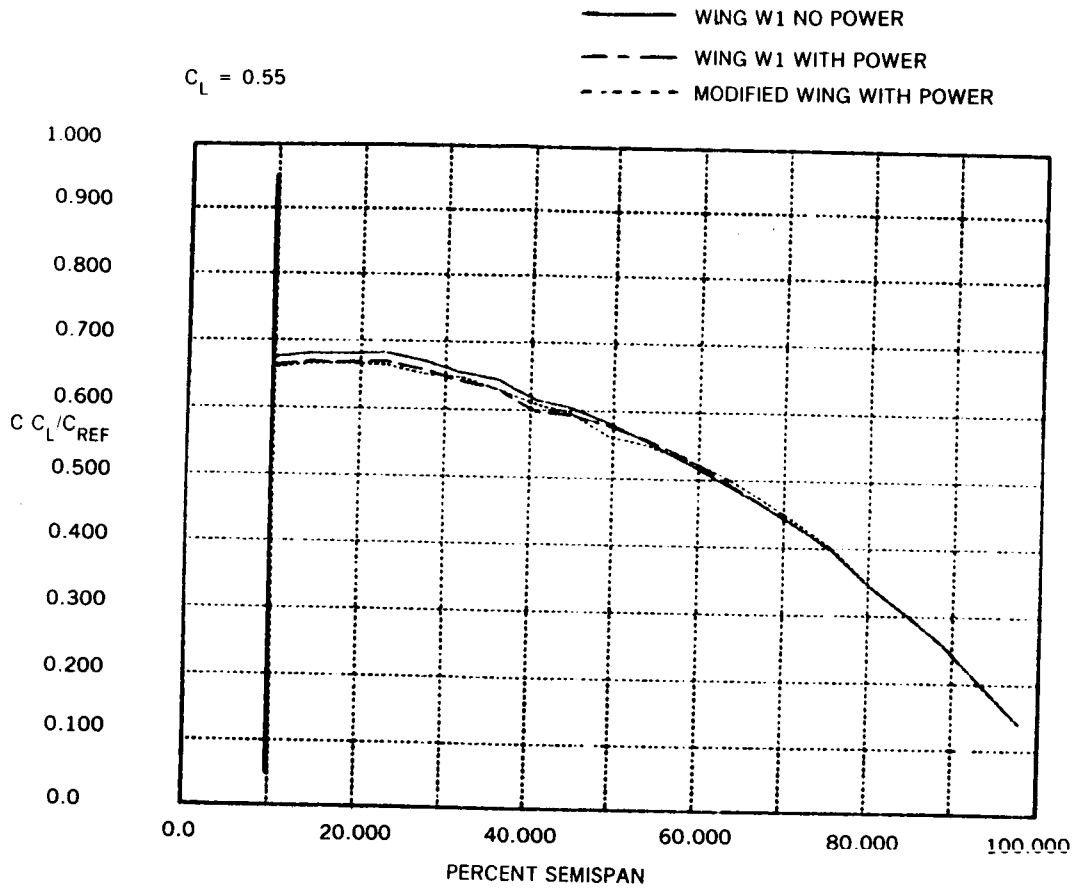

FIGURE 76. JAMESON SPAN LOADINGS FOR MODIFIED AND BASELINE WINGS

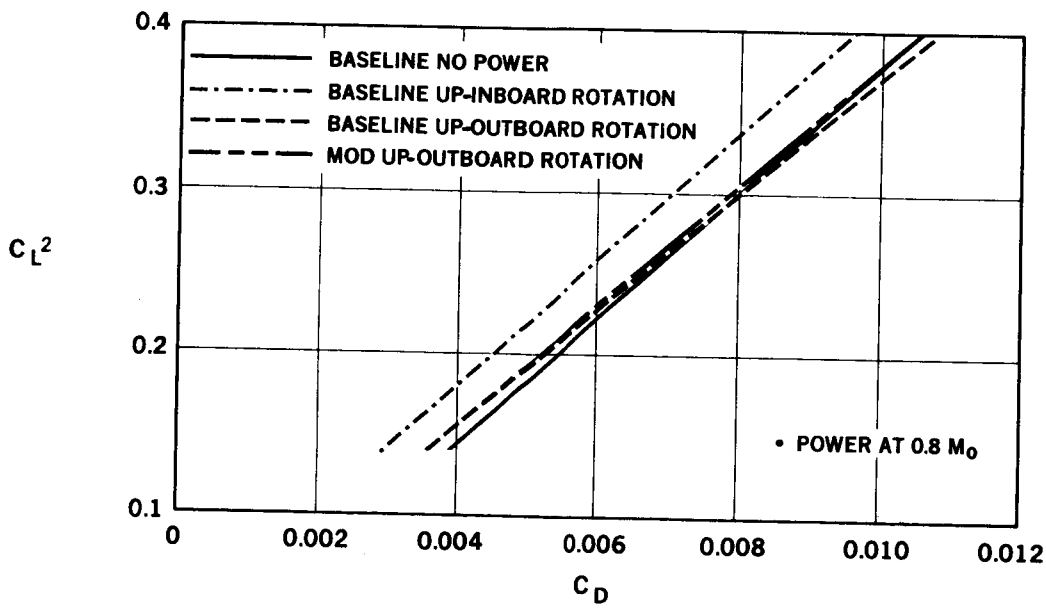

FIGURE 77. LIFTING LINE INDUCED DRAG POLARS, BASELINE AND MODIFIED WING

1. Report No.	2. Government Accession No.	3. Recipient's Catalog No.
NASA CR 166582		

4. Title and Subtitle	5. Report Date
Propfan Experimental Data Analysis	August 1984
	6. Performing Organization Code

7. Author(s)	8. Performing Organization Report No.
David F. Vernon, Greg S. Page, H. Robert Welge	ACEE-28-FR-
	10. Work Unit No.

9. Performing Organization Name and Address	11. Contract or Grant No.
Douglas Aircraft Company 3855 Lakewood Blvd. Long Beach, CA 90846	NAS2-11672
	13. Type of Report and Period Covered
12 Sponsoring Agency Name and Address National Aeronautics and Space Administration Ames Research Center Moffett Field, CA 94035	Contractor Report
	14. Sponsoring Agency Code

15. Supplementary Notes
Point of Contact: Alan D. Levin 227-6
Moffett Field, CA 94035
Commerical No. (415) 965-5858, FTS 448-5858

16. Abstract

A data reduction method, which is consistent with the performance predition methods used for analysis of new aircraft designs, is defined and compared to the method currently employed by NASA using data obtained from an Ames Research Center 11-foot transonic wind tunnel test (316-3-11).

Pressure and flow visualization data from The Ames test for both the powered straight underwing nacelle, and an unpowered contoured overwing nacelle installation is used to determine the flow phenomena present for a wing mounted turboprop installation. The test data is compared to analytic methods, showing the analytic methods to be suitable for design and analysis of new configurations. The data analysis indicated that designs with zero interference drag levels are achieveable with proper wing and nacelle tailoring. A new overwing contoured nacelle design and a modification to the wing leading edge extension for the current wind tunnel model design are evaluated. Hardware constraints of the current model parts prevent obtaining any significant performance improvement due to a modified nacelle contouring.

A new, aspect ratio 11 wing design for an up outboard rotation turboprop installation is defined, and an advanced contoured nacelle is provided. The design shows a slight drag reduction, compared to the unpowered clean wing, and maintains good pressure characteristics for the power-on case.

17. Key Words (Suggested by Author(s))	
Transonic Design Turboprop Wing Design Propulsion Integration	Release Date: June 1987 Star Category 05

19. Security Classif. (of this report)	20. Security Classif. (of this page)	21. No. of Pages	22. Price
Unclassified	Unclassified	PAGE 126 INTENTIONALLY BLANK	

*For sale by the National Technical Information Service, Springfield, Virginia 22151

DOUGLAS AIRCRAFT COMPANY

3855 Lakewood Boulevard, Long Beach, California 90846 (213) 593-5511

MCDONNELL DOUGLAS CORPORATION

PRINTED IN U.S.A. 9/84 TECH-1951